



DIGITAL ACCESS TO SCHOLARSHIP AT HARVARD

Nonlinear optical and optoelectronic studies of topological insulator surfaces

The Harvard community has made this article openly available.
[Please share](#) how this access benefits you. Your story matters.

Citation	No citation.
Accessed	February 17, 2015 12:43:14 AM EST
Citable Link	http://nrs.harvard.edu/urn-3:HUL.InstRepos:13064980
Terms of Use	This article was downloaded from Harvard University's DASH repository, and is made available under the terms and conditions applicable to Other Posted Material, as set forth at http://nrs.harvard.edu/urn-3:HUL.InstRepos:dash.current.terms-of-use#LAA

(Article begins on next page)

HARVARD UNIVERSITY
Graduate School of Arts and Sciences



DISSERTATION ACCEPTANCE CERTIFICATE

The undersigned, appointed by the
Department of Physics
have examined a dissertation entitled

Nonlinear optical and optoelectronic studies of topological insulator surfaces

presented by James W. McIver

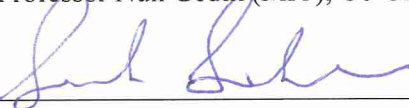
candidate for the degree of Doctor of Philosophy and hereby
certify that it is worthy of acceptance.

Signature  _____


Typed name: Professor Jennifer Hoffman, Chair

Signature  _____

Typed name: Professor Nuh Gedik (MIT), Co-Chair

Signature  _____

Typed name: Professor Subir Sachdev

Signature  _____

Typed name: Dr. Ronald Walsworth

Date: September 8, 2014

*Nonlinear optical and optoelectronic studies of
topological insulator surfaces*

A DISSERTATION PRESENTED
BY
JAMES W. McIVER
TO
THE DEPARTMENT OF PHYSICS

IN PARTIAL FULFILLMENT OF THE REQUIREMENTS
FOR THE DEGREE OF
DOCTOR OF PHILOSOPHY
IN THE SUBJECT OF
PHYSICS

HARVARD UNIVERSITY
CAMBRIDGE, MASSACHUSETTS
SEPTEMBER 2014

© 2014 - *JAMES W. McIVER*
ALL RIGHTS RESERVED.

Nonlinear optical and optoelectronic studies of topological insulator surfaces

ABSTRACT

Since their experimental discovery in 2008, topological insulators have been catapulted to the forefront of condensed matter physics research owing to their potential to realize both exciting new technologies as well as novel electronic phases that are inaccessible in any other material class. Their exotic properties arise from a rare quantum organization of its electrons called “topological order,” which evades the conventional broken symmetry based-classification scheme used to categorize nearly every other state of ordered matter. Instead, topologically ordered phases are classified by topological invariants, which characterize the phase of an electron’s wavefunction as it moves through momentum space. When a topologically ordered phase is interfaced with an ordinary phase, such as the vacuum, a novel metallic state appears at their shared boundary. In topological insulators, this results in the formation of a two-dimensional metallic state that spans all of its surfaces. The surface state electronic spectrum is characterized by a single linearly dispersing and helically spin-polarized Dirac cone that is robust

against disorder. The helical nature of the surface Dirac cone is highly novel because the Dirac electrons carry a net magnetic moment and are capable of transporting 100% spin-polarized electrical currents, which are the long-sought electronic properties needed for many spin-based electronic applications. However, owing to the small bulk band gap and intrinsic electronic doping inherent to these materials, isolating the surface electronic response from the bulk has proven to be a major experimental obstacle.

In this thesis, we demonstrate the means by which light can be used to isolate and study the surface electronic response of topological insulators using optoelectronic and nonlinear optical techniques. In chapter 1, we overview the physics of topological order and topological insulators. In chapter 2, we show how polarized light can be used to generate and control surface electrical currents that originate from the helical Dirac cone. In chapter 3, we demonstrate that the nonlinear second harmonic generation of light from a topological insulator is a sensitive surface probe and can be used to detect the breaking of space-time symmetries and monitor changes in the surface carrier density.

Contents

1	INTRODUCTION	2
1.1	The quantum Hall insulator and topological order . . .	3
1.2	The quantum spin Hall insulator and Z_2 topological order	10
1.3	The three-dimensional topological insulator	15
2	OPTOELECTRONIC MANIPULATION OF ELECTRONS ON THE SURFACE OF A TOPOLOGICAL INSULATOR	24
2.1	The circular photogalvanic effect	26
2.2	Observation of the circular photogalvanic effect in the topological insulator Bi_2Se_3	31
2.3	Phenomenological description of photocurrents in $\text{Bi}_2\text{Se}_3(111)$	54
3	SECOND HARMONIC GENERATION FROM THE SURFACE OF A TOPO- LOGICAL INSULATOR	76
3.1	Theoretical background	78
3.2	Experimental results	95

3.3 Summary and outlook 116

REFERENCES **131**

Listing of figures

1.1.1 Topology of closed surfaces	6
1.1.2 The quantum Hall insulator	8
1.2.1 The quantum spin Hall insulator	11
1.2.2 Z_2 topological order	13
1.3.1 The topological insulator	17
1.3.2 Bi_2Se_3 crystal and electronic structure	20
2.0.1 Topological insulator spin currents	25
2.1.1 Spin-dependent optical transitions	28
2.1.2 The circular photogalvanic effect	29
2.2.1 AFM image of Bi_2Se_3 device	32
2.2.2 Photocurrent generation and detection	34
2.2.3 Thermoelectric currents and linear response	36
2.2.4 Photocurrent polarization dependence (xz-plane) . . .	38
2.2.5 Photocurrent polarization dependence (yz-plane) . . .	39
2.2.6 Photocurrent polarization dependence (normal inc.) .	40
2.2.7 Photocurrent temperature dependence and absorptivity	41
2.2.8 Microscopic mechanisms of photocurrent generation .	44

2.2.9	Absence of Rashba-split states	46
2.2.10	Ultrafast bulk spin relaxation	49
2.2.11	Laser intensity dependence of photocurrents	51
2.2.12	Continuous wave vs pulsed laser excitation	52
2.2.13	Consistent results across multiple devices	53
2.3.1	C_{3v} symmetry of the $\text{Bi}_2\text{Se}_3(111)$ cleaved surface	58
2.3.2	Experimental geometry for photocurrent measurements	60
3.1.1	C_{3v} symmetry of the $\text{Bi}_2\text{Se}_3(111)$ cleaved surface	80
3.1.2	SHG active regions	84
3.1.3	SHG laser beam geometry and polarizations	91
3.2.1	Bi_2Se_3 refractive index and penetration depth	96
3.2.2	SHG experimental apparatus	98
3.2.3	SHG sample geometry and linear optical response	100
3.2.4	Rotational anisotropy of SHG from $\text{Bi}_2\text{Se}_3(111)$	102
3.2.5	SHG φ dependence at different times after cleavage in air	105
3.2.6	Time evolution of SHG after cleavage in air	106
3.2.7	Time evolution of fit coefficients after cleavage in air	107
3.2.8	SHG time-dependence after cleavage in O_2	110
3.2.9	Circular dichroism SHG from Bi_2Se_3	114

Acknowledgments

This thesis would not have been possible without the help of many people to whom I am so grateful. First and foremost, I want to thank my wonderful advisor Nuh Gedik for his mentorship and support. He has been a constant source of enthusiasm, ideas and advice throughout my graduate career, and I couldn't have picked a better advisor. I am also indebted to all of my lab mates for their help and friendship over the years: Darius, David, Yihua, Dan, Alex, Fahad, Edbert, Changmin, Steve, Claudia, Mahmoud, Jaime, Ryan, Zhanybek, Timm, Inna, Joshua, Ozge, Byron and all the undergraduates that have passed through. Thank you so much for making such a great lab community. I'd especially like to thank former postdocs Darius Torchinsky and David Hsieh. Darius ultimately convinced me to join the Gedik group, and taught me an enormous amount about ultrafast optics and how to survive graduate school. David taught me everything I know about topological insulators and helped me write my first papers in the group, and continues to be a great source of advice. I'd also like to extend thanks

to Hadar Steinberg, Pablo Jarillo-Herrero, Valla Fatemi, Dillon Gardner, Young Lee and Liang Fu for being such enthusiastic collaborators and mentors at MIT. I also want to thank my other committee members Jenny Hoffman, Ron Walsworth and Subir Sachdev for keeping me on track and providing useful career advice. And of course none of this would be possible without the help of Monica Wolf and Lisa Cacciabauda, who so kindly helped me with mounds of Harvard and MIT paperwork over the years. Many thanks to them, and to everyone else I've interacted with at Harvard and MIT.

Graduate school can be a grueling process and getting through it would not have been possible without all the friends I made in Boston along the way. I'd especially like to thank the members of my bluegrass band Cold Chocolate, who provided a much needed extracurricular outlet. Also my long time friend and room mate Simon, whose editing skills transformed multiple fellowship applications. Finally, I'd like to thank my partner Rachel, my parents, siblings and other family members and friends for their abundant love and encouragement.

This page is intentionally left blank

1

Introduction

THE PHYSICS OF TOPOLOGICAL INSULATORS is best understood through a historical narrative, since the underlying principles of topological order naturally unfold in this way. Section 1.1 introduces the quantum Hall insulator—the first known topologically ordered phase—and the basics of topological order. The second section covers the quantum spin Hall insulator, which can be thought of as two spin-polarized copies of the quantum Hall insulator in the absence of a magnetic field. Section 1.3 introduces the topological insulator, which is the first known three-dimensional topological phase of matter and the subject of this thesis.

1.1 THE QUANTUM HALL INSULATOR AND TOPOLOGICAL ORDER

Ordered phases of matter are typically classified by the symmetries that they break. A crystalline solid, for example, breaks the continuous rotational and translational symmetry of space in favor of reduced discretized versions of these symmetries. As physicists, the way that we identify different phases is by using probes that are sensitive to the symmetries being broken. In this example one would perform a scattering experiment and look for discretized scattering vectors as evidence that the continuous spatial symmetries had been broken.

This broken symmetry-based classification scheme can also be used to define quantum electronic phases. In materials that possess charge density wave order, the electron density forms a sinusoidal distribution in space, thereby breaking the continuous translational symmetry that a uniform electron density in an ordinary metal would have. Ferromagnetic phases break time-reversal symmetry: if time is reversed, the electrons spin in the opposite direction thereby reversing the direction of their magnetic moments. Ferromagnets also break the rotational symmetry of spin space. Even the most exotic phases such as superconductivity can be classified in this way, though more subtle. Here gauge symmetry is broken when Cooper pairs form to make a superconducting condensate. This symmetry-based classification scheme, originally devised by Lev Landau [1], was believed for many years to be the most fundamental means of defining distinct ordered phase of condensed matter.

However, this seemingly infallible paradigm of identifying electronic phases by their broken symmetries was challenged in 1980 with the unexpected discovery of the quantum Hall effect by K. von Klitzing and collaborators [2]. The effect occurred in an electrical insulator, which, as will be discussed in the following pages, is both very important and not by accident. The sample under study was a two-dimensional electron gas, which can be formed in transistor-like semiconductor devices. Left alone a Fermi gas of electrons will be metallic, but when a strong magnetic field is applied the electrons condense into cyclotron orbits and form Landau levels. If the system is tuned so that the Fermi level lies inside the energy gap between two Landau levels, which can be achieved by adjusting the magnetic field strength, one would expect the material to be electrically insulating and show zero conductivity, according to the semi-classical Boltzmann theory for electron transport [3]. However, upon performing this experiment von Klitzing and collaborators, to their surprise, observed a nonzero and precisely quantized Hall conductivity in integer multiples of a fundamental constant of nature

$$\sigma_{xy} = n \frac{e^2}{h} \quad (1.1)$$

where σ_{xy} is the transverse or Hall conductivity, e is the electron charge, h is Planck's constant, and n is an integer precise to nearly one part in a billion, irrespective of sample geometry or impurity content. The

discovery, which won von Klitzing the 1985 Nobel Prize, raised many important questions. Why, in an insulating state, is the Hall conductivity nonzero and so precisely quantized? What electronic states are carrying the current? And finally, how do we classify this new quantum phase? By all measures no new symmetries were being broken when the index n in (1.1) changed; for the first time Landau's paradigm had failed. The answer to these questions lied in the fact that this was a new kind of electronic ordering that had never been observed before, called topological order.

Topology is the branch of mathematics concerned with the properties of geometric shapes that do not change under smooth deformations. The mathematical quantities that do not change under these deformations are called topological invariants. As an example consider one of the fundamental theorems of topology, the Gauss-Bonnet theorem [4], which states that the integral of the local curvature over a closed surface S is quantized and is a topological invariant

$$\frac{1}{2\pi} \int_S K dA = 2(1 - g) \quad (1.2)$$

where K is the local curvature of the surface and the genus g is the number of holes in the shape created by the closed surface, which characterizes the topology of the surface. The sphere in Figure 1.1.1 for example has $g = 0$ and no matter how the sphere is deformed, provided no holes are punctured thereby changing the genus, the integral on the left

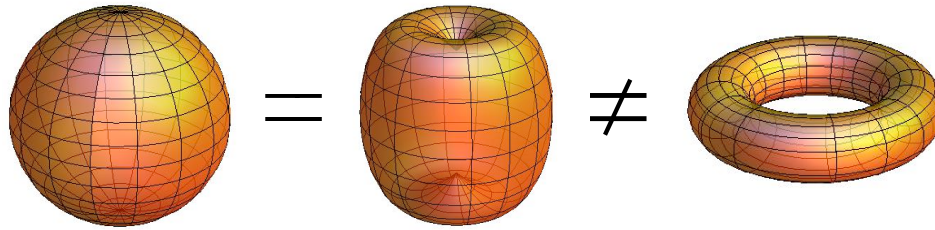


Figure 1.1.1: Topology of closed surfaces. Closed surfaces are topologically equivalent if the shape they create shares the same number of holes g . This is because the integral of their total curvature is a topological invariant that depends only on g and is insensitive to any other geometric properties, according to the Gauss-Bonnet theorem (1.2).

side of (1.2) will always yield the same result and is therefore a topological invariant. This same line of reasoning applies to a torus, where $g = 1$, or any other closed surface with any number of holes. Any shapes with the same number of holes are considered to be topologically equivalent because they share the same topological invariant and can be smoothly deformed into each other. This theorem can also be generalized to higher dimensional closed surfaces [5].

In topologically ordered phases, the topology of relevance is ultimately that of the Hilbert space—the mathematical space spanned by the electronic wavefunctions—which can have intrinsic curvature and be described by topological invariants. This manifests in the geometric properties of the parameter space of the Hamiltonian describing a given system, which is a more convenient theoretical language to use when discussing topological physics. In a pioneering paper [6], Thouless *et*

al. made the connection between topology and the quantized Hall conductivity, showing that the integer n in (1.1) is a topological invariant, called a Chern number, that describes the topology of the Hilbert space and is given by a modified formulation of the Gauss-Bonnet theorem

$$n = \frac{1}{2\pi} \int_{BZ} [\nabla_{\mathbf{k}} \times \mathbf{A}(k_x, k_y)]_z d^2k \quad (1.3)$$

with

$$\mathbf{A} = -i \langle u_k | \nabla_{\mathbf{k}} | u_k \rangle \quad (1.4)$$

where the integral is over all the occupied states in the magnetic Brillouin zone [6, 7], and u_k is the periodic part of the Bloch wavefunction [3]. The Berry curvature $\Omega = \nabla_{\mathbf{k}} \times \mathbf{A}(k_x, k_y)$ is related to the Berry phase [8], which is quantum mechanical phase, purely geometric in origin, that electron wavefunctions can accumulate when cycling a closed path in a parameter space that has intrinsic curvature. Since the Berry curvature is odd under time-reversal, σ_{xy} must vanish in the absence of an external magnetic field for inversion symmetric systems. However, because σ_{xy} is proportional to a topological (Chern) invariant, it cannot smoothly evolve from zero as the magnetic field is varied. Instead, it must jump from one discrete value to another once the magnetic field is sufficiently strong enough to alter the topology of the Hilbert space.

Equation (1.3) shows that the quantum Hall current is proportional to the number of *fully* occupied Landau levels—as the magnetic field

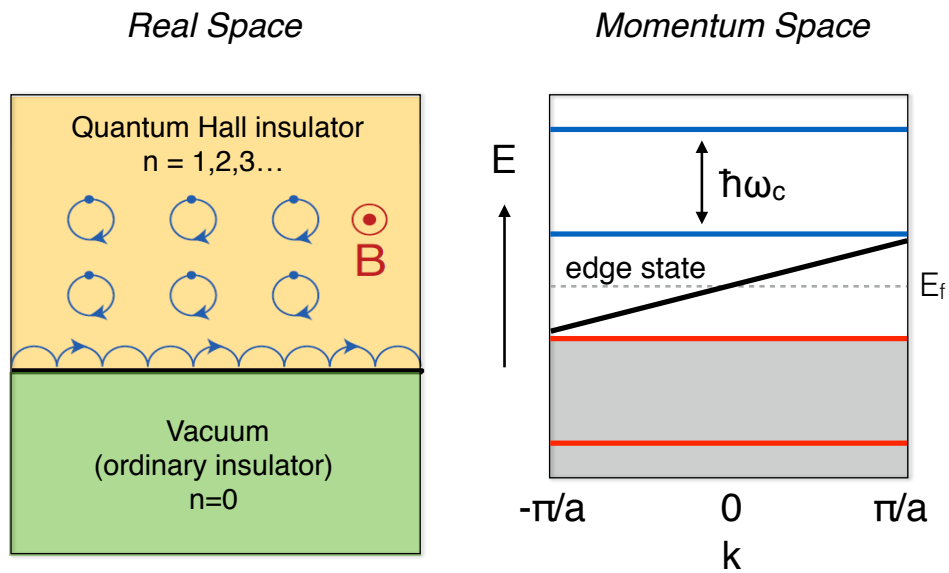


Figure 1.1.2: The quantum Hall insulator. Metallic chiral edge states appear at the boundary between a quantum Hall insulator and an ordinary insulator so that the distinct Hilbert space topologies encoded in the insulating phases can change.

strength is tuned and more Landau levels sink beneath the Fermi energy, the index n increases and more conduction channels open. This is surprising because according to the semi-classical Boltzmann theory of electron transport [3], fully occupied bands should be electrically insulating. Building on earlier work by Laughlin [9], Halperin showed that for a system with Hall conductivity $\sigma_{xy} = n e^2/h$, there must be n branches of metallic one-dimensional chiral edge states connecting adjacent Landau levels at the sample boundary, where the chirality is set by the magnetic field direction [Figure 1.1.2] [10]. These metallic edge states arise because the nontrivial topology of the insulating states responsible for the quantized Hall current cannot be smoothly deformed into the ordinary insulating states at the sample boundary (which includes the vacuum). This is because the nontrivial topology is a discrete characteristic of gapped energy states, and as long as the gap remains open, the topology cannot change. Hence, in order for the topology to change at an interface, the insulating gap must close, thereby forming a metallic state. The extreme precision in which the conductivity is quantized, which is unaffected by impurity content, is because σ_{xy} is proportional to a topological invariant that has an integer nature. This topological property manifests in the fact that the metallic edge states are unidirectional: the absence of conduction channels moving in the opposite direction makes backscattering impossible, thus the Hall current is dissipationless, which has made such materials attractive for energy efficient electronics technologies. Since there are no spontaneously broken symmetries to probe in the quantum Hall insulator, the presence

of these metallic states at the sample boundary act as an identifying signature of topological order.

1.2 THE QUANTUM SPIN HALL INSULATOR AND Z_2 TOPOLOGICAL ORDER

The quantum Hall insulator generated great interest throughout the condensed matter physics community, which quickly became eager to discover more topologically ordered electronic phases. Of particular interest was eliminating the need for a strong magnetic field, which can be difficult to implement in experiments and technological applications. Attention moved to spin-orbit coupling as a possible alternative, where the static nuclear electric field is relativistically transformed into an intrinsic spin-dependent magnetic field in the reference frame of a moving electron [11]. While spin-orbit coupling does not have the necessary symmetry to induce the quantum Hall insulator (it does not break time-reversal symmetry like a magnetic field), simplified models introduced in the early 2000s showed that it can lead to a new phase called the quantum spin Hall insulator [12–15]. This phase can naively be thought of as two copies of the quantum Hall system with oppositely spin-polarized edge states that propagate in opposite directions [Figure 1.2.1], so as to preserve time-reversal symmetry. The spin-polarized edge states carry a conductivity

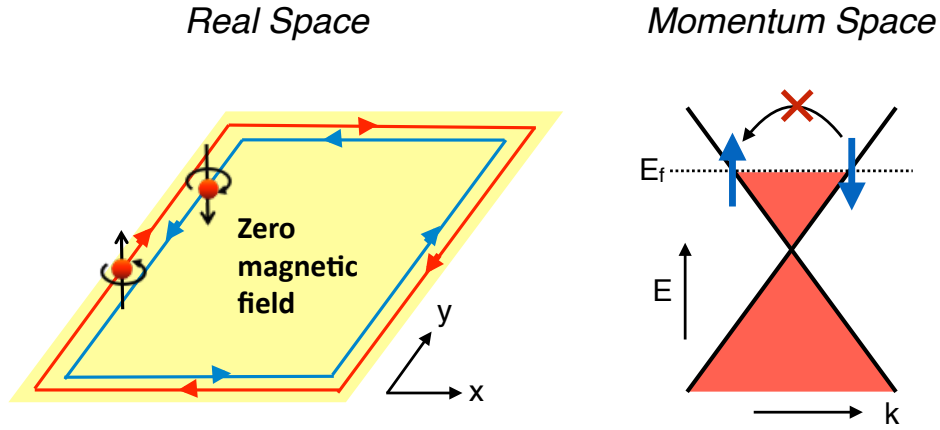


Figure 1.2.1: The quantum spin Hall insulator. Strong spin-orbit coupling replaces the magnetic field in the quantum Hall effect to give two oppositely spin-polarized edge states that propagate in opposite directions. These states form a spin-polarized Dirac cone in momentum space that sits between the valence and conduction bands. Backscattering is forbidden due to the absence of similar spin states propagating in the opposite direction.

$$\sigma_{xy}^{(\uparrow)} = n_{\uparrow} \frac{e^2}{2h}; \quad \sigma_{xy}^{(\downarrow)} = n_{\downarrow} \frac{e^2}{2h} \quad (1.5)$$

where $n_{\uparrow} = -n_{\downarrow}$. In momentum space, these spin-polarized edge states linearly disperse in opposite directions to form a Dirac cone between the valence and conduction bands [Figure 1.2.1]. The total charge conductivity is given by

$$\sigma_{xy} = (n_{\uparrow} + n_{\downarrow}) \frac{e^2}{2h} = 0 \quad (1.6)$$

This must be the case because the Hall conductivity in general can only

be nonzero when time-reversal symmetry is broken, which is not the case when spin-orbit coupling is the driving mechanism. The total spin conductivity on the other hand is nonzero

$$\sigma_{xy}^S = (n_{\uparrow} - n_{\downarrow}) \frac{e}{4\pi} \quad (1.7)$$

Equations (1.6) and (1.7) show that when a longitudinal electric field is applied, there is a net quantized transfer of spin in the transverse direction without any transfer of charge. It was proposed that this phase is topologically ordered with a topological invariant given by the total spin Chern number $(n_{\uparrow} - n_{\downarrow})$ [14]. However, as was pointed out by Kane and Mele [15], $(n_{\uparrow} - n_{\downarrow})$ is invariant only when σ_z is conserved, which tends to break down in real systems due to disorder, interband mixing and interactions. In a more realistic model, Kane and Mele showed that the topological properties of the quantum spin Hall insulator do still survive, but are encoded instead by a stable Z_2 topological invariant that is particular to time-reversal symmetric systems [15]. It expresses whether the one-dimensional edge state Fermi surfaces enclose an even ($Z_2 = 0$) or odd ($Z_2 = 1$) number of time-reversal invariant momenta [Figure 1.2.2]. Its value, 0 or 1, determines whether the system is an ordinary or quantum spin Hall insulator respectively.

Physically, the way to achieve a non-trivial Z_2 topological invariant is through band inversion. Ordinary insulators are typically characterized by a valence band edge with a p -like orbital character and a conduction

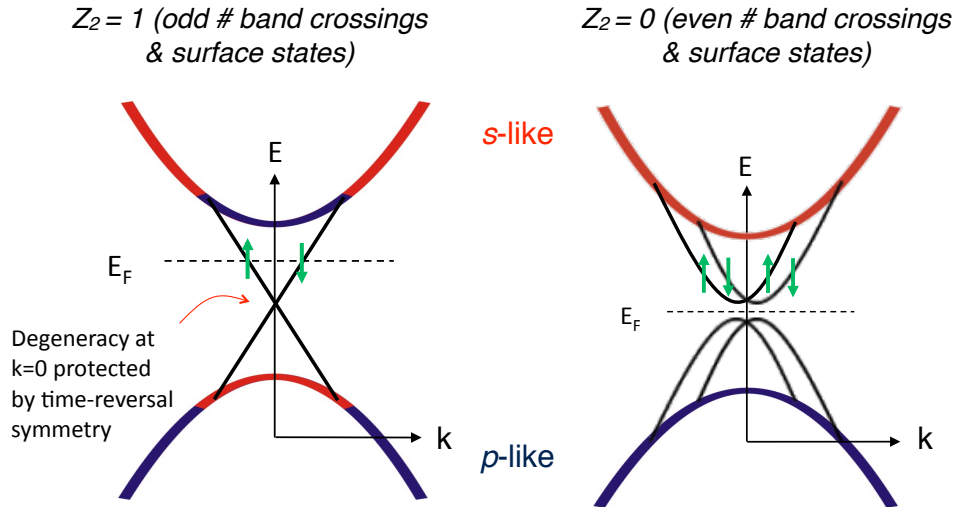


Figure 1.2.2: Z_2 topological order. (Left) $Z_2 = 1$ topological order describes an odd number of band inversions at time-reversal invariant momenta. The odd number of surface states that result are protected from opening a gap by time-reversal symmetry, thereby fulfilling the requirement that topological phases of matter have metallic boundary states. (Right) $Z_2 = 0$ order describes an ordinary insulator, which has an even number of surface states. These are free to hybridize and open an insulating energy gap without violating time-reversal symmetry. Thus, it cannot be a topological phase. Z_2 topological order applies to both the quantum spin Hall insulator and the topological insulator, where in the latter case ν_0 is the particular Z_2 topological invariant of relevance.

band edge with an s -like orbital character, in the sense that the wavefunctions have odd (anti-symmetric) and even (symmetric) parity respectively. A non-trivial Z_2 invariant arises when strong spin-orbit coupling causes the valence and conduction bands to invert an odd number of times at time-reversal invariant points in momentum space (like $\mathbf{k} = 0$), which induces a non-trivial Berry curvature of the occupied states. The odd number of edge states that result are protected from opening a gap by time-reversal symmetry, which requires that $E(\mathbf{k}, \uparrow) = E(-\mathbf{k}, \downarrow)$ [Figure 1.2.2 left]. An even number of crossings, on the other hand, induces an even number of edge states that are free to hybridize and form an energy gap [Figure 1.2.2 right]. This violates the necessity that a metal form at the interface between a topological and ordinary phase; thus, an even number of crossings cannot be topologically ordered.

Because the edge states form a time-reversed pair, backscattering is prohibited [Figure 1.2.1] in the absence of magnetic impurities (which can flip the spin) and transport is inherently dissipationless. Unlike the quantum Hall insulator, the topological properties of the quantum spin Hall insulator are manifested directly in its edge state energy dispersion (intrinsic to how the Z_2 topological invariant is defined). This provides an experimental advantage for studying topological invariants because the relevant temperature scale is no longer set by the phase coherence length of the many-body wavefunction, as with the quantum Hall insulator, but instead by the magnitude of the spin-orbit coupling induced energy gap.

The first real proposal for a quantum spin Hall insulator was made in 2006 by Bernevig, Hughes and Zhang for a particular HgTe/(Hg,Cd)Te quantum well heterostructure [16]. Heavy elements are needed because the phase requires strong spin-orbit coupling to induce band inversion. In 2007, Konig *et al.* experimentally verified the phase in the proposed HgTe/(Hg,Cd)Te quantum well structure through an intricate set of charge conductance measurements [17]. The spin polarization of the edge states has also been confirmed [18].

1.3 THE THREE-DIMENSIONAL TOPOLOGICAL INSULATOR

The discovery of the quantum spin Hall insulator, and the immense amount of theoretical development that paved the way, was a momentous achievement: a second topologically ordered phase had been discovered. However, the phase still left some to be desired in that a fabricated heterostructure is necessary, like with the quantum Hall insulator, which makes studying the buried one-dimensional edge states difficult with all but electron transport techniques. The complexity of the particular heterostructure required and the one-dimensionality of the topological edge states also limits potential future technological applications. These limitations, and general curiosity, motivated the need to discover a three-dimensional topologically ordered phase.

Building on the theoretical works that led to the discovery of the quan-

tum spin Hall insulator [13–15], new theoretical predictions arose between 2006 and 2007 showing that three-dimensional insulators can also be characterized by Z_2 topological invariants [19–22]. However, instead of being characterized by a single Z_2 invariant, insulators in three-dimensions are described by four Z_2 invariants $\nu_o; (\nu_1\nu_2\nu_3)$, of which only ν_o is robust against disorder. Ordinary three-dimensional insulators are described by $\nu_o = 0$, while $\nu_o = 1$ describes an intrinsically three-dimensional topologically ordered phase called the strong topological insulator [19, 22], or just topological insulator. Similar to the quantum spin Hall insulator, topological insulators arise from spin-orbit coupling induced band inversion that occurs an odd number of times at time-reversal invariant momenta in inversion symmetric crystals [Figure 1.2.2] [22].

Like all topologically ordered phases, when a topological insulator is interfaced with an ordinary insulator, like the vacuum, metallic states appear at the boundaries so that the distinct topologies of the insulating states can change. This results in the appearance of robust two-dimensional surface states that wrap around the three-dimensional bulk insulator [Figure 1.3.1]. Similar to the quantum spin Hall insulator, these surface states form time-reversed pairs so that electrons moving in opposite directions have opposite spin polarizations, with the spin orientation locked perpendicular to its direction of motion. In momentum space, these states take the form of a helically spin-polarized Dirac cone that sits between the bulk valence and conduction bands [Fig-

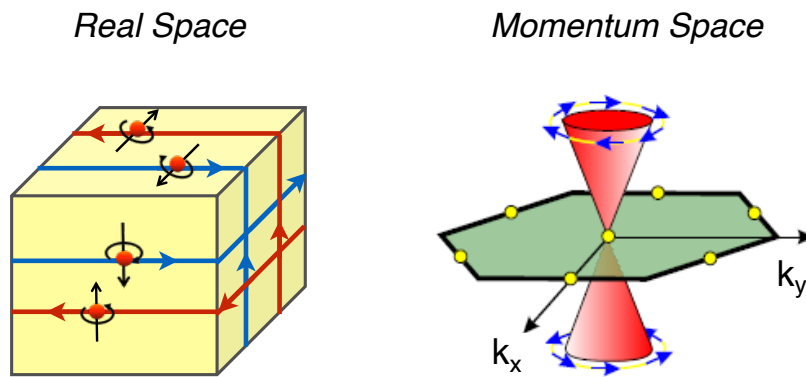


Figure 1.3.1: The topological insulator. Two-dimensional metallic topological surface states wrap around the three-dimensional bulk insulator. The surface states are spin-polarized and form time-reversed pairs so that opposite spins propagate in opposite directions with the spin orientation locked perpendicular to its direction of motion. In momentum space, these states form a (usually) single helically spin-polarized Dirac cone at the zone center that spans between the bulk valence and conduction bands. The Dirac cone is protected from opening a gap by time-reversal symmetry [Figure 1.2.2].

ure 1.3.1] and is protected from opening a gap by time-reversal symmetry [Figure 1.2.2]. Since there are no counter-propagating states of the same spin polarization, backscattering is forbidden in the absence of non-magnetic impurities. This leads to very high surface mobilities, on the order of $10,000 \text{ cm}^2/\text{V s}$ [23], making topological insulator materials very attractive candidates for use in future low power electronics applications. Because all currents running through the surface states are 100% spin-polarized, a large surface magnetization can be induced by a modest electrical current. These are the long-sought material properties necessary for various spin-based applications [24–27], such as a low power magnetization switch [25]. This and other topological insulator-based spintronic device architectures are currently being developed.

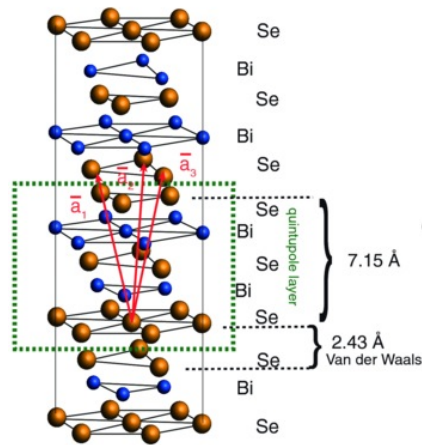
While the equilibrium properties of topological insulator surfaces are novel, even more exotic physics is predicted to emerge when a gap is induced at the Dirac point of the surface states. One way this can be done is by breaking time-reversal symmetry, which protects the Dirac point from opening a gap, by applying a magnetic field [24, 28, 29], introducing magnetic dopants [30, 31], or through a coherent light-matter interaction with circularly polarized light [32]. Once accomplished, several novel effects are predicted to occur, such as a half-integer surface quantum Hall effect [30], the observation of image magnetic monopoles [33], and a quantized Kerr rotation due to axion electrodynamics [34]—a concept borrowed from particle physics that causes the light electric and magnetic fields to become parallel. The other means of opening a gap is by inducing superconductivity, where Majorana fermions—a hy-

pothetical particle that is its own anti-particle—are predicted to emerge [35]. To date none of these exotic effects have been observed, largely due to the lack of high enough quality materials, which will be discussed later.

The first realistic topological insulator proposal was made by Fu and Kane in 2007 for the material $\text{Bi}_{1-x}\text{Sb}_x$ [22]. Later that year, Hsieh *et al.* confirmed its topological order by directly imaging the surface states using using angle-resolved photoemission spectroscopy (ARPES) [36]. Shortly thereafter, Bi_2Se_3 and Bi_2Te_3 were predicted and observed to be topological insulators as well [37, 38]. These have become the staple materials of the topological insulator community because they possess a single Dirac cone, as opposed to $\text{Bi}_{1-x}\text{Sb}_x$, which has five. To date there have been over 100 topological insulators predicted [39], many of which have been experimentally confirmed, all involving heavy elements from the bottom righthand corner of the periodic table that have suitably strong spin-orbit coupling.

Figure 1.3.2 (Left) shows the crystal structure for Bi_2Se_3 . It has a hexagonal crystal structure, as most topological insulator materials do, where the unit cell is a quintuple layer of alternating Se and Bi planes. Quintuple layers are van der Waals bonded at the Se-Se junctions, making these materials very cleavable to the point that they can be mechanically exfoliated to form small crystals of only a few nanometers thick [42]. Figure 1.3.2 (Right) shows an ARPES image of the Bi_2Se_3 topological surface states, where the single linearly dispersing Dirac cone

Crystal structure



Electronic structure

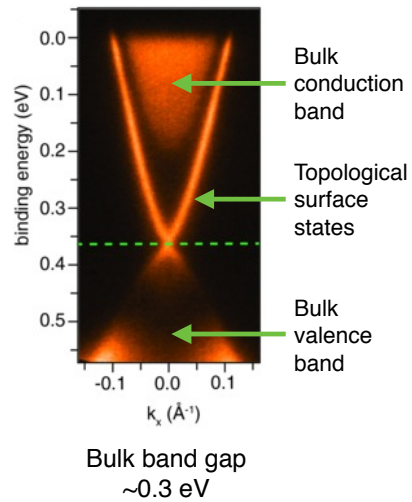


Figure 1.3.2: Bi_2Se_3 crystal and electronic structure. (Left) The prototypical topological insulator Bi_2Se_3 has a hexagonal crystal structure with a unit cell given by a quintuple layer of alternating Bi and Se planes that are van der Waals bonded at Se-Se junctures. Figure panel reprinted from [40]. (Right) ARPES image of the surface electronic structure, which is given by a single linearly dispersing Dirac cone that sits between the bulk valence and conduction bands. Figure panel reprinted from [40].

can be clearly seen connecting the bulk valance and conduction bands. Spin-polarized ARPES measurements have confirmed the helical spin texture of the surface states [43, 44]. Bi_2Se_3 is the most commonly studied topological insulator because it has one of the largest bulk band gaps (0.3 eV) of all the known topological insulator materials, and it has only a single Dirac cone, which simplifies things. Band gaps tend to be small in these materials ($\lesssim 0.3$ eV) owing to the fact that they are inverted gaps induced through spin-orbit coupling.

While there has been a lot of experimental progress made over the last few years in understanding topological insulators, the pace of discovery has nonetheless been slow given the large size of the field due to the lack of ideal materials. In most experiments, the bulk electronic response dominates over the surface contribution due to the characteristically small band gaps and intrinsic doping that occurs in real materials due to atomic vacancies [45]. For this reason, most of the more exotic proposals involving topological insulators have not been realized because they require having the Fermi level at the Dirac point. While in some situations this can be achieved through electrostatic gating [42], it has proven to be very difficult due to how highly doped most topological materials are, and cannot be used in all experimental conditions. This has also slowed progress on the applications end of the research spectrum, especially when compared to graphene, the only other known two-dimensional Dirac-like electron gas. More recently, new topological insulator materials such as $\text{Bi}_2\text{Te}_2\text{Se}$ and $\text{Bi}_{1.1}\text{Sb}_{0.9}\text{Te}_2\text{S}$ have emerged that have lower intrinsic doping and comparable band gaps to Bi_2Se_3 .

[39]. These materials have made isolating the surface contribution easier, but nonetheless still difficult and discovering more ideal topological insulator materials remains the largest challenge in the field.

The works presented in this thesis show how light can be used to study the electronic response of topological insulator surfaces, despite the high bulk carrier concentrations that occlude many experimental probes. In chapter 2, we show how polarized light can be used to selectively induce and control electron transport that is confined to the surface. In chapter 3, we demonstrate that the second harmonic generation of light from a topological insulator is a sensitive measure of various surface electronic properties.

This page is intentionally left blank

2

Optoelectronic manipulation of electrons on the surface of a topological insulator

THE SURFACE ELECTRONIC SPECTRUM of the topological insulator Bi_2Se_3 [37, 38] has been shown to be characterized by a single helical Dirac dispersion [47] that carries a Berry phase of π . This is a topologically non-trivial feature that dictates that counter-propagating electrons carry opposite spin. Hence, pure spin currents, which are a net flow of spin without a net flow of charge, propagate along the surfaces of a topological insulator in equilibrium [Figure 2.0.1]. These can be viewed as the

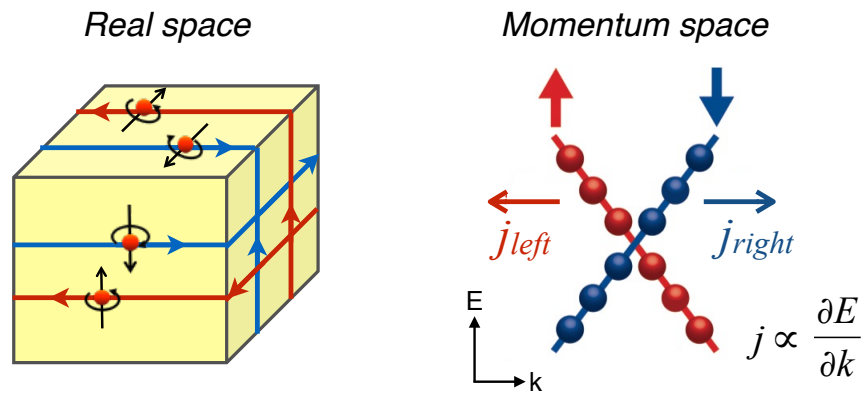


Figure 2.0.1: Topological insulator spin currents. Pure spin currents, which are a net flow of spin without a net flow of charge, propagate on the surfaces of a topological insulator in equilibrium. These can be viewed as the summation of two counter-propagating electrical currents of opposite spin polarization, where the total equilibrium charge current j_{total} is given by $j_{total} = j_{right} + j_{left} = 0$. The electrical current contribution carried by a given state is given by the slope of its energy-momentum dispersion $j \propto \partial E / \partial k$ [11]. Figure panel reprinted from [46].

summation of counter-propagating charge currents of equal magnitude and opposite spin polarization, so the total equilibrium charge current is zero. Applying a voltage between two electrical contacts deposited on the surface of a topological insulator tips this equilibrium balance so that one spin-polarized charge current dominates over the other, transforming the pure spin current into a 100% spin-polarized net electrical current that flows between the contacts. This, along with the extremely high surface electron mobilities that have been measured [23], are the long-sought material properties needed to realize many proposals for next-generation low-power technologies that rely on the electron spin degree of freedom as an information carrier [24–27]. However, a major experimental obstacle in developing these technologies

has been the high concentration of bulk charge carriers in Bi_2Se_3 and related materials that typically overwhelm the surface electrical response. Although transport results on electrically gated samples show evidence for surface carrier modulation [42], the contributions to the electrical response from carriers on different surfaces and in the bulk are difficult to separate and require highly insulating samples, which are difficult to produce.

2.1 THE CIRCULAR PHOTO GALVANIC EFFECT

In this chapter we demonstrate that optically driving a topological insulator out of equilibrium with circularly polarized light can generate a spin-polarized electrical current carried by the topological surface states without any applied voltage bias, even in highly doped samples [46]. This occurs through a process called the circular photogalvanic effect [48, 49]. The effect relies on the fact that circularly polarized light induces interband optical transitions with a probability that is sensitive to the electron spin orientation [44, 50], which is a property inherent in all materials for the following reason. The transition probability from an initial state $|i\rangle$ to a final state $|f\rangle$ in the electric dipole approximation, which usually dominates over all other types of optical transitions,

is given by Fermi's Golden Rule [51]

$$T_{i \rightarrow f} = \frac{2\pi}{\hbar} |\langle f | V | i \rangle|^2 \rho \quad (2.1)$$

where \hbar is the reduced Planck's constant, V is the operator for the electric dipole interaction between the initial and final states, and ρ is the density of final states. Light cannot directly couple to the electron spin via the electric dipole interaction, only to the orbital degree of freedom. However, since the selection rules mandate that at least one of the states involved in the transition has nonzero orbital angular momentum l (no s - to s -orbital transitions allowed, $\Delta l \neq 0$) [51], spin-orbit coupling is present and mixes the spin information with the orbital information. States of opposite spin polarization $m_s = \pm 1/2$ will mix with the orbital degree of freedom differently because one spin state will be primarily parallel and the other anti-parallel to the projected orbital quantum number m_l (except when $m_l = 0$). This makes the spin-orbit coupled wavefunctions used to calculate (2.1) distinct for spin-up and -down states, thus the transition probabilities can in general be expected to be different. This reasoning applies to both the initial and the final states, whichever has spin-orbit coupling (all non- s -orbitals).

Such spin-dependent optical transitions with circularly polarized light have been directly observed on the surface of Bi_2Se_3 using circular dichroism angle-resolved photoemission spectroscopy (ARPES) [Figure 2.1.1] [44]. Because surface states of opposite spin polarization disperse in

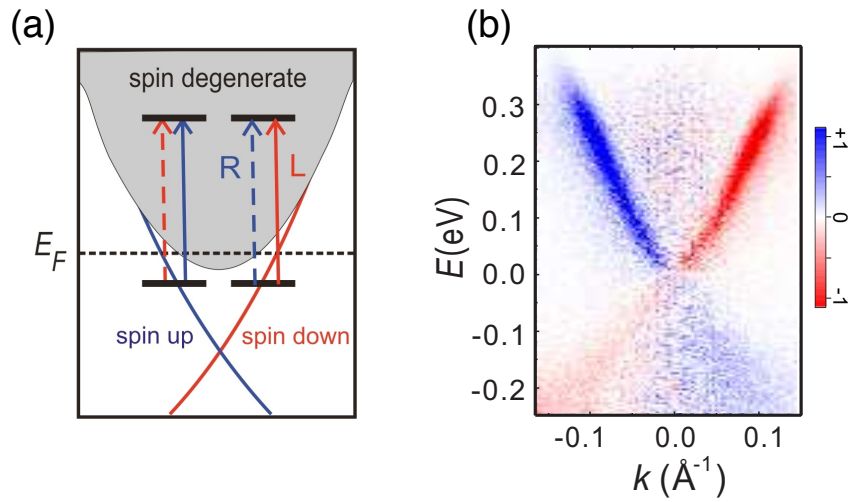


Figure 2.1.1: Spin-dependent optical transitions. (a) Circularly polarized light induces interband optical transitions from the topological surface states to spin-degenerate excited states with a probability that depends on the initial state's spin polarization. The same holds true exciting from occupied spin-degenerate states below the Dirac cone to unoccupied spin-polarized final states in the Dirac cone. (b) Circular dichroism ARPES energy-momentum cut showing that the oppositely dispersing branches of the surface Dirac cone can be preferentially depopulated by using different photon helicities. Figure panel reprinted from [44].

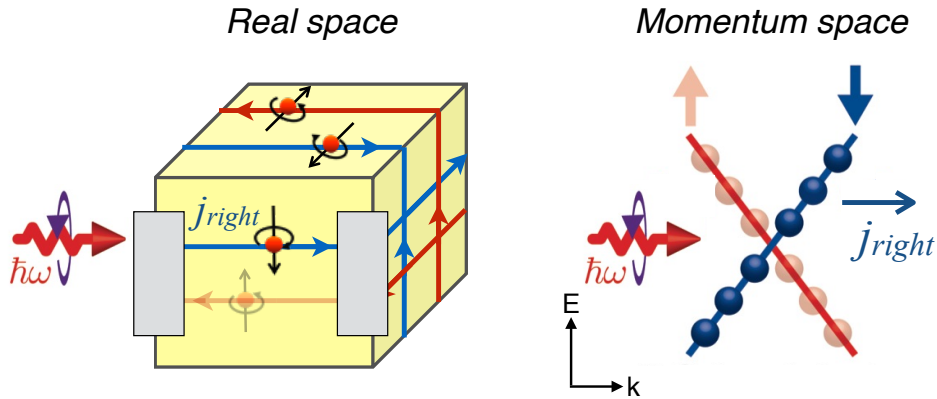


Figure 2.1.2: The circular photogalvanic effect. Spin-dependent transition probabilities for circularly polarized light allow for the Dirac cone to be asymmetrically depopulated (left moving spin-up states depopulated), creating a momentum imbalance that leads to a spin-polarized current to flow by those states not optically excited (right moving blue states). The excited states being populated by the optical transitions (not shown) also contribute to the total current measured (see main text). The grey strips represent contacts deposited on the surface to measure the photoinduced electrical current. Figure panel reprinted from [46].

opposite directions in momentum space to form the Dirac cone [Figure 2.0.1], it is observed that a given photon helicity preferentially excites one of these branches over the other to populate some excited state. This asymmetric momentum-dependent excitation of a Dirac system is a novel property unique to topological insulator surface states and quantum spin Hall edge states.

The asymmetric depopulation of the Dirac cone with circularly polarized light has novel consequences in that it creates a momentum imbalance that should result in spin-polarized current flow by those states not optically excited [Figure 2.1.2] [49]. This process is called the cir-

cular photogalvanic effect, which has been extensively studied in semiconductor quantum well systems where a spin-momentum dependent excitation can occur due to the momentum-dependent spin-splitting of the valance and conduction bands from Rashba spin-orbit coupling [see section 2.2.4] [52, 53]. Because the bulk bands of Bi_2Se_3 are spin-degenerate, these photon helicity-dependent currents can only be induced from the helical spin texture of the surface Dirac cone. The circular photogalvanic effect is furthermore forbidden in the bulk by crystal symmetry, which is discussed in section 2.3. This surface-specific method of generating and controlling spin-polarized electrical currents on the surface of a topological insulator is an appealing alternative to conventional transport techniques, where the surface contributions are dwarfed by the abundance of bulk carriers that are unavoidably generated in experiments. The circular photogalvanic effect can however also generate electrical current contributions from excited states when light of energy greater than the bulk band gap is used, which will be discussed in the next section. Bi_2Se_3 is generally highly electron doped, so the surface states will almost always be the initial states when considering optical transitions in the circular photogalvanic effect. However in topological insulators that are hole doped, circularly polarized light would instead populate the unoccupied topological surface states to generate a spin-polarized current.

This chapter reports the first experimental observation of the circular photogalvanic effect in a topological insulator [46]. The experimental results and analysis are presented in section 2.2. In section 2.3 we

present a phenomenological model that describes the circular photogalvanic effect and other photocurrent contributions by performing a crystal symmetry analysis.

2.2 OBSERVATION OF THE CIRCULAR PHOTOGALVANIC EFFECT IN THE TOPOLOGICAL INSULATOR Bi_2Se_3

This section is organized as follows. In section 2.2.1 we overview the sample growth, device fabrication, and the experimental apparatus used to generate and measure photocurrents in Bi_2Se_3 devices. Section 2.2.2 addresses thermoelectric currents generated in Bi_2Se_3 devices by laser heating. Section 2.2.3 reports the observation of the circular photogalvanic effect, as well as photocurrents generated via other mechanisms. Section 2.2.4 discusses and rules out alternative helicity-dependent photocurrent mechanisms. Section 2.2.5 presents additional measurements further characterizing photocurrents in Bi_2Se_3 .

2.2.1 SAMPLE GROWTH, DEVICE FABRICATION & PHOTOCURRENT DETECTION

Bi_2Se_3 single crystals were synthesized by melting a stoichiometric mixture of Bi and Se, where excess Se was used to compensate for the Se vacancies that give rise to bulk doping [54]. Specifically, the initial mixture of Bi:Se 2:4.06 was heated in a sealed quartz tube to 850°C where

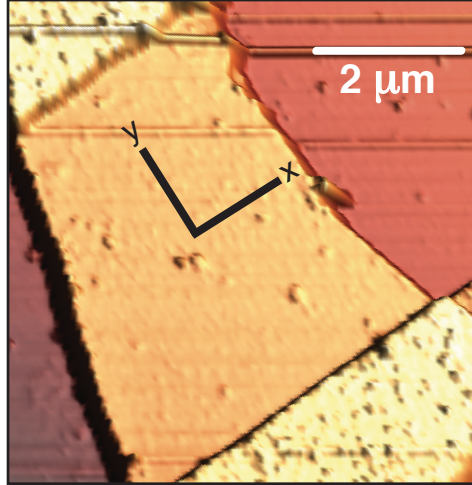


Figure 2.2.1: AFM image of Bi₂Se₃ device. A typical two-terminal exfoliated Bi₂Se₃ device used in experiments $\sim 120\text{nm}$ thick. The coordinate system referred to throughout the chapter is superimposed on the Bi₂Se₃ flake, and the edges of the contacts can be seen in the top left and bottom right corners of the image. Figure reprinted from [46].

it was kept for 48 hours. It was then cooled down over five days and annealed at 550°C for an additional five days. The resulting material was studied by low temperature (4K) magneto-transport and was found to be electron doped with a bulk carrier density (n) of $n \sim 2 \times 10^{17} \text{ cm}^{-3}$ and a bulk carrier mobility (μ) of $\mu \sim 6000 - 8000 \text{ cm}^2/\text{Vs}$. We note that the doping concentration in these materials increases due to the processing of nano-devices.

The devices were fabricated using a similar technique to that reported in [42]. An Atomic Force Microscopy (AFM) image of a typical device contacted in a two-terminal geometry is shown in Figure 2.2.1. The devices were fabricated by mechanically exfoliating Bi₂Se₃ flakes to a

nanometric thickness and depositing them on a SiO_2 surface. Bi_2Se_3 flakes measured in this study are 120 nm thick and typically 3.5 μm wide and 5 μm long. Suitable flakes of a smooth top surface were identified using optical and AFM imaging techniques. The flakes were contacted by evaporated electrodes (5 nm Ti, 100 nm Al) patterned using standard electron beam lithography procedures.

Figure 2.2.2(a) shows a block diagram of the experiment used to generate and detect photocurrents in Bi_2Se_3 devices. 80 fs pulses of 800 nm (1.5 eV) laser light are derived from a Ti:sapphire oscillator at a repetition rate of 80 MHz. The beam is chopped at 5 kHz for lock-in detection, then passed through an adjustable intensity (I) filter. A $\lambda/4$ waveplate is used to set the laser polarization, then the light is focused with a lens to a 100 μm spot size to completely illuminate a device. A 50x microscope objective and a high resolution CCD camera are used to align the device position to the center of the focused beam with an accuracy of $\sim 1 \mu\text{m}$. Alignment is done by adjusting the cryostat position, which is mounted on a three-axis translation stage. The induced photocurrents (j_y) are measured across unbiased exfoliated Bi_2Se_3 devices [Figure 2.2.2(b)]. The photocurrent signals are passed through a low noise current-to-voltage preamplifier, then into a lock-in for detection, which is synced to the chopper frequency. Polarization dependent photocurrents are identified by measuring j_y while rotating the $\lambda/4$ waveplate by an angle α , which varies the laser polarization with a 180° period from linearly P -polarized in the scattering plane ($\alpha = 0^\circ$),

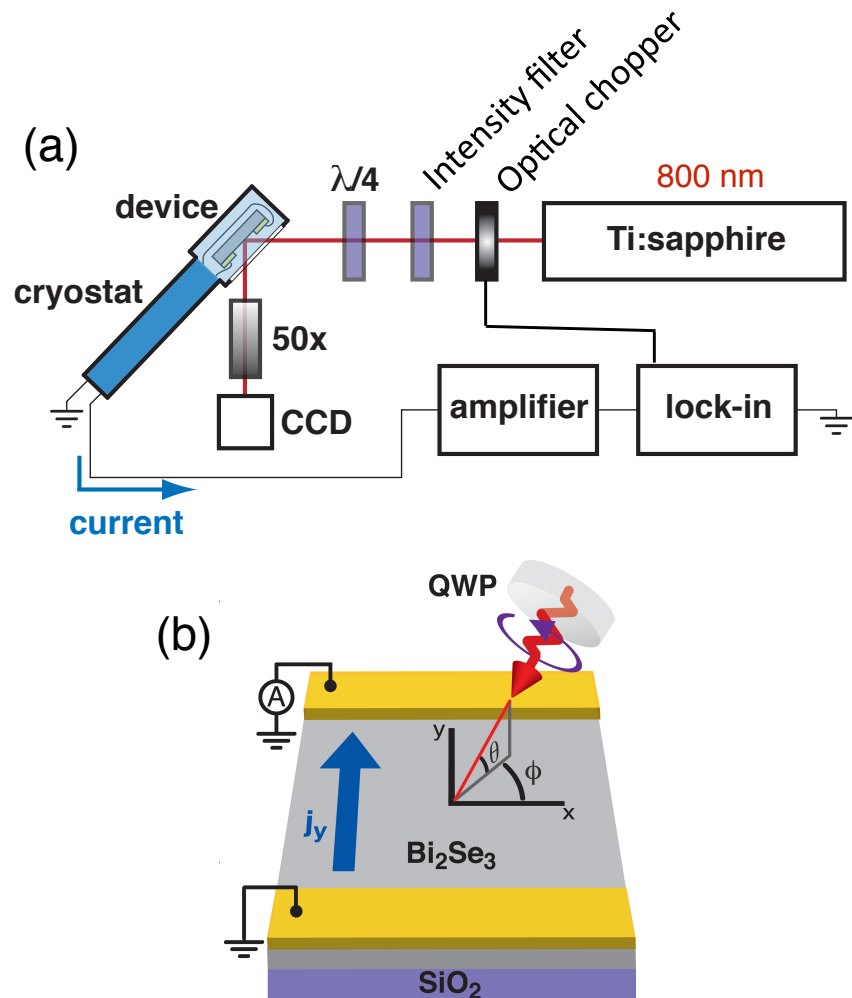


Figure 2.2.2: Photocurrent generation and detection. (a) Block diagram of the experimental layout. See main text for description. (b) Schematic of the experimental geometry. The laser beam is incident on the device at the out-of-plane angle Θ defined from the xy -plane and the in-plane angle Φ . Photon polarization varied by rotating the $\lambda/4$ waveplate (QWP) and photo-induced currents j_y are measured. Figure panel reprinted from [46].

to left-circular ($\alpha = 45^\circ$), to P ($\alpha = 90^\circ$), to right-circular ($\alpha = 135^\circ$), to P ($\alpha = 180^\circ$). Photocurrent data are corrected for small variations in laser intensity as a function of α due to $\lambda/4$ waveplate imperfections. The angle of incidence of light on a device is important for identifying various photocurrent contributions. The angles Θ and Φ [Figure 2.2.2(b)] are varied by adjusting the device position within the cryostat relative to the incident laser beam, which is fixed. Optical absorptivity measurements, which are presented in section 2.2.3, are performed by measuring the reflectivity on bulk single crystals of Bi_2Se_3 from the same material batch used to make devices.

2.2.2 THERMOELECTRIC PHOTOCURRENTS

Owing to the high thermoelectric power of Bi_2Se_3 [55], laser induced heat gradients in the sample can cause a bulk thermoelectric current background in addition to any photocurrents generated. To isolate the photocurrent response, we vary the heat gradient between the contacts by sweeping the laser spot position (y) across the Bi_2Se_3 device [Figure 2.2.3(a)] at a fixed polarization ($\alpha = 0^\circ$). We find that a current develops that switches polarity across the sample and is finite exactly at the center of the sample ($y = 0$). The contribution to j_y that switches polarity can be attributed to a thermoelectric current with electron-like carriers, which is consistent with our n-type native Bi_2Se_3 . On the other hand, the finite contribution to j_y at $y = 0$, where the sample is

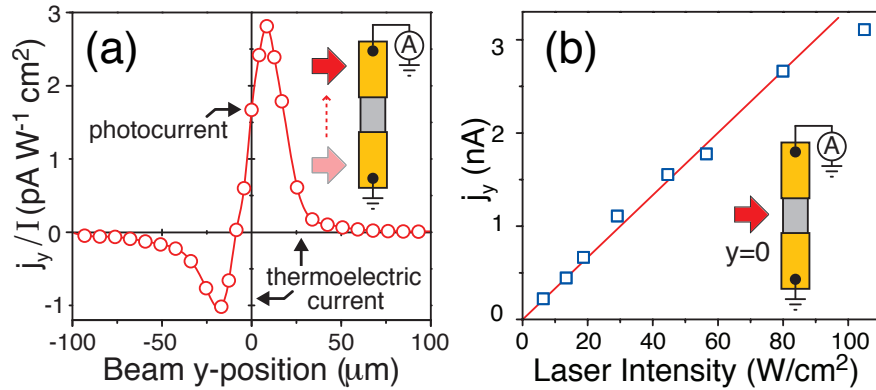


Figure 2.2.3: Thermoelectric currents and linear response. (a) j_y/I with light obliquely incident at $\Theta = 56^\circ$ in the xz -plane as a function of beam focus position y at room temperature where $y = 0$ is the center of the sample. (b) j_y as a function of laser intensity I at $y = 0$ at 15 K. Figure panels reprinted from [46].

evenly heated and the thermoelectric current should be minimal, can be attributed to a photocurrent that may encode aspects of the surface states' electronic response to light. Figure 2.2.3 (b) shows that this current scales linearly with laser intensity, which is a characteristic feature of a photocurrent [see section 2.2.5]. All subsequent measurements in section 2.2.3 are performed at $y = 0$ and in this low laser intensity regime ($I < 60 \text{ W/cm}^2$) where sample heating is minimized. Additional intensity dependence studies can be found in section 2.2.5.

2.2.3 POLARIZATION DEPENDENT PHOTOCURRENTS

To investigate the role of spin in generating the photocurrent, we measure the light polarization dependence of j_y at $y = 0$. Figure 2.2.4 shows that when light is obliquely incident in the xz -plane, j_y exhibits a strong polarization dependence that is comprised of four components

$$j_y(\alpha) = C\sin(2\alpha) + L_1\sin(4\alpha) + L_2\cos(4\alpha) + D \quad (2.2)$$

The coefficient C parameterizes a helicity-dependent photocurrent because rotating the $\lambda/4$ waveplate varies the light polarization between left- and right-circular with the functional form $\sin(2\alpha)$. The helicity-dependence indicates that C is generated through a spin-dependent process. This is because left- and right-circularly polarized light preferentially interact with opposite spin polarizations that are either aligned or anti-aligned to the light's wavevector [50], depending on the helicity [see section 2.1]. The other coefficients in (2.2) parameterize helicity-independent photocurrents that depend on the linear polarization of light (L_1 and L_2) and that are polarization-independent (D), which will be discussed later.

We now move to understand if the spin-mediated photocurrent C is generated by states in the helical Dirac cone through the circular photogalvanic effect. If this is the case, it should be possible to deduce the

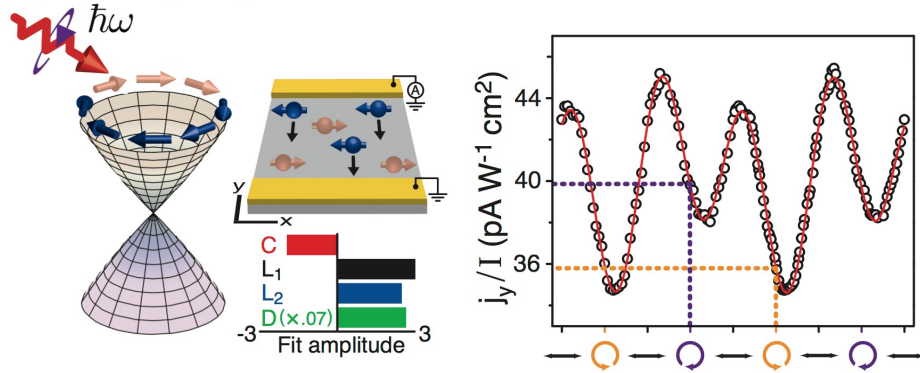


Figure 2.2.4: Photocurrent polarization dependence (xz-plane). $j_y(a)/I$ with light obliquely incident at $\Theta = 56^\circ$ in the xz -plane at 15K. The solid red line is a fit to (2.2) and the fit results are shown. Figure panels reprinted from [46].

surface state \mathcal{S} spin distribution by comparing the magnitude of C at different light angles of incidence. Because C is generated transverse to the light scattering plane (xz -plane) in Figure 2.2.4, the opposing \mathcal{S} spin polarizations that are excited by the different helicities must have a \mathcal{S} spin component in the xz -plane and be asymmetrically distributed along the y -direction in k -space. This is consistent with the helical \mathcal{S} spin distribution of the surface Dirac cone. Figure 2.2.5 shows that C becomes very small when light is obliquely incident in the yz -plane, such that the device contacts lie in the light scattering plane. This indicates that the electrons involved in generating C have a \mathcal{S} spin polarization that is locked perpendicular to their linear momentum, which is also consistent with the helical \mathcal{S} spin texture of the surface states. When light is normally incident, C completely vanishes [Figure 2.2.6], which is characteristic of an

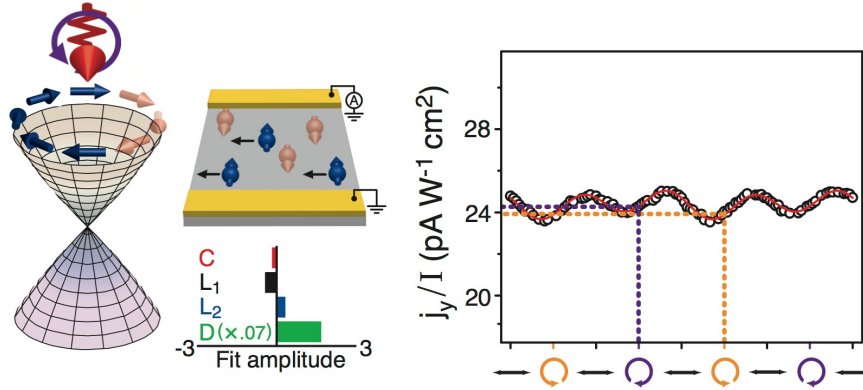


Figure 2.2.5: Photocurrent polarization dependence (yz-plane). $j_y(a)/I$ with light obliquely incident at $\Theta = 56^\circ$ in the yz-plane at 15K. The solid red line is a fit to (2.2) and the fit results are shown. Figure panels reprinted from [46].

in-plane spin distribution but is more fundamentally required to vanish by the in-plane rotational symmetry of Bi_2Se_3 [49]. Together these results reveal that the helicity-dependent photocurrent C arises from the asymmetric optical excitation of the helical Dirac cone through the circular photogalvanic effect.

Having identified that C arises from the Dirac cone, we seek to understand if the contributions L_1 , L_2 , and D in Figure 2.2.4 also share this origin. In general, the interband transition probabilities that set photocurrent magnitudes can be highly temperature (T) dependent owing to the thermal broadening of the Fermi distribution and small changes in the electronic structure due to changes in the electron-phonon coupling strength [56]. Therefore, to understand if L_1 , L_2 , and D are gov-

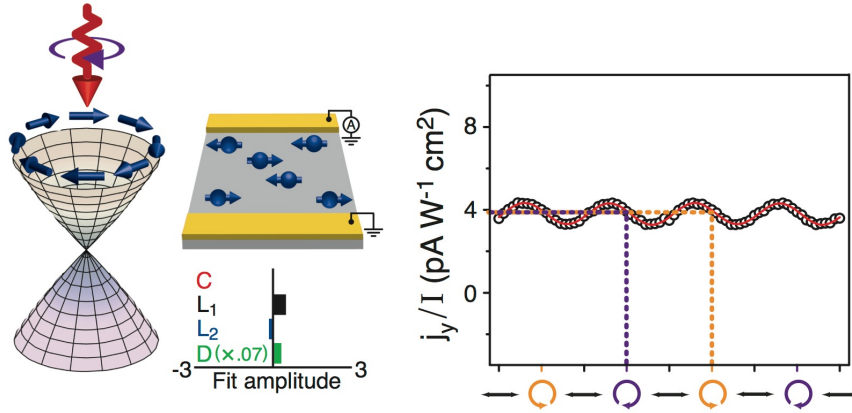


Figure 2.2.6: Photocurrent polarization dependence (normal incidence). $j_y(\alpha)/I$ with light normally incident at $\Theta = 90^\circ$ and $\Phi = 180^\circ$ so that the laser electric field is perpendicular to the contacts at $\alpha = 0^\circ$ at 15K. The solid red line is a fit to (2.2) and the fit results are shown. Figure panels reprinted from [46].

erned by the same interband transitions that give rise to C , we compare their detailed T dependence. The inset of Figure 2.2.7(a) shows that the fraction of incident photons absorbed by the sample, the absorptivity, exhibits a sharp decrease as T is raised from 15 K. This is generally consistent with the T dependences exhibited by C , L_1 , L_2 , and D [Figure 2.2.7(a)]. However, there are two clearly distinct sets of behavior: C and L_1 decrease monotonically to a constant and finite value between 60-293 K, whereas D and L_2 decrease identically to zero after undergoing a polarity reversal between 60-200 K. The similar behavior shared by L_1 and C strongly indicates that their generation mechanisms are deeply related and that L_1 may also have a Dirac cone origin. On the other hand, the D and L_2 photocurrents likely share a different origin.

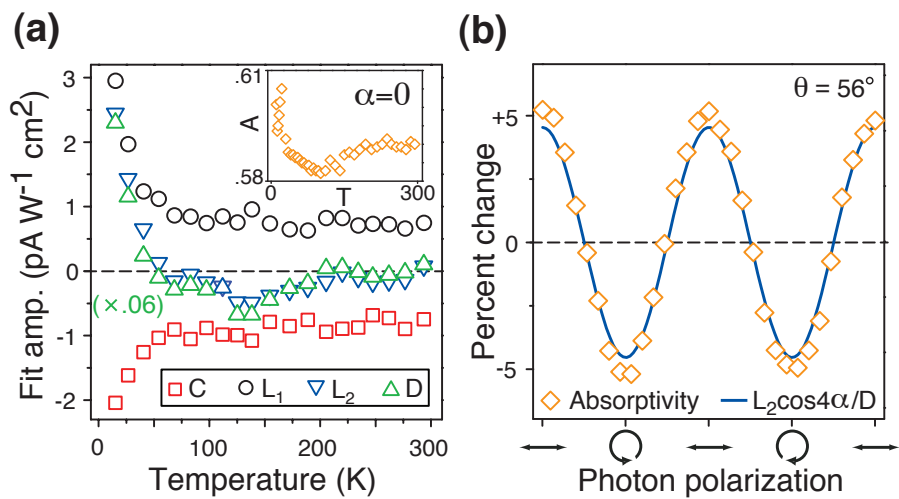


Figure 2.2.7: Photocurrent temperature dependence and absorptivity. (a) Fit results for $j_y(a)/I$ as a function of temperature for the geometry in Figure 2.2.4. Inset: Optical absorptivity as a function of temperature with P -polarized light ($a = 0$) at $\Theta = 56^\circ$. (b) Percent change of the absorptivity and $L_2 \cos(4a/D)$ as a function of photon polarization at room temperature. Figure panels reprinted from [46].

The origin of D and L_2 is revealed through the photon polarization dependence of the absorptivity, which exhibits only a $\cos(4\alpha)$ modulation [Figure 2.2.7(b)]. This is expected because the maxima of $\cos(4\alpha)$ describe when the incident light is P -polarized, which is the polarization that is generally absorbed most strongly by solids [57]. The modulation amplitude is approximately 5% of the α -independent background, which matches the percentage that the component $L_2 \cos(4\alpha)$ modulates the α -independent photocurrent D [Figure 2.2.7(b)]. This observation, together with their identical temperature dependence [Figure 2.2.7(a)], shows that L_2 is a trivial modulation of the photocurrent D . Because the polarization dependence of the absorptivity is representative of the bulk index of refraction [57], this is an indication that the photocurrent represented by D and L_2 likely has a bulk origin.

The observation of polarization-dependent photocurrents that stem from helical Dirac fermions (C and L_1) coexisting with a bulk photocurrent (D and L_2) in a topological insulator is novel and we elaborate on their possible microscopic mechanisms and topological significance below. The similar behavior of the photocurrent contributions L_1 and C in Figure 2.2.7(a) suggests that L_1 also arises from an asymmetric depopulation of the surface Dirac cone. This is supported by recent ARPES measurements on Bi_2Se_3 showing that linearly polarized light does in fact couple differently to opposite branches of the Dirac cone depending on the crystal orientation [44]. Such linear photogalvanic effects have also been observed alongside circular photogalvanic effects in semiconductor quantum wells [52, 53]. It has been shown theoret-

cally in these systems that the two photogalvanic effects are linked and that their combined magnitude is a measure of the spin texture's trivial Berry phase [58, 59]. Photogalvanic currents have similarly been predicted to be a measure of the non-trivial Berry phase in topological insulators [49]. However, determining the Berry phase requires a quantitative measure of the Dirac cone contribution alone. This is challenging because the depopulation of the Dirac cone using high energy light necessarily implies a population of bulk-like excited states, which may also carry a net photogalvanic current [Figure 2.2.8(a)]. Eliminating these contributions will be possible when more insulating samples become available and by extending these measurements into the lower energy (sub-bulk gap) THz radiation regime so that only inter-band transitions within the Dirac cone occur [49]. While Rashba spin-split quantum well states have been observed in the inversion layer of some Bi_2Se_3 samples their relative contribution to circular photogalvanic effect can be expected to be small [section 2.2.4]. This is because circular photogalvanic effect from Rashba spin-split bands will have an inherent cancellation effect (two competing spin distributions) that is absent in the topological surface states (one spin distribution) and because the inversion layer depth is comparable to the surface state penetration depth [section 2.2.4].

The bulk nature of the photocurrent described by D and L_2 [Figure 2.2.7(b)] precludes a photogalvanic origin because the photogalvanic effect is only permitted at the surface of Bi_2Se_3 where spin-splitting is

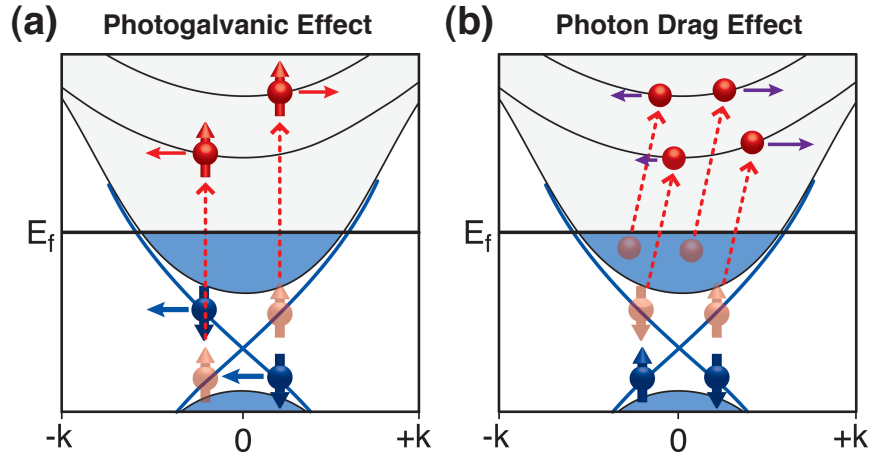


Figure 2.2.8: Microscopic mechanisms of photocurrent generation. (a) k -space depiction of photon helicity-induced currents from the Dirac cone via the circular photogalvanic effect including contributions from excited states. (b) k -space depiction of photon drag. The optical transition arrows are tilted to account for the transfer of linear photon momentum. Figure panels reprinted from [46].

present in the electronic structure. This must therefore be due to a different mechanism that is allowed in the bulk called the photon drag effect [60–63]. Photon drag describes photocurrents that result from the transfer of linear momentum from incident photons to excited carriers [Figure 2.2.8(b)], thus permitting a photocurrent even if states are symmetrically distributed in k -space. Helicity-independent photon drag photocurrents generated transverse to the direction of momentum transfer, consistent with what we observe, have been attributed in conventional semiconductors to an aspheric bulk band structure [62], which is also present in Bi_2Se_3 . Recently, a new helicity-dependent form of photon drag was observed alongside photogalvanic photocurrents in a quantum well system [53]. It was proposed that the photon mo-

momentum transfer opened a spin-dependent relaxation channel in the spin-split valence band that created a spin-polarized current. A similar process may be able to take place on the surface of a topological insulator where the required spin-splitting is provided by the Dirac cone. However, the bulk spin-degeneracy of Bi_2Se_3 forbids this mechanism in the bulk and makes any other helicity-dependent photocurrents in the bulk highly unlikely [64]. While a photo-induced inverse spin Hall effect has been observed in GaAs and related materials, the exceptionally short spin lifetime of bulk optically spin oriented carriers will make contributions from this effect very small [section 2.2.4].

Our measurements show that the topological insulator's non-trivial band topology can give rise to a novel non-equilibrium electronic response. The photocurrents observed are only one of many possible non-equilibrium properties of a topologically ordered phase [48, 49, 65–67] and there are features in our data that call for a detailed theoretical treatment. In addition to the possibility of measuring fundamental physical quantities, like the Berry phase [49, 58, 59], optically induced currents provide a promising route to generate and control spin-polarized currents at an isolated surface or buried interface, which could be harnessed for spintronic applications [26].

2.2.4 RULING OUT ALTERNATIVE PHOTOCURRENT MECHANISMS

Below we rule out two alternative photocurrent mechanisms that could explain the observed photon helicity dependence.

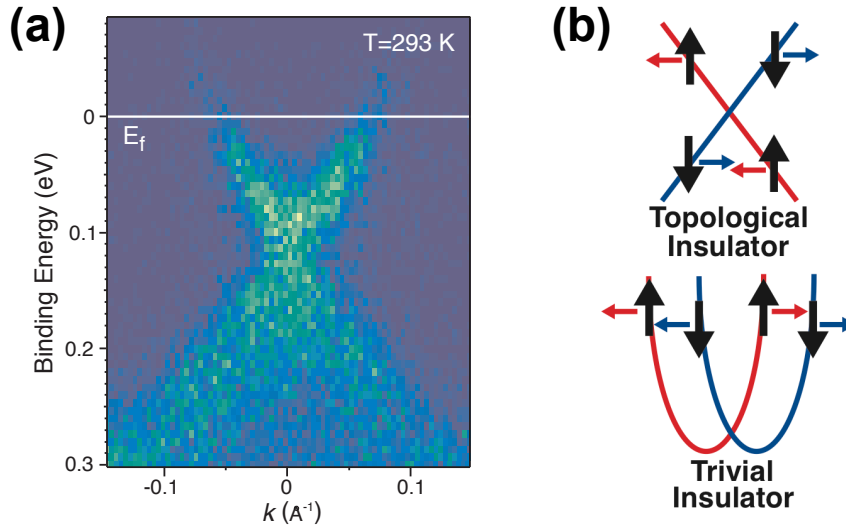


Figure 2.2.9: Absence of Rashba-split states. (a) ARPES spectrum of the Bi_2Se_3 material used to fabricate devices revealing the absence of Rashba-split states in ultra-high vacuum. (b) Comparison of Rashba-split quantum well states and topological surface states. Circular photogalvanic effect currents induced in Rashba-split states experience a cancellation effect that is absent in the linearly dispersing surface states. Figure panels reprinted from [46].

THE CIRCULAR PHOTO GALVANIC EFFECT FROM RASHBA-SPLIT QUANTUM WELL STATES IN THE INVERSION LAYER

The circular photogalvanic effect has been observed from Rashba spin-split states in quantum well structures [52, 53]. Similar states have been observed using ARPES in the surface inversion layer of Bi_2Se_3 samples that were intentionally surface electron doped by depositing specific gases or metals on the surface [68–70]. To check for these states, we performed ARPES measurements on the Bi_2Se_3 material used to make devices [Figure 2.2.9(a)]. The spectrum was taken in ultrahigh vacuum

and at room temperature several hours after the sample was cleaved to approximate the band-bending that occurs in air. We find no evidence of Rashba-splitting. The Fermi level is approximately 120 meV above the Dirac point. Rashba-split states typically do not appear until the surface Fermi level is doped to around 600 meV above the Dirac point [68–70].

While we find no evidence of Rashba-splitting in samples cleaved in ultrahigh vacuum, we acknowledge that the device fabrication process does electron dope our material. However, even if the doping during fabrication were sufficient to induce Rashba-splitting in the inversion layer, the circular photogalvanic effect contribution from these states can be expected to be small in comparison to that from the surface states. This is because currents induced by changing the spin-density in Rashba spin-split systems (such as through the circular photogalvanic effect, electrical spin-injection etc.) will largely cancel because there are two spin distributions that generate competing currents. The magnitude of the net current will be proportional to the spin-splitting, which is only a fraction of the Fermi momentum k_f [Figure 2.2.9(b)]. Topological surface states, on the other hand, have a single helical spin distribution, so there is no cancellation effect, with a current magnitude that is proportional to the effective spin-splitting across the Dirac cone, which is $2k_f$. For this reason, topological surface states are generally expected to have a much larger spin-density induced current than Rashba systems [27, 48]. However, if the depth that the inversion layer penetrated into the bulk were very large, it is true that the circular pho-

totalgalvanic effect from these states could dominate our signal. We estimate the depth that the Rashba-split states would penetrate into the bulk if they were present in our material. We typically measure a bulk carrier density of $n \sim 5 \times 10^{18} \text{ cm}^{-3}$ in our exfoliated Bi_2Se_3 flakes patterned in a Hall bar device geometry. From this and the reported values for the average effective mass and dielectric constant [54] we estimate that the inversion layer thickness is only $\sim 2 \text{ nm}$ using the Thomas-Fermi screening length as an approximation. This is comparable to the depth (d) that the surface state penetrate into the bulk, which is roughly $d = \hbar v_f / \Delta \sim 1 \text{ nm}$, where v_f is the surface state Fermi velocity and Δ is the bulk band gap. This shows that the cumulative circular photogalvanic effect contribution from Rashba-split states over the entire inversion layer depth can still be expected to be small.

PHOTO-INDUCED INVERSE SPIN HALL EFFECT

A photoinduced inverse spin Hall effect has been observed in bulk GaAs [26, 71]. In this effect, optically spin oriented electrons excited on the surface diffuse into the bulk and undergo spin-dependent scattering to generate a helicity-dependent photocurrent. This effect can occur in GaAs because of the unique nature of its spin-orbit coupling. The spin-orbit coupled valance band permits the optical spin orientation of electrons excited to the conduction band by circularly polarized light. Owing to the s-orbital nature (zero spin-orbit coupling) of the conduction band, the spin lifetime of these electrons is exceptionally long, on the

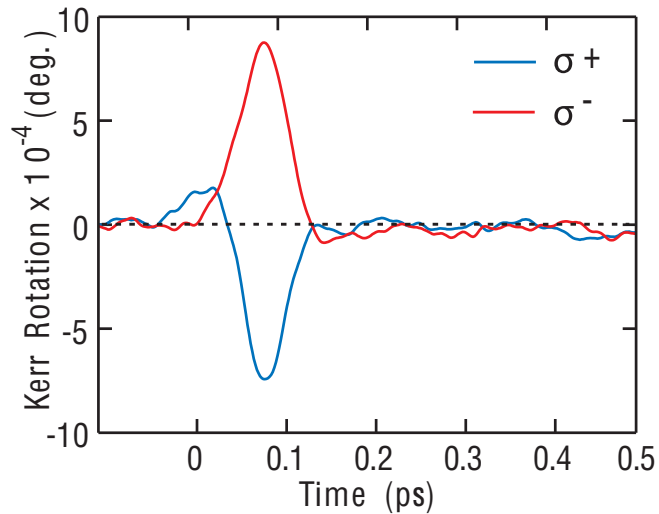


Figure 2.2.10: Ultrafast bulk spin relaxation. Time-resolved Kerr rotation spectroscopy measurement on the same Bi_2Se_3 material used to fabricate devices. A 100 fs circularly polarized pump pulse of 800 nm laser light creates a non-equilibrium bulk state spin polarization. The spin relaxation dynamics are probed by monitoring the Kerr rotation of a time-delayed linearly polarized probe pulse. σ^+ and σ^- represent left- and right-circular polarizations respectively. Figure panel reprinted from [46].

order of 10-100 ns [72]. This is long enough for optically excited carriers on the surface to diffuse into the bulk while retaining their spin polarization. Spin-dependent scattering can then occur to generate a spin Hall effect current.

In materials such as Bi_2Se_3 , any photoinduced spin-polarized bulk states will rapidly depolarize before significant diffusion can occur. This is because both the initial and final states are spin-orbit coupled (p-orbital nature), in contrast to GaAs, which greatly reduces the spin life-

time of excited carriers. To show that this is the case, we performed time-resolved Kerr rotation spectroscopy measurements on the same material used to fabricate devices [Figure 2.2.10]. A more extensive study was performed in [73]. We find that the spin polarization of optically oriented bulk carriers completely depolarizes in <100 fs, which is the resolution limit of our measurement. This is 5-6 orders of magnitude shorter than the spin-lifetime in GaAs and short enough that any carrier diffusion from the surface into the bulk can be expected to have a negligible spin polarization. Contributions from the photo-induced inverse spin Hall effect can therefore be expected to be very small in Bi_2Se_3 . Furthermore, the presence of the photocurrent L_1 that appears to be linked to the helicity-dependent current C [Figure 2.2.7(a)] cannot be accounted for by this effect.

2.2.5 ADDITIONAL PHOTOCURRENT MEASUREMENTS

This section provides additional characterization of the photocurrents reported in section 2.2.3.

DEVIATION FROM LINEAR PHOTOCURRENT RESPONSE AT HIGHER LASER INTENSITIES

As shown by (2.3) in the next section, photocurrents are expected to scale quadratically with the ac electric field of the incident light, which

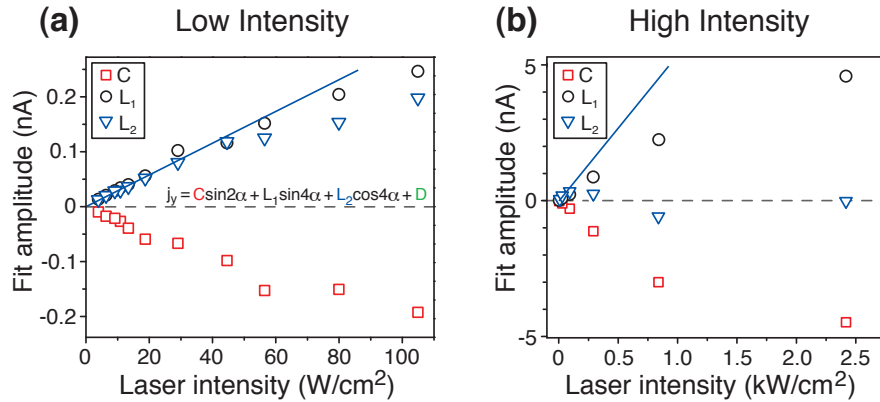


Figure 2.2.11: Laser intensity dependence of photocurrents. Photocurrent $j_y(a)$ fit amplitudes in the Figure 2.2.4 geometry over a broad range of laser intensities at 15 K. (a) Low intensity regime. (b) High intensity regime. The blue line is drawn to highlight the sub-linear behavior at high intensities. Figure panels reprinted from [46].

is to say that they scale linearly with the laser intensity. Figure 2.2.3(b) shows that $j_y(a = 0)$ scales linearly with laser intensity up until around $I = 60 \text{ W/cm}^2$, below which is the low intensity regime where all reported photocurrent measurements were performed. Here we show the intensity dependence of the corresponding polarization dependent fit coefficients C , L_1 and L_2 from (2.2) over a broad range of laser intensities. Figure 2.2.11(a) shows that their amplitudes likewise begin to deviate from the expected linear scaling when intensities of greater than $I = 60 \text{ W/cm}^2$ are used, and become highly sub-linear at even greater intensities [Figure 2.2.11(b)]. These behaviors may be attributed to a combination of multi-photon absorption processes, the saturation of certain interband transitions, and a temperature increase caused by excessive laser heating. The last-mentioned is likely responsible for the

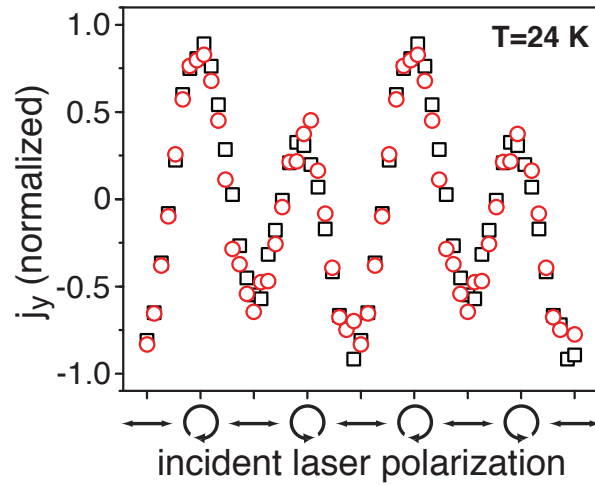


Figure 2.2.12: Continuous wave vs pulsed laser excitation. Photocurrent $j_y(a)$ taken with pulsed (red circles) and continuous wave (black squares) 800 nm laser light. Traces were taken in the Figure 2.2.4 geometry at 24 K and were normalized to account for the small laser intensity changes that accompany changing the laser emission mode, which slightly modify the current amplitude, to highlight the identical polarization dependence. Figure reprinted from [46].

sub-linearity since Figure 2.2.7 shows that the photocurrent amplitudes decrease as the temperature is increased. This is further evidenced by the sign reversal of L_2 in Figure 2.2.11 (b), which likewise occurs in the temperature dependence. It is therefore necessary that all photocurrent measurements on Bi_2Se_3 be performed at low laser intensities.

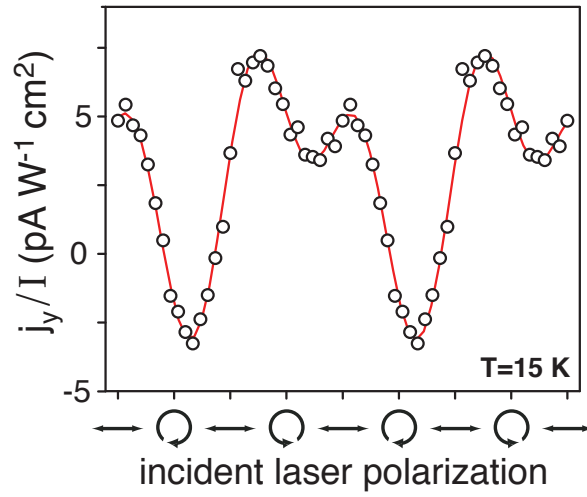


Figure 2.2.13: Consistent results across multiple devices. Photocurrent $j_y(a)/I$ measured on a different device in the Figure 2.2.4 geometry at 15 K. Figure reprinted from [46].

IDENTICAL PHOTOCURRENT RESPONSE BY CONTINUOUS WAVE AND PULSED LASER EXCITATION

While pulsed laser light is standardly used to induce polarization dependent photocurrents in quantum well structures [52], we confirmed independently that the pulsed nature of the light does not influence $j_y(a)$. Figure 2.2.12 shows that traces taken with continuous wave laser light and pulsed laser light of the same wavelength are virtually identical.

CONSISTENT RESULTS ACROSS MULTIPLE DEVICES

To confirm that the photon polarization induced currents observed are consistent across multiple devices, a second device of similar dimensions was characterized [Figure 2.2.13]. The photocurrent response $j_y(\alpha)$ of the second device proved to be qualitatively similar to the data reported in the main text. The slight differences between the signals may be due to a different crystal axes orientation relative to the contacts, which could affect the relative photocurrent magnitudes as discussed in the next section.

2.3 PHENOMENOLOGICAL DESCRIPTION OF PHOTOCURRENTS IN $\text{Bi}_2\text{Se}_3(111)$

In this section we derive the phenomenological equations governing the photon drag and photogalvanic effects in $\text{Bi}_2\text{Se}_3(111)$ using purely symmetry analysis. These results can be used to identify photocurrent contributions in all topological insulator materials that share the same crystal symmetry as $\text{Bi}_2\text{Se}_3(111)$. We find that the photon drag effect is allowed in the bulk of the material, whereas the photogalvanic effect can only arise from the surface. The dominant dc current response \vec{j} to an oscillating electromagnetic field with complex electric field compo-

ment $\vec{E}(\vec{q}, \omega)$ is given by [52]

$$j_\lambda(\mathbf{o}, \mathbf{o}) = \sigma_{\lambda\nu\eta}(\vec{q}, \omega) E_\nu(\vec{q}, \omega) E_\eta^*(\vec{q}, \omega) \quad (2.3)$$

where $\sigma_{\lambda\nu\eta}(\vec{q}, \omega)$ is a photocurrent conductivity tensor, the indices run through three spatial coordinates x, y and z in the laboratory frame, \vec{q} is the photon linear momentum, and ω is the photon frequency. Expanding the second order conductivity $\sigma_{\lambda\nu\eta}(\vec{q}, \omega)$ to linear order in \vec{q} , we find that

$$\sigma_{\lambda\nu\eta}(\vec{q}, \omega) = \sigma_{\lambda\nu\eta}(\mathbf{o}, \omega) + \Phi_{\lambda\mu\nu\eta}(\omega) q_\mu \quad (2.4)$$

The first and second terms, dubbed the photogalvanic and photon drag effects respectively, differentiate between optical processes that do not and do involve the transfer of linear momentum from the incident photons to the excited electrons as a means of generating an electrical current. Because j_λ is odd under the operation of space inversion symmetry but the square of the electric field is even, the tensor $\sigma_{\lambda\nu\eta}(\mathbf{o}, \omega)$ has non-zero components only for systems that break inversion symmetry. Therefore, in an inversion-symmetric material such as Bi_2Se_3 (space group D_{3d}^5) [49], photogalvanic effects are only allowed at the surface where the symmetry is reduced to C_{3v} . Photon drag effects, on the other hand, are described by a higher-order conductivity tensor $\Phi_{\lambda\mu\nu\eta}(\omega)$ that has an even rank. Because even rank tensors may have

non-zero components in inversion-symmetric systems, photon drag is permitted by symmetry to exist in the bulk of Bi_2Se_3 . Because both $\sigma_{\lambda\nu\eta}(\mathbf{o}, \omega)$ and $\Phi_{\lambda\mu\nu\eta}(\omega)$ may have off-diagonal elements, photocurrent magnitudes may differ along different crystal axes. While this analysis does not guarantee the presence of a particular photocurrent class, it serves as a useful guide for identifying potential contributions. In the following sections we will discuss these two effects separately.

2.3.1 LINEAR AND CIRCULAR PHOTOGALVANIC EFFECTS IN $\text{Bi}_2\text{Se}_3(111)$

In this section we derive the phenomenological equations governing the linear photogalvanic effect (LPGE) and circular photogalvanic effect (CPGE) in $\text{Bi}_2\text{Se}_3(111)$. The dominant dc current response \vec{j} to an oscillating electromagnetic field that neglects photon momentum is given by

$$j_\lambda(\mathbf{o}, \mathbf{o}) = \sigma_{\lambda\nu\eta}(\mathbf{o}, \omega) E_\nu(\vec{q}, \omega) E_\eta^*(\vec{q}, \omega) \quad (2.5)$$

where $\sigma_{\lambda\nu\eta}$ is a complex third-rank tensor and the indices run through three spatial coordinates x, y and z in the laboratory frame. Because $\sigma_{\lambda\nu\eta}$ has non-zero components only for systems that break inversion symmetry, photogalvanic effects cannot arise in the bulk of Bi_2Se_3 (space group D_{3d}^5) and must instead solely arise from the surface. Since \vec{j} must be real, it has been shown [49] that (2.5) can be separated into the fol-

lowing form

$$j_\lambda = i\gamma_{\lambda\beta}(\vec{E} \times \vec{E}^*)_\beta + \chi_{\lambda\mu\nu} \frac{E_\mu E_\nu^* + E_\mu^* E_\nu}{2} \quad (2.6)$$

where $\gamma_{\lambda\beta}$ is a second-rank pseudo-tensor composed of the part of $\sigma_{\lambda\mu\nu}$ that is antisymmetric under exchange of the last two indices μ and ν and $\chi_{\lambda\mu\nu}$ is the symmetric part of $\sigma_{\lambda\mu\nu}$. The first term on the right hand side is proportional to the helicity of incoming circularly polarized light and represents the CPGE. The second term is sensitive to the linear polarization of light and represents the LPGE. Because both the CPGE and LPGE only occur at the surface of Bi_2Se_3 , the tensors $\gamma_{\lambda\beta}$ and $\chi_{\lambda\mu\nu}$ must be invariant under the crystal symmetries of the (111) surface.

At the (111) surface of Bi_2Se_3 , the crystal symmetry is reduced from D_{3d}^5 to C_{3v} , which consists of a three-fold rotational symmetry about the axis (\hat{z}) normal to the (111) surface, and mirror symmetry about the $x'z'$ -plane as well as planes rotated by $2\pi/3$ and $4\pi/3$ from the xz -plane [Figure 2.3.1]. Here the primed coordinates refer to the crystal axes. In this space group, the tensor $\gamma_{\lambda\beta}$ has only one non-zero component $\gamma_{x'y'} = -\gamma_{y'x'} \equiv \gamma$. $\chi_{\lambda\mu\nu}$ has four non-zero independent components $\chi_{x'x'x'} = \chi_{x'y'y'} = -\chi_{y'x'y'} \equiv \chi_1$, $\chi_{x'x'z'} = \chi_{y'y'z'} \equiv \chi_2$, $\chi_{z'x'x'} = \chi_{z'y'y'} \equiv \chi_3$ and $\chi_{z'z'z'} \equiv \chi_4$. We note that $\chi_{\lambda\mu\nu}$ is isomorphic to the nonlinear susceptibility tensor for optical second harmonic generation [section 3.1.1]. In our experiments, the contacts that measure \vec{j} are arbitrarily oriented relative to the in-plane crystallographic di-

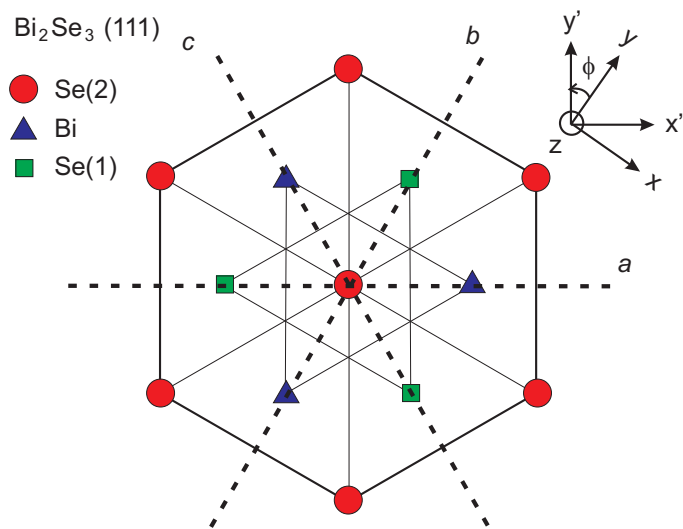


Figure 2.3.1: C_{3v} symmetry of the Bi_2Se_3 (111) cleaved surface. The three-fold rotation symmetry and the three planes of mirror symmetry (a , b and c) are illustrated. The topmost, second and third atomic layers are Se(2), Bi and Se(1) respectively. The relationship between the crystal (primed) and beam (un-primed) coordinates are shown in the top right. Figure reprinted from [74].

reflections. Under a rotation of φ about the \hat{z} -axis, $\gamma_{\lambda\beta}$ remains invariant while $\chi_{\lambda\mu\nu}$ becomes

$$\left(\begin{array}{c} \left(\begin{array}{c} \chi_1 \cos 3\varphi \\ \chi_1 \sin 3\varphi \\ \chi_2 \end{array} \right) \\ \left(\begin{array}{c} \chi_1 \sin 3\varphi \\ -\chi_1 \cos 3\varphi \\ \circ \end{array} \right) \\ \left(\begin{array}{c} \chi_3 \\ \circ \\ \circ \end{array} \right) \end{array} \right) \left(\begin{array}{c} \left(\begin{array}{c} \chi_1 \sin 3\varphi \\ -\chi_1 \cos 3\varphi \\ \circ \end{array} \right) \\ \left(\begin{array}{c} -\chi_1 \cos 3\varphi \\ -\chi_1 \sin 3\varphi \\ \chi_2 \end{array} \right) \\ \left(\begin{array}{c} \circ \\ \chi_3 \\ \circ \end{array} \right) \end{array} \right) \left(\begin{array}{c} \left(\begin{array}{c} \chi_2 \\ \circ \\ \circ \end{array} \right) \\ \left(\begin{array}{c} \circ \\ \chi_2 \\ \circ \end{array} \right) \\ \left(\begin{array}{c} \circ \\ \circ \\ \chi_4 \end{array} \right) \end{array} \right)$$

This means that the CPGE is isotropic with respect to the in-plane orientation of the (111) surface whereas the LPGE is anisotropic. In our experiments, a laser beam polarized either parallel to (P) or perpendicular to (S) the scattering plane propagates through a wave-plate (either $\lambda/2$ or $\lambda/4$) and impinges on the sample at an angle θ with respect to the normal. Current along either the x or y direction is then measured as a function of the angle α between the optical axis of the wave-plate and the scattering plane [Figure 2.3.2]. Below we study the functional form of these photocurrents under the various experimental geometries in detail.

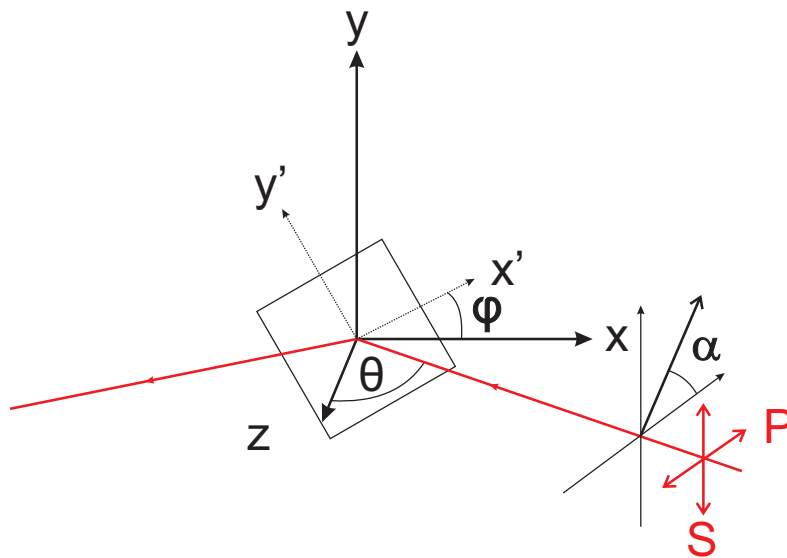


Figure 2.3.2: Experimental geometry for photocurrent measurements.
 The angles are defined as follows: ϕ is the angle between the in-plane crystal coordinates and the lab coordinates, α is the angle of the wave-plate optical axis with respect to the scattering plane, and θ is the angle of incidence.

OBLIQUE INCIDENCE WITH P-POLARIZED LIGHT THROUGH A $\lambda/2$ WAVEPLATE

In this experimental geometry, the light incident on the sample is always linearly polarized with polarization $\vec{E} = E_o(\cos 2\alpha \cos \theta, \sin 2\alpha, -\cos 2\alpha \sin \theta)$. Therefore only the second term in (2.6) survives and the photogalvanic current becomes

$$\begin{aligned} j_x &= -1/2\chi_1 \cos 3\varphi + 1/2(\chi_1 \cos^2 \theta \cos 3\varphi - \chi_2 \sin 2\theta) \\ &+ \cos 4\alpha [1/2\chi_1 \cos 3\varphi + 1/2(\chi_1 \cos^2 \theta \cos 3\varphi - \chi_2 \sin 2\theta)] \\ &+ \sin 4\alpha (\chi_1 \cos \theta \sin 3\varphi) \end{aligned} \quad (2.7)$$

$$\begin{aligned} j_y &= -1/2\chi_1 \sin 3\varphi + 1/2\chi_1 \cos^2 \theta \sin 3\varphi \\ &+ \cos 4\alpha (1/2\chi_1 \sin 3\varphi + 1/2\chi_1 \cos^2 \theta \sin 3\varphi) \\ &- \sin 4\alpha (\chi_1 \cos \theta \cos 3\varphi + \chi_2 \sin \theta) \end{aligned} \quad (2.8)$$

OBLIQUE INCIDENCE WITH S-POLARIZED LIGHT THROUGH A $\lambda/2$ WAVEPLATE

In this experimental geometry, the light incident on the sample is always linearly polarized with polarization $\vec{E} = E_o(\sin 2\alpha \cos \theta, -\cos 2\alpha, -\sin 2\alpha \sin \theta)$. Again only the second term in (2.6) survives and the photogalvanic current becomes

$$\begin{aligned}
j_x &= -1/2\chi_1 \cos 3\varphi + 1/2(\chi_1 \cos^2 \theta \cos 3\varphi - \chi_2 \sin 2\theta) \\
&- \cos 4a[1/2\chi_1 \cos 3\varphi + 1/2(\chi_1 \cos^2 \theta \cos 3\varphi - \chi_2 \sin 2\theta)] \\
&- \sin 4a(\chi_1 \cos \theta \sin 3\varphi) \tag{2.9}
\end{aligned}$$

$$\begin{aligned}
j_y &= -1/2\chi_1 \sin 3\varphi + 1/2\chi_1 \cos^2 \theta \sin 3\varphi \\
&- \cos 4a(1/2\chi_1 \sin 3\varphi + 1/2\chi_1 \cos^2 \theta \sin 3\varphi) \\
&+ \sin 4a(\chi_1 \cos \theta \cos 3\varphi + \chi_2 \sin \theta) \tag{2.10}
\end{aligned}$$

The expressions for the LPGE currents j_x and j_y under both P - and S -geometries consist of a term that is independent of a and terms that are proportional to $\cos 4a$ and $\sin 4a$. The terms proportional to $\cos 4a$ and $\sin 4a$ switch sign upon changing from P - to S - geometry, as dictated by the replacement of $a \rightarrow a - \pi/4$.

OBLIQUE INCIDENCE WITH P -POLARIZED LIGHT THROUGH A $\lambda/4$ WAVEPLATE

In this experimental geometry, the light incident on the sample is alternately linearly and circularly polarized with polarization $\vec{E} = E_o[\cos \theta (\cos^2 a - i \sin^2 a), (1 + i) \cos a \sin a - (\cos^2 a - i \sin^2 a) \sin \theta]$. The contribution to the photogalvanic current from the first term in (2.6) is given by

$$j_x = 0 \quad (2.11)$$

$$j_y = -\gamma \sin 2a \sin \theta \quad (2.12)$$

Accounting for the second term in (2.6) as well, we derive a total photogalvanic current given by

$$\begin{aligned} j_x &= 1/8\chi_1 \cos 3\varphi + 3/8\chi_1 \cos 2\theta \cos 3\varphi - 3/4\chi_2 \sin 2\theta \\ &+ \cos 4a(3/8\chi_1 \cos 3\varphi + 1/8\chi_1 \cos 2\theta \cos 3\varphi - 1/4\chi_2 \sin 2\theta) \\ &+ \sin 4a(1/2\chi_1 \cos \theta \sin 3\varphi) \end{aligned} \quad (2.13)$$

$$\begin{aligned} j_y &= 1/8\chi_1 \sin 3\varphi + 3/8\chi_1 \cos 2\theta \sin 3\varphi \\ &- \sin 2a(\gamma \sin \theta) \\ &+ \cos 4a(1/4\chi_1 \sin 3\varphi + 1/4 \sin 3\varphi \chi_1 \cos^2 \theta) \\ &- \sin 4a(1/2\chi_1 \cos \theta \cos 3\varphi + 1/2\chi_2 \sin \theta) \end{aligned} \quad (2.14)$$

OBLIQUE INCIDENCE WITH S-POLARIZED LIGHT THROUGH A $\lambda/4$ WAVEPLATE

In this experimental geometry, the light incident on the sample is alternately linearly and circularly polarized with polarization $\vec{E} = E_o[(1 + i) \cos a \sin a \cos \theta, -i \cos^2 a + \sin^2 a, (-1 - i) \cos a \sin a \sin \theta]$. The

contribution to the photogalvanic current from the first term in (2.6) is given by

$$j_x = 0 \quad (2.15)$$

$$j_y = \gamma \sin 2a \sin \theta \quad (2.16)$$

Accounting for the second term in (2.6) as well, we derive a total photogalvanic current given by

$$\begin{aligned} j_x &= -(5/8)\chi_1 \cos 3\varphi + 1/8\chi_1 \cos 2\theta \cos 3\varphi - 1/4\chi_2 \sin 2\theta \\ &\quad - \cos 4a(3/8\chi_1 \cos 3\varphi + 1/8\chi_1 \cos 2\theta \cos 3\varphi - 1/4\chi_2 \sin 2\theta) \\ &\quad - \sin 4a(1/2\chi_1 \cos \theta \sin 3\varphi) \end{aligned} \quad (2.17)$$

$$\begin{aligned} j_y &= -3/4\chi_1 \sin 3\varphi + 1/4 \sin 3\varphi \chi_1 \cos^2 \theta \\ &\quad + \sin 2a(\gamma \sin \theta) \\ &\quad - \cos 4a(1/4\chi_1 \sin 3\varphi + 1/4 \sin 3\varphi \chi_1 \cos^2 \theta) \\ &\quad + \sin 4a(1/2\chi_1 \cos \theta \cos 3\varphi + 1/2\chi_2 \sin \theta) \end{aligned} \quad (2.18)$$

2.3.2 LINEAR AND CIRCULAR PHOTON DRAG EFFECTS IN $\text{Bi}_2\text{Se}_3(111)$

In this section we derive the phenomenological equations governing the linear photon drag effect (LPDE) and circular photon drag effect (CPGE) in $\text{Bi}_2\text{Se}_3(111)$ following the convention in [75]. The fourth rank tensor describing the photon drag effect exhibits the same symmetries as that describing electric field induced second harmonic generation in section 3.1.1.

Because even rank tensors do not necessarily vanish under inversion symmetry, the dominant photon drag contribution comes from the bulk rather than the surface. In general $\Phi_{\lambda\mu\nu\eta}$ has 81 components. Under the transformations by the symmetry operations of D_{3d}^s (without assuming Kleinman symmetry), this is reduced to the following form

$$\Phi = \begin{pmatrix} \Phi_{11}^{(3)} & \Phi_{12}^{(3)} & \Phi_{13}^{(3)} \\ \Phi_{21}^{(3)} & \Phi_{22}^{(3)} & \Phi_{23}^{(3)} \\ \Phi_{31}^{(3)} & \Phi_{32}^{(3)} & \Phi_{33}^{(3)} \end{pmatrix}$$

where each element is a 3×3 matrix given by

$$\Phi_{11}^{(3)} = \begin{pmatrix} \Phi_{xxxx} & 0 & -\Phi_{xyyz} \\ 0 & \Phi_{xxyy} & 0 \\ -\Phi_{xyzy} & 0 & \Phi_{xxzz} \end{pmatrix}$$

$$\Phi_{12}^{(3)} = \begin{pmatrix} & \circ & & \Phi_{xyxy} & \circ \\ \Phi_{xxxx} - \Phi_{xxyy} - \Phi_{xyxy} & & & \circ & \Phi_{xyyz} \\ & \circ & & \Phi_{xyzy} & \circ \end{pmatrix}$$

$$\Phi_{13}^{(3)} = \begin{pmatrix} -\Phi_{xzyy} & \circ & \Phi_{xzxz} \\ \circ & \Phi_{xzyy} & \circ \\ \Phi_{xzxx} & \circ & \circ \end{pmatrix}$$

$$\Phi_{21}^{(3)} = \begin{pmatrix} \circ & \Phi_{xxxx} - \Phi_{xxyy} - \Phi_{xyxy} & \circ \\ \Phi_{xyxy} & & \circ & \Phi_{xyyz} \\ \circ & & \Phi_{xyzy} & \circ \end{pmatrix}$$

$$\Phi_{22}^{(3)} = \begin{pmatrix} \Phi_{xxyy} & \circ & \Phi_{xyyz} \\ \circ & \Phi_{xxxx} & \circ \\ \Phi_{xyzy} & \circ & \Phi_{xxzz} \end{pmatrix}$$

$$\Phi_{23}^{(3)} = \begin{pmatrix} \circ & \Phi_{xzyy} & \circ \\ \Phi_{xzyy} & \circ & \Phi_{xzxz} \\ \circ & \Phi_{xzxx} & \circ \end{pmatrix}$$

$$\Phi_{31}^{(3)} = \begin{pmatrix} -\Phi_{zxyy} & 0 & \Phi_{zxxz} \\ 0 & \Phi_{zxyy} & 0 \\ \Phi_{zzxz} & 0 & 0 \end{pmatrix}$$

$$\Phi_{32}^{(3)} = \begin{pmatrix} 0 & \Phi_{zxyy} & 0 \\ \Phi_{zxyy} & 0 & \Phi_{zxxz} \\ 0 & \Phi_{zzxz} & 0 \end{pmatrix}$$

$$\Phi_{33}^{(3)} = \begin{pmatrix} \Phi_{zzxx} & 0 & 0 \\ 0 & \Phi_{zzxx} & 0 \\ 0 & 0 & \Phi_{zzzz} \end{pmatrix}$$

which contains 14 independent components [76]. In the laboratory coordinate frame, $\Phi^{(3)}$ transforms according to

$$\Phi_{11}^{(3)} \rightarrow \begin{pmatrix} \Phi_{xxxx} & 0 & -\Phi_{xyyz} \cos(3\varphi) \\ 0 & \Phi_{xxyy} & -\Phi_{xyyz} \sin(3\varphi) \\ -\Phi_{xyzy} \cos(3\varphi) & -\Phi_{xyzy} \sin(3\varphi) & \Phi_{xxzz} \end{pmatrix}$$

$$\Phi_{12}^{(3)} \rightarrow \begin{pmatrix} 0 & \Phi_{xyxy} & -\Phi_{xyyz} \sin(3\varphi) \\ \Phi_{xxxx} - \Phi_{xxyy} - \Phi_{xyxy} & 0 & \Phi_{xyyz} \cos(3\varphi) \\ -\Phi_{xyzy} \sin(3\varphi) & \Phi_{xyzy} \cos(3\varphi) & 0 \end{pmatrix}$$

$$\Phi_{13}^{(3)} \rightarrow \begin{pmatrix} -\Phi_{xzyy} \cos(3\varphi) & -\Phi_{xzyy} \sin(3\varphi) & \Phi_{xzzx} \\ -\Phi_{xzyy} \sin(3\varphi) & \Phi_{xzyy} \cos(3\varphi) & 0 \\ \Phi_{xzzx} & 0 & 0 \end{pmatrix}$$

$$\Phi_{21}^{(3)} \rightarrow \begin{pmatrix} 0 & \Phi_{xxxx} - \Phi_{xxyy} - \Phi_{xyxy} & -\Phi_{xyyz} \sin(3\varphi) \\ \Phi_{xyxy} & 0 & \Phi_{xyyz} \cos(3\varphi) \\ -\Phi_{xyzy} \sin(3\varphi) & \Phi_{xyzy} \cos(3\varphi) & 0 \end{pmatrix}$$

$$\Phi_{22}^{(3)} \rightarrow \begin{pmatrix} \Phi_{xxyy} & 0 & \Phi_{xyyz} \cos(3\varphi) \\ 0 & \Phi_{xxxx} & \Phi_{xyyz} \sin(3\varphi) \\ \Phi_{xyzy} \cos(3\varphi) & \Phi_{xyzy} \sin(3\varphi) & \Phi_{xzzx} \end{pmatrix}$$

$$\Phi_{23}^{(3)} \rightarrow \begin{pmatrix} -\Phi_{xzyy} \sin(3\varphi) & \Phi_{xzyy} \cos(3\varphi) & 0 \\ \Phi_{xzyy} \cos(3\varphi) & \Phi_{xzyy} \sin(3\varphi) & \Phi_{xzzx} \\ 0 & \Phi_{xzzx} & 0 \end{pmatrix}$$

$$\Phi_{31}^{(3)} \rightarrow \begin{pmatrix} -\Phi_{zxyy} \cos(3\varphi) & -\Phi_{zxyy} \sin(3\varphi) & \Phi_{zxxz} \\ -\Phi_{zxyy} \sin(3\varphi) & \Phi_{zxyy} \cos(3\varphi) & 0 \\ \Phi_{zxxz} & 0 & 0 \end{pmatrix}$$

$$\Phi_{32}^{(3)} \rightarrow \begin{pmatrix} -\Phi_{zxyy} \sin(3\varphi) & \Phi_{zxyy} \cos(3\varphi) & 0 \\ \Phi_{zxyy} \cos(3\varphi) & \Phi_{zxyy} \sin(3\varphi) & \Phi_{zxxz} \\ 0 & \Phi_{zxxz} & 0 \end{pmatrix}$$

$$\Phi_{33}^{(3)} \rightarrow \begin{pmatrix} \Phi_{zzxx} & 0 & 0 \\ 0 & \Phi_{zzxx} & 0 \\ 0 & 0 & \Phi_{zzzz} \end{pmatrix}$$

Just as we did for the photogalvanic effects, we can decompose the tensor $\Phi_{\lambda\mu\nu\eta}$ into symmetrical and anti-symmetrical parts with respect to inter-change of the indices ν and η . The symmetric part is constructed as follows

$$T_{\lambda\mu\nu\eta} \propto \Phi_{\lambda\mu\nu\eta} + \Phi_{\lambda\mu\eta\nu} \quad (2.19)$$

and the anti-symmetric part as

$$\tilde{T}_{\lambda\mu\xi} \propto e_{\xi\nu\eta} (\Phi_{\lambda\mu\nu\eta} - \Phi_{\lambda\mu\eta\nu}) \quad (2.20)$$

where $e_{\xi\nu\eta}$ is the Levi-Civita tensor and some optical constants have been left out. The photon drag current is then expressed as

$$j_\lambda = T_{\lambda\mu\nu\eta} q_\mu \frac{E_\nu E_\eta^* + E_\nu^* E_\eta}{2} I + \tilde{T}_{\lambda\mu\xi} q_\mu (\hat{P}_{circ})_\xi I \quad (2.21)$$

where $\hat{P}_{circ} = i(\vec{E} \times \vec{E}^*)$ and I is the light intensity. Below we will study the functional form of these currents under the various experimental geometries in detail.

OBLIQUE INCIDENCE WITH P-POLARIZED LIGHT THROUGH A $\lambda/2$ WAVEPLATE

In this experimental geometry, only the first term in (2.21) survives. Assuming that the incident plane of the light is the xz -plane such that $q_y = 0$, this term becomes

$$\begin{aligned}
j_x = & q_x \Phi_{xxyy} + q_z \Phi_{xzyy} \cos 3\varphi \\
& + 1/2(-2 \cos^2 \theta (q_x \Phi_{xxxx} - q_z \Phi_{xzyy} \cos 3\varphi)) \\
& - 2q_x \Phi_{xxzz} \sin^2 \theta + \cos 4\alpha (-q_x \Phi_{xxyy} - q_z \Phi_{xzyy} \cos 3\varphi) \\
& - (-q_z (\Phi_{xzxz} + \Phi_{xzzx}) + q_x (\Phi_{xyyz} + \Phi_{xyzy}) \cos 3\varphi) \sin 2\theta) \\
& + \sin 4\alpha (1/2(2 \cos^2 \theta (q_x \Phi_{xxxx} - q_z \Phi_{xzyy} \cos 3\varphi)) \\
& + 2q_x \Phi_{xxzz} \sin^2 \theta + (-q_z (\Phi_{xzxz} + \Phi_{xzzx}) \\
& + q_x (\Phi_{xyyz} + \Phi_{xyzy}) \cos 3\varphi) \sin 2\theta) \\
& + (-2q_z \Phi_{xzyy} \cos \theta + q_x (\Phi_{xyyz} + \Phi_{xyzy}) \sin \theta) \sin 3\varphi) \quad (2.22)
\end{aligned}$$

$$\begin{aligned}
j_y &= q_z \Phi_{xzzy} \sin 3\varphi - \cos 4\alpha q_z \Phi_{xzzy} \sin 3\varphi \\
&+ 1/2(2q_z \Phi_{xzzy} \cos^2 \theta \sin 3\varphi - q_x(\Phi_{xyyz} + \Phi_{xyzy}) \sin 2\theta \sin 3\varphi) \\
&+ \sin 4\alpha(-\cos \theta(q_x(-\Phi_{xxxx} + \Phi_{xxyy}) - 2q_z \Phi_{xzzy} \cos 3\varphi) \\
&- (q_z(\Phi_{xzxz} + \Phi_{xzzx}) + q_x(\Phi_{xyyz} + \Phi_{xyzy}) \cos 3\varphi) \sin \theta \\
&+ 1/2(-2q_z \Phi_{xzzy} \cos^2 \theta \sin 3\varphi \\
&+ q_x(\Phi_{xyyz} + \Phi_{xyzy}) \sin 2\theta \sin 3\varphi)) \tag{2.23}
\end{aligned}$$

OBLIQUE INCIDENCE WITH S-POLARIZED LIGHT THROUGH A $\lambda/2$ WAVEPLATE

$$\begin{aligned}
j_x &= (q_x \Phi_{xxxx})/2 + q_x \Phi_{xxyy} + (q_x \Phi_{xxzz})/2 + 1/2 q_z \Phi_{xzzy} \cos 3\varphi \\
&+ 1/2 \cos 2\theta(q_x(\Phi_{xxxx} - \Phi_{xxzz}) - q_z \Phi_{xzzy} \cos 3\varphi) \\
&+ 1/2(-q_z(\Phi_{xzxz} + \Phi_{xzzx}) + q_x(\Phi_{xyyz} + \Phi_{xyzy}) \cos 3\varphi) \sin 2\theta \\
&+ \cos 4\alpha(-(1/2)q_x(\Phi_{xxxx} - 2\Phi_{xxyy} + \Phi_{xxzz}) \\
&+ 3/2 q_z \Phi_{xzzy} \cos 3\varphi - 1/2 \cos 2\theta(q_x(\Phi_{xxxx} - \Phi_{xxzz}) \\
&- q_z \Phi_{xzzy} \cos 3\varphi) \\
&+ 1/2(q_z(\Phi_{xzxz} + \Phi_{xzzx}) - q_x(\Phi_{xyyz} + \Phi_{xyzy}) \cos 3\varphi) \sin 2\theta) \\
&+ \sin 4\alpha(2q_z \Phi_{xzzy} \cos \theta \sin 3\varphi - q_x(\Phi_{xyyz} + \Phi_{xyzy}) \sin \theta \sin 3\varphi) \tag{2.24}
\end{aligned}$$

$$\begin{aligned}
j_y = & -q_z \Phi_{xzzy} \sin 3\varphi - q_z \Phi_{xzzy} \cos^2 \theta \sin 3\varphi \\
& + q_x (\Phi_{xyyz} + \Phi_{xyzy}) \cos \theta \sin \theta \sin 3\varphi \\
& + \sin 4\alpha (\cos \theta (-q_x \Phi_{xxxx} + q_x \Phi_{xxyy} - 2q_z \Phi_{xzzy} \cos 3\varphi) \\
& + (q_z (\Phi_{xzxz} + \Phi_{xzzx}) + q_x (\Phi_{xyyz} + \Phi_{xyzy}) \cos 3\varphi) \sin \theta \\
& + q_z \Phi_{xzzy} \sin 3\varphi) + \cos 4\alpha (q_z \Phi_{xzzy} \cos^2 \theta \sin 3\varphi \\
& - q_x (\Phi_{xyyz} + \Phi_{xyzy}) \cos \theta \sin \theta \sin 3\varphi) \quad (2.25)
\end{aligned}$$

OBLIQUE INCIDENCE WITH P-POLARIZED LIGHT THROUGH A $\lambda/4$ WAVEPLATE

$$\begin{aligned}
j_x = & 1/2 (q_x (\Phi_{xxxx} + 6\Phi_{xxyy} + \Phi_{xxzz}) + 5q_z \Phi_{xzzy} \cos 3\varphi \\
& - \cos 2\theta (q_x (-\Phi_{xxxx} + \Phi_{xxzz}) + q_z \Phi_{xzzy} \cos 3\varphi) \\
& - q_z (\Phi_{xzxz} + \Phi_{xzzx}) \sin 2\theta + q_x (\Phi_{xyyz} + \Phi_{xyzy}) \cos 3\varphi \sin 2\theta) \\
& + 1/2 \cos 4\alpha (-q_x (\Phi_{xxxx} - 2\Phi_{xxyy} + \Phi_{xxzz}) \\
& + 3q_z \Phi_{xzzy} \cos 3\varphi + \cos 2\theta (q_x (-\Phi_{xxxx} + \Phi_{xxzz}) \\
& + q_z \Phi_{xzzy} \cos 3\varphi) + (q_z (\Phi_{xzxz} + \Phi_{xzzx}) \\
& - q_x (\Phi_{xyyz} + \Phi_{xyzy}) \cos 3\varphi) \sin 2\theta) \\
& + 1/2 \sin 4\alpha (4q_z \Phi_{xzzy} \cos \theta \sin 3\varphi \\
& - 2q_x (\Phi_{xyyz} + \Phi_{xyzy}) \sin \theta \sin 3\varphi) \quad (2.26)
\end{aligned}$$

$$\begin{aligned}
j_y = & -2 \sin 2\alpha (q_x (2\Phi_{zzxx} + \Phi_{zzzz}) \cos \theta \\
& - q_z (\Phi_{xxxx} + \Phi_{xxyy} + \Phi_{xxzz}) \sin \theta) \\
& + \sin 4\alpha (\cos \theta (q_x (-\Phi_{xxxx} + \Phi_{xxyy}) - 2q_z \Phi_{xzzy} \cos 3\varphi) \\
& + (q_z (\Phi_{xzxx} + \Phi_{xzzx}) + q_x (\Phi_{xyyz} + \Phi_{xyzy}) \cos 3\varphi) \sin \theta) \\
& + 5/2 q_z \Phi_{xzzy} \sin 3\varphi - 1/2 q_z \Phi_{xzzy} \cos 2\theta \sin 3\varphi \\
& + 1/2 q_x (\Phi_{xyyz} + \Phi_{xyzy}) \sin 2\theta \sin 3\varphi \\
& + \cos 4\alpha (3/2 q_z \Phi_{xzzy} \sin 3\varphi + 1/2 q_z \Phi_{xzzy} \cos 2\theta \sin 3\varphi \\
& - 1/2 q_x (\Phi_{xyyz} + \Phi_{xyzy}) \sin 2\theta \sin 3\varphi) \quad (2.27)
\end{aligned}$$

OBLIQUE INCIDENCE WITH S-POLARIZED LIGHT THROUGH A $\lambda/4$ WAVEPLATE

$$\begin{aligned}
j_x = & 1/2 (q_x (\Phi_{xxxx} + 6\Phi_{xxyy} + \Phi_{xxzz}) + 5q_z \Phi_{xzzy} \cos 3\varphi \\
& - \cos 2\theta (q_x (-\Phi_{xxxx} + \Phi_{xxzz}) + q_z \Phi_{xzzy} \cos 3\varphi) \\
& - q_z (\Phi_{xzxx} + \Phi_{xzzx}) \sin 2\theta + q_x (\Phi_{xyyz} + \Phi_{xyzy}) \cos 3\varphi \sin 2\theta) \\
& + 1/2 \cos 4\alpha (-q_x (\Phi_{xxxx} - 2\Phi_{xxyy} + \Phi_{xxzz}) \\
& + 3q_z \Phi_{xzzy} \cos 3\varphi + \cos 2\theta (q_x (-\Phi_{xxxx} + \Phi_{xxzz}) \\
& + q_z \Phi_{xzzy} \cos 3\varphi) + (q_z (\Phi_{xzxx} + \Phi_{xzzx}) \\
& - q_x (\Phi_{xyyz} + \Phi_{xyzy}) \cos 3\varphi) \sin 2\theta) \\
& + 1/2 \sin 4\alpha (4q_z \Phi_{xzzy} \cos \theta \sin 3\varphi \\
& - 2q_x (\Phi_{xyyz} + \Phi_{xyzy}) \sin \theta \sin 3\varphi) \quad (2.28)
\end{aligned}$$

$$\begin{aligned}
j_y = & 2 \sin 2\alpha (q_x (2\Phi_{zzxx} + \Phi_{zzzz}) \cos \theta \\
& - q_z (\Phi_{xxxx} + \Phi_{xxyy} + \Phi_{xxzz}) \sin \theta) \\
& + \sin 4\alpha (\cos \theta (q_x (-\Phi_{xxxx} + \Phi_{xxyy}) - 2q_z \Phi_{xzyy} \cos 3\varphi) \\
& + (q_z (\Phi_{xzxx} + \Phi_{xzzx}) + q_x (\Phi_{xyyz} + \Phi_{xyzy}) \cos 3\varphi) \sin \theta) \\
& + 5/2 q_z \Phi_{xzyy} \sin 3\varphi - 1/2 q_z \Phi_{xzyy} \cos 2\theta \sin 3\varphi \\
& + 1/2 q_x (\Phi_{xyyz} + \Phi_{xyzy}) \sin 2\theta \sin 3\varphi \\
& + \cos 4\alpha (3/2 q_z \Phi_{xzyy} \sin 3\varphi + 1/2 q_z \Phi_{xzyy} \cos 2\theta \sin 3\varphi \\
& - 1/2 q_x (\Phi_{xyyz} + \Phi_{xyzy}) \sin 2\theta \sin 3\varphi) \quad (2.29)
\end{aligned}$$

This page is intentionally left blank

3

Second harmonic generation from the surface of a topological insulator

THE ELECTRICAL RESPONSE PROPERTIES of topological insulator surfaces are predicted to be highly novel, including protection against back-scattering from non-magnetic impurities [24, 28] and a switchable spin-polarized electrical current [48, 49]. Under certain experimental conditions, the surface states are predicted to evolve into new broken symmetry electronic phases that exhibit topological superconductivity [28] and an anomalous half-integer quantum Hall effect [28, 30], which have

been proposed as media to search for Majorana fermions [24, 28] and charge fractionalization in three-dimensions [77]. Owing to these exciting theoretical proposals, the recent discovery of three-dimensional topological insulator phases in $\text{Bi}_{1-x}\text{Sb}_x$ [36, 43], Bi_2Se_3 [37, 38] and related materials [38, 78, 79] has generated great interest to measure their symmetry and electrical properties at an isolated surface. However, a major experimental obstacle has been the high density of mobile electrons in the bulk of these materials, which can overwhelm the surface electrical responses. Although transport results on electrically gated samples show evidence for surface carrier modulation [42, 80, 81], the contributions to the electrical response from carriers on different surfaces and in the bulk are difficult to separate and require highly insulating samples, which are difficult to produce. Moreover, contacts and gates deposited on the surface may perturb the intrinsic surface electronic structure [70]. Optical probes have been proposed as a contact free alternative that can be focused onto a single surface [30, 34, 48, 82]. However, most experiments to date have been limited to the linear optical regime, which has been shown to be dominated by the bulk electronic response [83–85] except in the limit of very thin samples [86, 87].

In this chapter, we demonstrate that the nonlinear second harmonic generation (SHG) of light from bulk single crystals of Bi_2Se_3 is highly sensitive to electrons confined to the surface and accumulation region [73, 74, 88]. The underlying principle for this surface sensitivity is that SHG is predominantly generated where inversion symmetry is broken

[89], which only occurs at the surface of the bulk inversion-symmetric Bi_2Se_3 . In section 3.1, we develop a theoretical model that describes the SHG intensity from Bi_2Se_3 in terms of the second- and third-order nonlinear electric susceptibilities. By performing a symmetry analysis of Bi_2Se_3 we identify the susceptibility tensor elements that contribute to SHG and show that their relative magnitudes can be determined by measuring the intensity and polarization of the emitted SHG as a function of crystal orientation and incident laser polarization. In section 3.2, we perform SHG experiments on bulk single crystals of Bi_2Se_3 and find that the results are described well by our model. To prove that second harmonic generation is sensitive to the surface, we perform a surface doping dependent study that reveals that changes in the surface Fermi level can be monitored optically. We also show that generating second harmonic with circular polarized light is a sensitive measure of the time-reversal symmetry properties of the system and is robust against surface charging, which makes second harmonic generation a promising tool for spectroscopic studies of topological surfaces. In section 3.3 we provide a summary and outlook.

3.1 THEORETICAL BACKGROUND

This section is organized into two parts. In section 3.1.1, we determine the susceptibility tensor elements that give rise to SHG in Bi_2Se_3 by per-

forming a crystal symmetry analysis. In section 3.1.2, we present a phenomenological model that describes the intensity of second harmonic light generated from Bi_2Se_3 using these tensor elements.

3.1.1 SYMMETRY ANALYSIS AND ELECTRIC SUSCEPTIBILITY TENSORS OF $\text{Bi}_2\text{Se}_3(111)$

The electrical response of a material is described by susceptibility tensors $\chi^{(n)}$ that relate the electric polarization of the material \vec{P} to the applied electric field \vec{E} through the power-series expansion [89]

$$P_i = \chi_{ij}^{(1)} E_j + \chi_{ijk}^{(2)} E_j E_k + \chi_{ijkl}^{(3)} E_j E_k E_l + \dots \quad (3.1)$$

in the electric dipole approximation, where the indices run through spatial coordinates. The susceptibility tensor elements of each $\chi^{(n)}$ can be determined by performing a crystal symmetry analysis. The bulk crystal structure of $\text{Bi}_2\text{Se}_3(111)$, which belongs to space group D_{3d}^5 , remains invariant under a group of symmetry operations T . These consist of (i) rotation along the (111) axis by 0° , 120° and 240° , (ii) mirror reflection under planes a , b and c [Figure 3.1.1], and (iii) inversion symmetry. Because $\chi^{(n)}$ must obey the same symmetry conditions as the crystal, they must be invariant under the same group of symmetry operations that

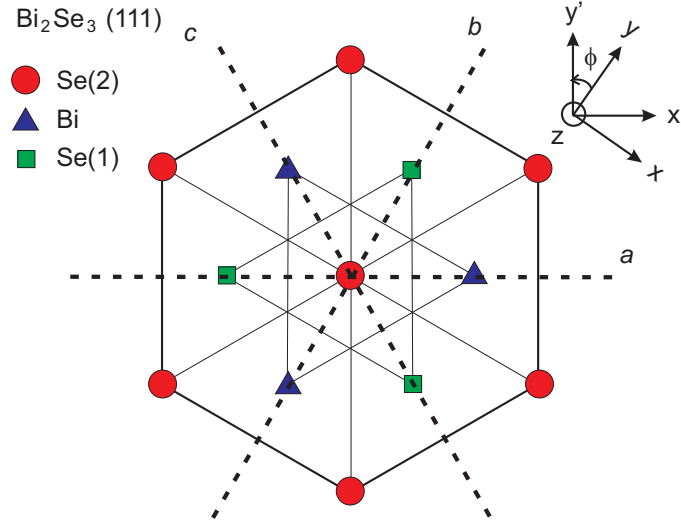


Figure 3.1.1: C_{3v} symmetry of the $\text{Bi}_2\text{Se}_3(111)$ cleaved surface. The three-fold rotation symmetry and the three planes of mirror symmetry (a , b and c) are illustrated. The bulk D_{3d}^5 symmetry is given by the addition of inversion symmetry out of the page. The topmost, second and third atomic layers are Se(2), Bi and Se(1) respectively. The relationship between the crystal (primed) and beam (un-primed) coordinates are shown in the top right. Figure reprinted from [74].

bring $\chi^{(n)}$ to $\chi^{(n)'}$, which is given by [89]

$$\chi_{i_1 i_2 \dots i_{n+1}}^{(n)'} = \sum_{j_1 j_2 \dots j_{n+1}} T_{i_1 j_1} T_{i_2 j_2} \dots T_{i_{n+1} j_{n+1}} \chi_{j_1 j_2 \dots j_{n+1}}^{(n)} \quad (3.2)$$

Under such transformations, the crystal symmetry greatly reduces the number of non-zero independent components of $\chi^{(n)}$.

We first examine the first-order response characterized by $\chi^{(1)}$ in (3.1). Because $\chi^{(1)}$ is an even rank tensor and P_i and E_j are both odd under the operation of inversion, a first-order response is permitted regard-

less of whether or not crystal inversion symmetry is present. Therefore, the linear electronic response can include contributions from both the inversion symmetric bulk of Bi_2Se_3 as well as from the (111) surface where inversion symmetry is necessarily broken [89]. The individual tensor elements can be found by transforming $\chi^{(1)}$ under the rotation, mirror and inversion symmetry operations that characterize bulk Bi_2Se_3 via (3.2) and equating the resulting tensors. Using this procedure, we find that $\chi^{(1)}$ assumes the form

$$\chi^{(1)} = \begin{pmatrix} \chi_{11}^{(1)} & 0 & 0 \\ 0 & \chi_{22}^{(1)} & 0 \\ 0 & 0 & \chi_{33}^{(1)} \end{pmatrix} \quad (3.3)$$

where $\chi_{11}^{(1)} = \chi_{22}^{(1)}$, and $\chi_{33}^{(1)}$ are scalars [76]. This mandates an isotropic first-order electronic response in the (111) plane. Aspects of this response have been measured by conventional transport and linear optical studies where the bulk contribution has been shown to dominate.

We now analyze how the $\text{Bi}_2\text{Se}_3(111)$ crystal symmetry affects the second-order dipolar response $\chi^{(2)}$. From (3.2) we see that all of the components of odd rank tensors must vanish under the inversion operator $T_{ij} = -\delta_{ij}$ because each component is mapped to the negative of itself. Therefore, all 27 components of $\chi^{(2)}$ must be zero in the inversion symmetric bulk of Bi_2Se_3 . However, at the cleaved (111) surface inversion symmetry is broken and the crystal symmetry is reduced to

C_{3v} symmetry. In the case of Bi_2Se_3 , cleavage occurs naturally between two Se layers that are van der Waals bonded to expose large optically flat areas that are Se terminated [24, 28, 29]. Owing to this lack of inversion symmetry, non-vanishing components of odd rank tensors such as $\chi^{(2)}$ are permitted to exist. Similar to the procedure used to find the $\chi^{(1)}$ components, the $\chi^{(2)}$ tensor elements can be found by transforming $\chi^{(2)}$ under the C_{3v} rotation and mirror symmetry operations [Figure 3.1.1] via (3.2) and equating the resulting tensors. We find that $\chi^{(2)}$ assumes the form

$$\chi^{(2)} = \begin{pmatrix} \begin{pmatrix} \chi_{xxx} \\ \circ \\ \chi_{xxz} \end{pmatrix} & \begin{pmatrix} \circ \\ -\chi_{xxx} \\ \circ \end{pmatrix} & \begin{pmatrix} \chi_{xxz} \\ \circ \\ \circ \end{pmatrix} \\ \begin{pmatrix} \circ \\ -\chi_{xxx} \\ \circ \end{pmatrix} & \begin{pmatrix} -\chi_{xxx} \\ \circ \\ \chi_{xxz} \end{pmatrix} & \begin{pmatrix} \circ \\ \chi_{xxz} \\ \circ \end{pmatrix} \\ \begin{pmatrix} \chi_{zxx} \\ \circ \\ \circ \end{pmatrix} & \begin{pmatrix} \circ \\ \chi_{zxx} \\ \circ \end{pmatrix} & \begin{pmatrix} \circ \\ \circ \\ \chi_{zzz} \end{pmatrix} \end{pmatrix}$$

which contains four non-zero independent components: χ_{xxx} ($= -\chi_{xyy}$
 $= -\chi_{yxy}$), χ_{zxx} ($= \chi_{zyy}$), χ_{xxz} ($= \chi_{yyz}$), and χ_{zzz} , and x , y and z refer to

the crystal coordinates defined in Figure 3.1.1. $\chi^{(2)}$ can be transformed from the sample coordinate frame into the laboratory coordinate frame using (3.2) with T substituted by the rotation matrix [89]

$$R(\varphi) = \begin{pmatrix} \cos(\varphi) & -\sin(\varphi) & 0 \\ \sin(\varphi) & \cos(\varphi) & 0 \\ 0 & 0 & 1 \end{pmatrix}$$

This yields

$$\chi^{(2)} \rightarrow \begin{pmatrix} \begin{pmatrix} \chi_{xxx} \cos(3\varphi) \\ -\chi_{xxx} \sin(3\varphi) \\ \chi_{xxz} \end{pmatrix} & \begin{pmatrix} -\chi_{xxx} \sin(3\varphi) \\ -\chi_{xxx} \cos(3\varphi) \\ 0 \end{pmatrix} & \begin{pmatrix} \chi_{xxz} \\ 0 \\ 0 \end{pmatrix} \\ \begin{pmatrix} -\chi_{xxx} \sin(3\varphi) \\ -\chi_{xxx} \cos(3\varphi) \\ 0 \end{pmatrix} & \begin{pmatrix} -\chi_{xxx} \cos(3\varphi) \\ \chi_{xxx} \sin(3\varphi) \\ \chi_{xxz} \end{pmatrix} & \begin{pmatrix} 0 \\ \chi_{xxz} \\ 0 \end{pmatrix} \\ \begin{pmatrix} \chi_{zxx} \\ 0 \\ 0 \end{pmatrix} & \begin{pmatrix} \chi_{xxz} \\ 0 \\ \chi_{zxx} \\ 0 \end{pmatrix} & \begin{pmatrix} 0 \\ 0 \\ 0 \\ \chi_{zzz} \end{pmatrix} \end{pmatrix}$$

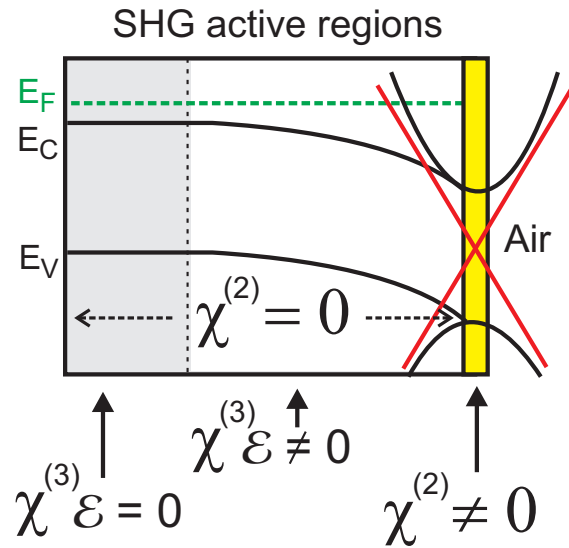


Figure 3.1.2: SHG active regions. SHG active regions where $\chi^{(2)} + \chi^{(3)}\mathcal{E} \neq 0$, which represent the surface (yellow) and accumulation region (white) contributions respectively. Figure reprinted from [74].

In section 3.2 we show how these tensor elements are manifested in the SHG intensity as a function of the crystal orientation and the incident light polarization.

In addition to the surface $\chi^{(2)}$ contribution derived above, SHG can be generated by accumulation layer electrons. These are bulk electrons confined near the surface by a band-bending induced electric field $\vec{\mathcal{E}}$ directed perpendicular to the surface. SHG is highly sensitive to a static electric field because it acts to break inversion symmetry over the accumulation region [Figure 3.1.2]. Electric-field induced SHG is commonly observed in the context of metal-electrolyte interfaces [90] and is theoretically described by a third-order process

$$P_i(2\omega) = \chi_{ipqr}^{(3)} \mathcal{E}_p(\omega) E_q(\omega) E_r(\omega)$$

that acts in addition to $\chi^{(2)}$ [89–91]. Because $\chi^{(3)}$ has the same symmetry constraints as $\chi^{(2)}$, the overall symmetry of the SHG intensity as a function of the crystal orientation must remain unchanged in the presence of $\vec{\mathcal{E}}$, as will be shown below, with each $\chi^{(2)}$ tensor element simply being enhanced by the addition of a $\chi^{(3)} \vec{\mathcal{E}}$ tensor element.

We now impose the same symmetry conditions on $\chi^{(3)}$ as was done above for $\chi^{(2)}$. Unlike odd rank tensors, all components of even rank tensors do not necessarily vanish under inversion symmetry. Therefore, the dominant $\chi^{(3)}$ contribution to SHG will be from the bulk rather than the surface. However, SHG will only be generated by $\chi^{(3)}$ over the finite accumulation region that the band-bending field $\vec{\mathcal{E}}$ penetrates into the bulk. In general $\chi^{(3)}$ has 81 components. Under the transformations by the symmetry operations of D_{3d}^5 , this is reduced to the following form

$$\chi^{(3)} = \begin{pmatrix} \chi_{11}^{(3)} & \chi_{12}^{(3)} & \chi_{13}^{(3)} \\ \chi_{21}^{(3)} & \chi_{22}^{(3)} & \chi_{23}^{(3)} \\ \chi_{31}^{(3)} & \chi_{32}^{(3)} & \chi_{33}^{(3)} \end{pmatrix}$$

where

$$\chi_{11}^{(3)} = \begin{pmatrix} \chi_{xxxx} & 0 & -\chi_{xyyz} \\ 0 & \chi_{xxyy} & 0 \\ -\chi_{xyzy} & 0 & \chi_{xxzz} \end{pmatrix}$$

$$\chi_{12}^{(3)} = \begin{pmatrix} 0 & \chi_{xyxy} & 0 \\ \chi_{xxxx} - \chi_{xxyy} - \chi_{xyxy} & 0 & \chi_{xyyz} \\ 0 & \chi_{xyzy} & 0 \end{pmatrix}$$

$$\chi_{13}^{(3)} = \begin{pmatrix} -\chi_{xzyy} & 0 & \chi_{xzzz} \\ 0 & \chi_{xzzy} & 0 \\ \chi_{xzzx} & 0 & 0 \end{pmatrix}$$

$$\chi_{21}^{(3)} = \begin{pmatrix} 0 & \chi_{xxxx} - \chi_{xxyy} - \chi_{xyxy} & 0 \\ \chi_{xyxy} & 0 & \chi_{xyyz} \\ 0 & \chi_{xyzy} & 0 \end{pmatrix}$$

$$\chi_{22}^{(3)} = \begin{pmatrix} \chi_{xxyy} & 0 & \chi_{xyyz} \\ 0 & \chi_{xxxx} & 0 \\ \chi_{xyzy} & 0 & \chi_{xxzz} \end{pmatrix}$$

$$\chi_{23}^{(3)} = \begin{pmatrix} 0 & \chi_{xzyy} & 0 \\ \chi_{xzzy} & 0 & \chi_{xzzz} \\ 0 & \chi_{xzzx} & 0 \end{pmatrix}$$

$$\chi_{31}^{(3)} = \begin{pmatrix} -\chi_{zxyy} & 0 & \chi_{zxxx} \\ 0 & \chi_{zxyy} & 0 \\ \chi_{zxzx} & 0 & 0 \end{pmatrix}$$

$$\chi_{32}^{(3)} = \begin{pmatrix} 0 & \chi_{zxyy} & 0 \\ \chi_{zxyy} & 0 & \chi_{zxxx} \\ 0 & \chi_{zxzx} & 0 \end{pmatrix}$$

$$\chi_{33}^{(3)} = \begin{pmatrix} \chi_{zzxx} & 0 & 0 \\ 0 & \chi_{zzxx} & 0 \\ 0 & 0 & \chi_{zzzz} \end{pmatrix}$$

which contains 17 independent components [92]. In the laboratory coordinate frame, $\chi^{(3)}$ transforms according to

$$\chi_{11}^{(3)} \rightarrow \begin{pmatrix} \chi_{xxxx} & 0 & -\chi_{xyyz} \cos(3\varphi) \\ 0 & \chi_{xxyy} & -\chi_{xyyz} \sin(3\varphi) \\ -\chi_{xyzy} \cos(3\varphi) & -\chi_{xyzy} \sin(3\varphi) & \chi_{xxzz} \end{pmatrix}$$

$$\chi_{12}^{(3)} \rightarrow \begin{pmatrix} 0 & \chi_{xyxy} & -\chi_{xyyz} \sin(3\varphi) \\ \chi_{xxxx} - \chi_{xxyy} - \chi_{xyxy} & 0 & \chi_{xyyz} \cos(3\varphi) \\ -\chi_{xyzy} \sin(3\varphi) & \chi_{xyzy} \cos(3\varphi) & 0 \end{pmatrix}$$

$$\chi_{13}^{(3)} \rightarrow \begin{pmatrix} -\chi_{xzyy} \cos(3\varphi) & -\chi_{xzyy} \sin(3\varphi) & \chi_{xzxx} \\ -\chi_{xzyy} \sin(3\varphi) & \chi_{xzyy} \cos(3\varphi) & 0 \\ \chi_{xzxx} & 0 & 0 \end{pmatrix}$$

$$\chi_{21}^{(3)} \rightarrow \begin{pmatrix} 0 & \chi_{xxxx} - \chi_{xxyy} - \chi_{xyxy} & -\chi_{xyyz} \sin(3\varphi) \\ \chi_{xyxy} & 0 & \chi_{xyyz} \cos(3\varphi) \\ -\chi_{xyzy} \sin(3\varphi) & \chi_{xyzy} \cos(3\varphi) & 0 \end{pmatrix}$$

$$\chi_{22}^{(3)} \rightarrow \begin{pmatrix} \chi_{xxyy} & 0 & \chi_{xyyz} \cos(3\varphi) \\ 0 & \chi_{xxxx} & \chi_{xyyz} \sin(3\varphi) \\ \chi_{xyzy} \cos(3\varphi) & \chi_{xyzy} \sin(3\varphi) & \chi_{xxzz} \end{pmatrix}$$

$$\chi_{23}^{(3)} \rightarrow \begin{pmatrix} -\chi_{xzyy} \sin(3\varphi) & \chi_{xzyy} \cos(3\varphi) & 0 \\ \chi_{xzyy} \cos(3\varphi) & \chi_{xzyy} \sin(3\varphi) & \chi_{xzxx} \\ 0 & \chi_{xzxx} & 0 \end{pmatrix}$$

$$\chi_{31}^{(3)} \rightarrow \begin{pmatrix} -\chi_{zxyy} \cos(3\varphi) & -\chi_{zxyy} \sin(3\varphi) & \chi_{zxxx} \\ -\chi_{zxyy} \sin(3\varphi) & \chi_{zxyy} \cos(3\varphi) & 0 \\ \chi_{zxxz} & 0 & 0 \end{pmatrix}$$

$$\chi_{32}^{(3)} \rightarrow \begin{pmatrix} -\chi_{zxyy} \sin(3\varphi) & \chi_{zxyy} \cos(3\varphi) & 0 \\ \chi_{zxyy} \cos(3\varphi) & \chi_{zxyy} \sin(3\varphi) & \chi_{zxxx} \\ 0 & \chi_{zxxx} & 0 \end{pmatrix}$$

$$\chi_{33}^{(3)} \rightarrow \begin{pmatrix} \chi_{zzxx} & 0 & 0 \\ 0 & \chi_{zzxx} & 0 \\ 0 & 0 & \chi_{zzzz} \end{pmatrix}$$

We note that there may also be higher multipole bulk contributions to SHG that can be finite even in inversion symmetric systems [89] and that will have the same symmetry properties as both the surface $\chi^{(2)}$ and $\chi^{(3)}$ tensors [76] shown above. The bulk electric quadrupole and magnetic dipole contributions are the dominant of these higher multipole susceptibilities, however they are generally suppressed relative to the dipolar susceptibilities by a factor of ka , where k is the wavevector of the incident light and a is a lattice constant [89]. In reflection measurements, the bulk contribution only comes from a layer within the optical penetration depth (ξ) of the incident light, which we measure to be ~ 25 nm at 795 nm [section 3.2.1]. The surface contribution will come from the entire depth d over which the surface wavefunctions penetrate into the bulk, which is of the order $d \equiv \hbar v_f / \Delta \sim 10$ Å for states within the bulk-gap, and is much larger for states not in the bulk gap, where v_f is the Fermi velocity, \hbar is the reduced Planck's constant, and Δ is the bulk band gap energy. Therefore, the relative intensity of the surface to bulk second harmonic radiation is approximately $|\frac{1}{ka} \frac{d}{\xi}|^2 = |\frac{7.95 \times 10^3 \text{Å}}{2\pi \times 2\text{Å}} \frac{10\text{Å}}{2.5 \times 10^2 \text{Å}}|^2 \sim 640$. Indeed, measurements on other strong spin-orbit coupled materials, such as Au, in the regime where interband transitions dominate ($\Delta < \hbar\omega$) have shown that these bulk

contributions are greatly suppressed [93]. Bulk contributions have only been shown to be observable when $\Delta > \hbar\omega$, where the penetration depth of the light into the crystal is very deep [94]. All of our measurements were performed in the regime $\Delta < \hbar\omega$ and we experimentally demonstrate in section 3.2.4 by varying the surface carrier density that these higher order bulk effects are indeed not dominant.

3.1.2 PHENOMENOLOGICAL MODEL OF SURFACE SHG

In this section, we show how the intensity of second harmonic radiation is related to the nonlinear susceptibility tensors derived in section 3.1.1. Our phenomenological model of surface SHG follows the convention developed by Mizrahi and Sipe (1988) [95], which builds on the earlier work of Heinz (1982) [96] and Bloembergen & Pershan (1962) [97]. The model assumes that a thin dipole sheet confined to the surface is the source of surface second harmonic generation. Following the notation used in [95] for surface SHG from a thick crystal in the reflection geometry, the second harmonic intensity $I(2\omega)$ is given by

$$I(2\omega) = A \times |\hat{e}_i(2\omega)(\chi_s)_{ijk}\hat{e}_j(\omega)\hat{e}_k(\omega)|^2 I(\omega)^2 \quad (3.4)$$

where A is a geometrical constant, \hat{e} is the beam polarization of the incoming or outgoing radiation field inside the crystal, $I(\omega)$ is the intensity of the incident beam, χ_s is the complex surface nonlinear susceptibility tensor and the indices run through x , y and z . The unit polariza-

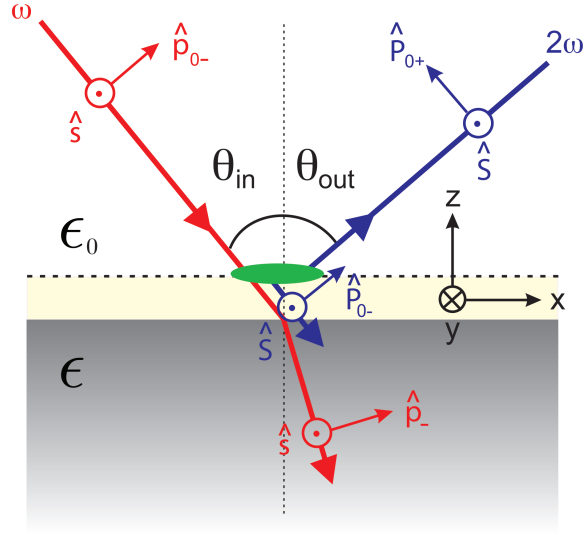


Figure 3.1.3: SHG laser beam geometry and polarizations. Schematic of the incoming and outgoing laser beam geometry and polarizations. The polarization vectors of the fundamental and second harmonic beams are labeled by lower case and upper case letters respectively. The cream colored region at $z = 0$ denotes the nonlinear polarization sheet at the surface as described in [95]. The interaction volume of the beams is demarcated by the green shaded region. The beams are displaced horizontally for visual clarity. Figure reprinted from [74].

tion vectors are given by

$$\hat{\mathbf{e}}(\omega) = \frac{E_{in}^s}{|E_{in}|} t_{om}^s \hat{\mathbf{S}} + \frac{E_{in}^p}{|E_{in}|} t_{om}^p \hat{\mathbf{P}}_-$$

$$\hat{\mathbf{e}}(2\omega) = \frac{E_{out}^s}{|E_{out}|} (1 + R_{om}^s) \hat{\mathbf{S}} + \frac{E_{out}^p}{|E_{out}|} (\hat{\mathbf{P}}_{o+} + R_{om}^p \hat{\mathbf{P}}_{o-}) \quad (3.5)$$

where $|E_{in}|$ and $|E_{out}|$ denote the magnitude of the input fundamental and output second harmonic electric fields respectively, $t_{om}^{s,p}$ is the Fresnel coefficient for transmission of the fundamental beam from air into the medium with dielectric constant ϵ , $R_{om}^{s,p}$ is the Fresnel coefficient for reflection of the second harmonic beam off of the medium [95], and all polarization directions are defined in Figure 3.1.3.

Our experiments are performed at $\theta_{in} = \theta_{out} = 45^\circ$ and we assume $\epsilon(\omega) = \epsilon(2\omega) = 29$. The latter assumption is based on our measurements of the index of refraction in section 3.2.1. We also let $\vec{\mathcal{E}}$ lie along the z direction, which is reasonable because the atomic layers must be equipotentials. Using these parameters in (3.4) and (3.5), we obtain expressions for the intensity of second harmonic radiation as a function of the in-plane crystal orientation angle φ [Figure 3.1.1] under different linear polarization geometries and circular polarization geometries as follows:

$$\begin{aligned}
I_{PP}(2\omega) &= A |c^{(3)} - 0.025 c^{(1)} \cos(3\varphi)|^2 \\
I_{SP}(2\omega) &= A |c^{(2)} + 0.016 c^{(1)} \cos(3\varphi)|^2 \\
I_{PS}(2\omega) &= A |0.020 c^{(1)} \sin(3\varphi)|^2 \\
I_{SS}(2\omega) &= A |0.013 c^{(1)} \sin(3\varphi)|^2
\end{aligned} \tag{3.6}$$

and

$$\begin{aligned}
I_{RS}(2\omega) &= \frac{A}{4} |c^{(4)} - 0.032i c^{(1)} \cos(3\varphi)|^2 \\
&\quad - 0.033 c^{(1)} \sin(3\varphi)|^2 \\
I_{LS}(2\omega) &= \frac{A}{4} |c^{(4)} - 0.032i c^{(1)} \cos(3\varphi)|^2 \\
&\quad + 0.033 c^{(1)} \sin(3\varphi)|^2 \\
I_{RP}(2\omega) &= \frac{A}{4} |c^{(5)} + 0.041 c^{(1)} \cos(3\varphi)|^2 \\
&\quad - 0.040 c^{(1)} \sin(3\varphi)|^2 \\
I_{LP}(2\omega) &= \frac{A}{4} |c^{(5)} + 0.041 c^{(1)} \cos(3\varphi)|^2 \\
&\quad + 0.040 c^{(1)} \sin(3\varphi)|^2 \tag{3.7}
\end{aligned}$$

The circular dichroism expressions, defined as $CD_S \equiv I_{RS} - I_{LS}$ and $CD_P \equiv I_{RP} - I_{LP}$, become

$$\begin{aligned}
CD_S &= -0.033 \frac{A}{2} [(c^{(1)})^\dagger \times c^{(4)} \\
&\quad + c^{(1)} \times (c^{(4)})^\dagger] \sin(3\varphi) \\
CD_P &= -0.040i \frac{A}{2} [c^{(1)} \times (c^{(5)})^\dagger \\
&\quad - (c^{(1)})^\dagger \times c^{(5)}] \sin(3\varphi) \tag{3.8}
\end{aligned}$$

In the above equations, $c^{(n)} = a^{(n)} + b^{(n)}$ where

$$\begin{aligned}
a^{(1)} &= \chi_{xxx} \\
a^{(2)} &= 0.061 \chi_{zxx} \\
a^{(3)} &= -0.007 \chi_{xxz} + 0.096 \chi_{zxx} + 0.002 \chi_{zzz} \\
a^{(4)} &= 0.004i \chi_{xxz} \\
a^{(5)} &= 0.007 \chi_{xxz} - 0.034 \chi_{zxx} - 0.002 \chi_{zzz} \quad (3.9)
\end{aligned}$$

represent the surface $\chi^{(2)}$ SHG and

$$\begin{aligned}
b^{(1)} &= -\chi_{xyyz} \mathcal{E}_z \\
b^{(2)} &= 0.061 \chi_{zxxx} \mathcal{E}_z \\
b^{(3)} &= (0.003 \chi_{xxzz} - 0.003 \chi_{xzxx} + 0.096 \chi_{zxxz} \\
&\quad + 0.002 \chi_{zzzz}) \mathcal{E}_z \\
b^{(4)} &= (0.002i \chi_{xxzz} + 0.002i \chi_{xzxx}) \mathcal{E}_z \\
b^{(5)} &= (0.003 \chi_{xxzz} + 0.003 \chi_{xzxx} - 0.034 \chi_{zxxz} \\
&\quad - 0.002 \chi_{zzzz}) \mathcal{E}_z \quad (3.10)
\end{aligned}$$

represent the electric field-induced SHG over the accumulation region due to $\chi^{(3)} \vec{\mathcal{E}}$. The magnitudes of $c^{(n)}$ can be experimentally determined by measuring $I(2\omega)$ as a function of the in-plane crystal orientation angle φ and laser polarization. The relative contributions of $a^{(n)}$ and $b^{(n)}$ can then be determined by varying the surface carrier density. The re-

sults are shown in section 3.2.4.

3.2 EXPERIMENTAL RESULTS

This section is organized as follows. In section 3.2.1 we overview the Bi_2Se_3 sample growth procedures, sample characterization results, and the experimental apparatus used to measure second harmonic generation from material surfaces. In section 3.2.2 we study the first order linear optical response of Bi_2Se_3 . In section 3.2.3 we characterize the second order nonlinear optical response and study the effects of surface molecular doping on the SHG in section 3.2.4. We conclude by investigating circular dichroism SHG in section 3.2.5.

3.2.1 METHODS AND SAMPLE CHARACTERIZATION

In this work, samples of Bi_2Se_3 were lightly hole-doped by substituting As into the Se planes to reduce the bulk carrier concentration [42, 45], although they remain electrically conducting. Single crystal $\text{Bi}_{2-x}\text{As}_x\text{Se}_3$ was grown by melting a 10 g stoichiometric mixture of Bi and Se shot with trace amounts of As powder ($x=0.00129$) in an evacuated quartz tube at 850°C . After 12 hours at this temperature, the mixture was cooled to 720°C over two hours, then slowly cooled to 650°C over two days. The batch was annealed at 650°C for two more days then furnace cooled

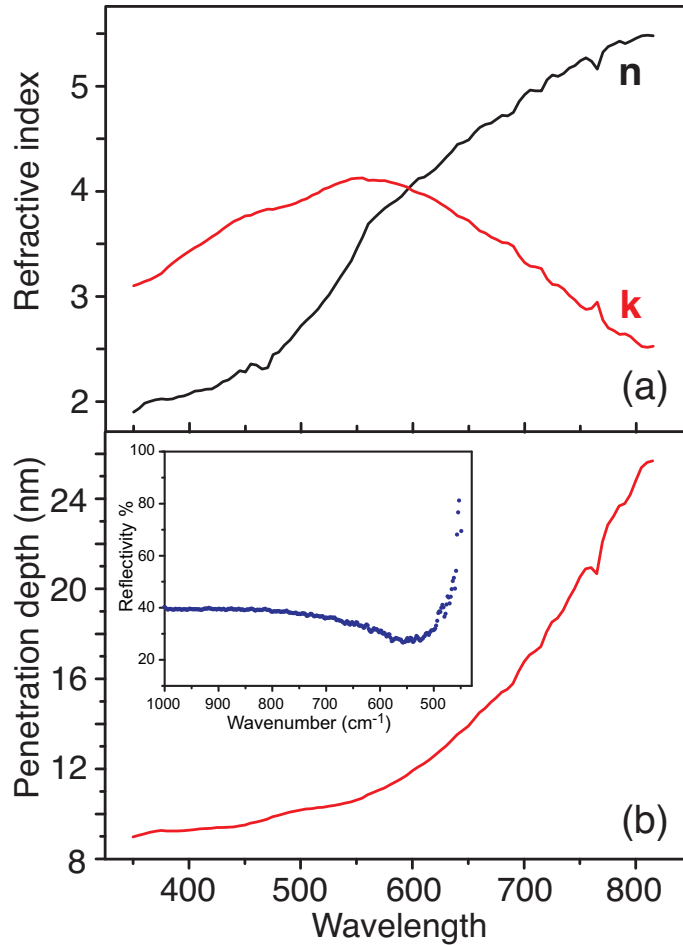


Figure 3.2.1: Bi₂Se₃ refractive index and penetration depth. (a) Real (n) and imaginary (k) parts of the Bi₂Se₃ index of refraction as a function of light wavelength acquired by performing spectroscopic ellipsometry measurements. (b) Optical penetration depth as a function of wavelength. Inset: Measured FTIR reflectivity as a function of wavenumber normalized to the reflectivity of gold. The reflectivity minimum at wavenumber $k \sim 557 \text{ cm}^{-3}$ ($f_p = 1.67 \times 10^{13} \text{ Hz}$) is due to absorption at the plasmon resonance, from which we calculate an electron density of $n_e = 4.33 \times 10^{17} \text{ cm}^{-3}$. Figure reprinted from [74].

to room temperature.

After growth, the crystal orientation was determined by X-ray diffraction using a Bruker D8 diffractometer with Cu K α radiation ($\lambda = 1.54\text{\AA}$) and a two-dimensional area detector. The real (n) and imaginary (k) parts of the index of refraction were determined between 350 nm and 820 nm by performing spectroscopic ellipsometry measurements using a Sopra GES 5 Spectroscopic Ellipsometer and accompanying WinElli software [Figure 3.2.1 (a)]. The optical penetration depth, which is given by $\xi = \lambda/4\pi k$ [98], is shown in Figure 3.2.1 (b). We find that $\xi \sim 25$ nm at $\lambda=795$ nm, which is the fundamental wavelength used in all SHG measurements. Samples were characterized by Fourier Transform Infrared Spectroscopy (FTIR) using a Nicolet Magna 860 FTIR Spectrometer [Figure 3.2.1 (b) inset]. The plasmon resonance was measured to be $f_p=1.67 \times 10^{13}$ Hz, from which we calculate an electron density of $n_e=4.33 \times 10^{17}$ cm $^{-3}$ [45].

The SHG experimental layout is shown schematically in Figure 3.2.2. Ultrashort laser pulses with a center wavelength of 795 nm ($\hbar\omega = 1.56$ eV) and a duration of 80 fs at FWHM were generated from a Ti:sapphire oscillator. The 80 MHz repetition rate was reduced to 1.6 MHz by a pulse picker and the average laser intensity of 0.63 kW/cm 2 used for the experiments is well below the Bi $_2$ Se $_3$ damage threshold. The incident laser polarization was set by adjusting a $\lambda/2$ and a $\lambda/4$ waveplate. The beam was focused to a 20 μm $1/e^2$ spot size on the sample at an incident angle of 45 $^\circ$. Specularly reflected photons at the second harmonic

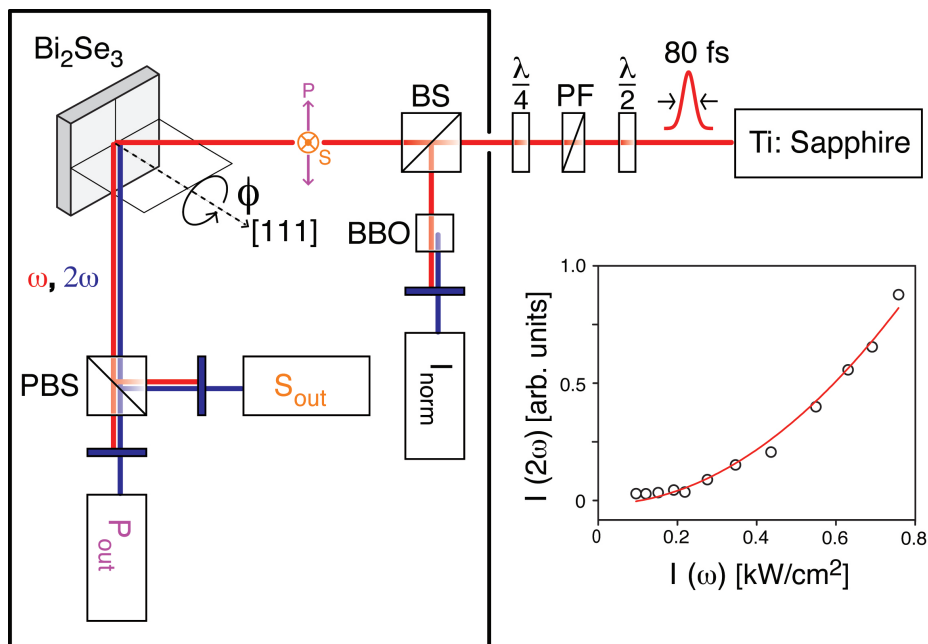


Figure 3.2.2: SHG experimental apparatus. Schematic of the experimental layout showing the complete beam path. The path of the fundamental (ω) and second harmonic (2ω) beams are shown in red and blue respectively. Experiments were performed in a dark enclosure to avoid stray light (see contour). Optical elements are denoted as follows: polarizing beam splitter (PBS), quarter- and half-wave plate ($\lambda/4$ and $\lambda/2$), beam splitter (BS), polarization filter (PF) and β -barium borate (BBO). Photomultiplier tubes are drawn as rectangles that measure the outgoing SHG with P_{out} and S_{out} polarizations as labeled. The photomultiplier tube used to measure laser intensity fluctuations is labeled I_{norm} . Wavelength filters are drawn as flat blue strips. Inset: Measured SHG intensity at $\phi = 0$ in the P_{in} - P_{out} polarization geometry as a function of the fundamental light intensity. The red line is a fit that shows the expected quadratic relationship between the two. Figure reprinted from [74].

energy ($\hbar 2\omega = 3.12$ eV) with polarization in (P) and out of (S) the scattering plane were spatially separated by a polarizing beam splitting cube and simultaneously measured using calibrated photomultiplier tubes sensitive to 3.1 eV photons. Before the photomultiplier tubes, the reflected fundamental light was removed through both absorptive and interference filtering. The second harmonic nature of the detected signal was confirmed by checking that it scaled quadratically with the incident beam intensity [Figure 3.2.2 inset]. Part of the incident beam was split off before the sample and passed through a β -barium borate crystal to generate second harmonic light against which both P and S channels were normalized to account for laser intensity fluctuations. $\text{Bi}_2\text{Se}_3(111)$ samples were mounted on a rotation stage and aligned so that the center of rotation coincided with the center of the focus of the incident beam. An accurate alignment was achieved by imaging the sample with a 50x microscope objective and a high resolution CCD camera. The second harmonic light generated as a function of the in-plane crystal orientation was measured by recording $I(2\omega)$ in both polarization channels as a function of the sample rotation angle φ around the (111) axis, and as a function of the incident polarization [Figure 3.2.3(a)]. All samples were cleaved along the (111) plane in air or O_2 under ambient pressure and temperature prior to measurement. For the O_2 measurements, a continuous flow of O_2 (99.5% Airgas) gas was directed on the sample at a pressure of 10 psi and at a distance of approximately one cm inside a sealed enclosure.

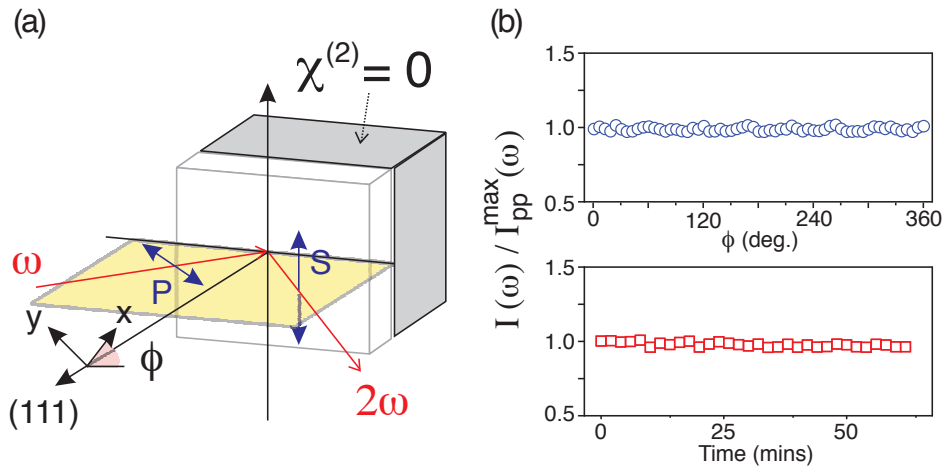


Figure 3.2.3: SHG sample geometry and linear optical response. (a) Schematic of the SHG sample geometry. Surface and bulk regions are colored white and gray respectively. (b) Top panel: Normalized intensity of the reflected beam at the fundamental frequency $I(\omega)$ from the (111) surface of Bi_2Se_3 measured as a function of azimuthal angle ϕ . Data are shown in the $P_{in} - P_{out}$ polarization geometry, but similar isotropic patterns were obtained under all four linear and four circular polarization geometries. Bottom panel: Intensity $I(\omega)$ at $\phi = 0^\circ$ in the $P_{in} - P_{out}$ polarization geometry measured as a function of time after cleavage in air. Figure reprinted from [74].

3.2.2 FIRST-ORDER LINEAR OPTICAL RESPONSE

Before performing SHG measurements, we characterized the $\chi^{(1)}$ first-order linear optical response by measuring the reflected light intensity at the fundamental frequency 200 minutes after the sample was cleaved in air. A typical trace is shown in the top panel of Figure 3.2.3 (b) for the $P_{in} - P_{out}$ geometry. As a function of the sample rotation angle φ , $I(\omega)$ is clearly isotropic, confirming that all off-diagonal tensor elements of $\chi^{(1)}$ are zero and that $\chi_{11}^{(1)} = \chi_{22}^{(1)}$ as expected from (3.3). Similar isotropic traces were recorded for all input-output polarization geometries.

In section 3.2.4 we show that $I(2\omega)$ increases after cleaving in air on the hour time scale before saturating. To check that this is not related to a change in the bulk electronic structure, we measured the time dependence of $I(\omega)$ immediately after cleaving in the $P_{in} - P_{out}$ geometry, since the linear response is predominantly representative of bulk properties. It is clear from the bottom panel of Figure 3.2.3 (b) that after cleaving the intensity of $I(\omega)$ remains constant. No measurable changes in $I(\omega)$ with time were observed at all φ and in all input-output polarization geometries.

3.2.3 SECOND-ORDER NONLINEAR OPTICAL RESPONSE

We now characterize the second-order nonlinear optical response by measuring the second harmonic light generated from $\text{Bi}_2\text{Se}_3(111)$. Equa-

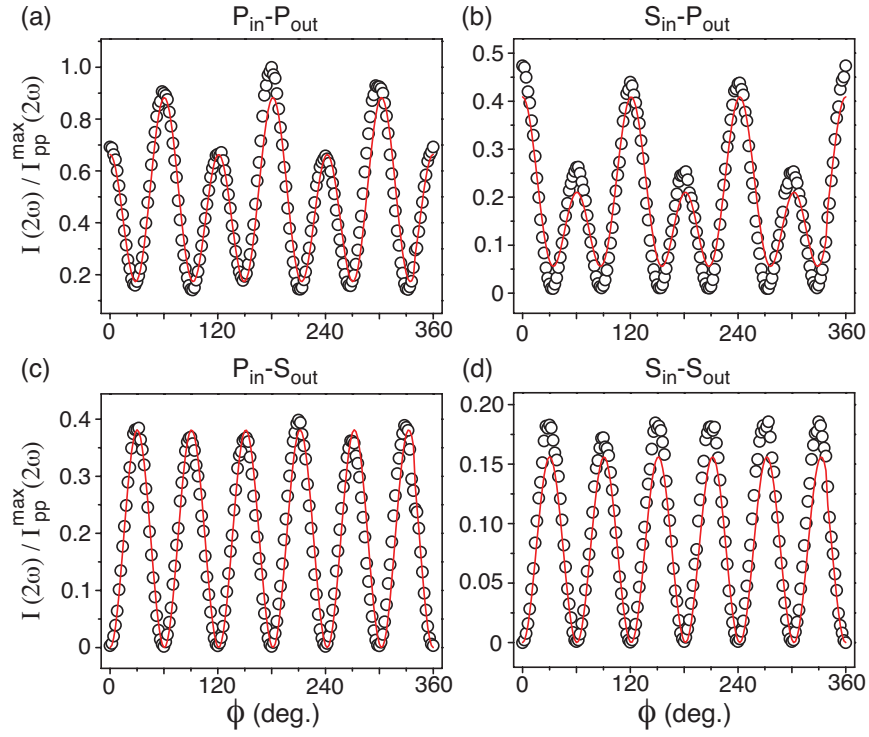


Figure 3.2.4: Rotational anisotropy of SHG from $\text{Bi}_2\text{Se}_3(111)$. Normalized SHG intensity $I(2\omega)$ from the $\text{Bi}_2\text{Se}_3(111)$ surface measured as a function of azimuthal angle ϕ between the bisectrix $(11\bar{2})$ and the scattering plane. Measurements taken 200 minutes after cleavage in (a) $P_{in}-P_{out}$, (b) $S_{in}-P_{out}$, (c) $P_{in}-S_{out}$ and (d) $S_{in}-S_{out}$ incident and outgoing photon polarization geometries. All data sets are normalized to the maximum intensity measured at $t = 200$ mins in the $P_{in}-P_{out}$ geometry. Solid lines are fits to (3.6). Figure reprinted from [74].

tion (3.6) shows that the tensor components of the combined $\chi^{(2)} + \chi^{(3)}\mathcal{E}$ susceptibilities, which encode the surface + accumulation region electrical responses respectively, can be determined by measuring $I(2\omega)$ as a function of the sample rotation angle φ in different input-output light polarization geometries. Figure 3.2.4 show the results of these measurements taken 200 minutes after the sample was cleaved in air. Unlike the linear optical response [Figure 3.2.3(b) top], $I(2\omega)$ is clearly anisotropic as a function of φ in all four linear polarization geometries. A fit of (3.6) to the SHG patterns using a single set of susceptibility tensor elements yields excellent agreement [Figure 3.2.4 red lines], which shows that the data are consistent with surface + accumulation layer SHG from Bi_2Se_3 . The fit parameters are shown in Table 3.2.1. We find that the largest contribution to the combined $\chi^{(2)} + \chi^{(3)}\mathcal{E}$ non-linear susceptibility comes from $|c^{(1)}|$, which describes the only purely in-plane electrical response at the surface ($|a^{(1)}|$) from $\chi^{(2)}$, in addition to accumulation region contributions ($|b^{(1)}|$). The components $|c^{(2)}|$ and $|c^{(3)}|$, which contain only tensor elements that involve an out of plane response, are smaller than $|c^{(1)}|$ by a factor of approximately 2 and 5 respectively. In section 3.2.4 we show that the relative contributions of each $a^{(n)}$ and $b^{(n)}$ can be determined by studying the time evolution of $I(2\omega)$ after cleaving the sample.

The data in Figure 3.2.4 exhibit a clear 3-fold or 6-fold rotational symmetry depending on whether the outgoing photons measured have a polarization component perpendicular (P -polarized) or parallel (S -pol-

Table 3.2.1: This table displays the best fit values of the parameters $c^{(n)} \equiv a^{(n)} + b^{(n)}$ when (3.6) and (3.7) are simultaneously fitted to both the linear polarization [Figure 3.2.4] and circular polarization [Figure 3.2.7] SHG data taken 200 minutes after cleavage. The ' and '' refers to the real and imaginary parts respectively, and all parameters are given in terms of its ratio to $c^{(1)'}$.

$c^{(1)'}$	$c^{(1)''}$	$c^{(2)'}$	$c^{(2)''}$	$c^{(3)'}$	$c^{(3)''}$	$c^{(4)'}$	$c^{(4)''}$	$c^{(s)'}$	$c^{(s)''}$
1	2.00	0.60	-0.71	-1.46	0.44	0.33	0.39	0.64	0.00

arized) to the sample plane respectively. Because *S*-polarized light only has in-plane electric-field components, it is only a sensitive measure of the in-plane response encoded by $c^{(1)}$. This likely originates from the anharmonic polarizability of the Se-Se bonds [Figure 3.1.1], which have a 6-fold symmetric arrangement in the sample plane. On the other hand, because *P*-polarized light contains an electric-field component along \hat{z} , it is a sensitive measure of the out-of-plane responses $c^{(2)}$ and $c^{(3)}$. These originate from the Se-Bi bonds, which have a 3-fold symmetric arrangement that extend into the bulk.

3.2.4 SURFACE MOLECULAR DOPING EFFECTS ON SHG

To prove that the surface and accumulation region SHG is dominant over multipole bulk effects, and to quantify their relative contributions, we studied the response to changes in the surface carrier concentration. Angle-resolved photoemission spectroscopy (ARPES) studies have shown that Bi_2Se_3 exhibits an intrinsic surface band-bending after cleavage

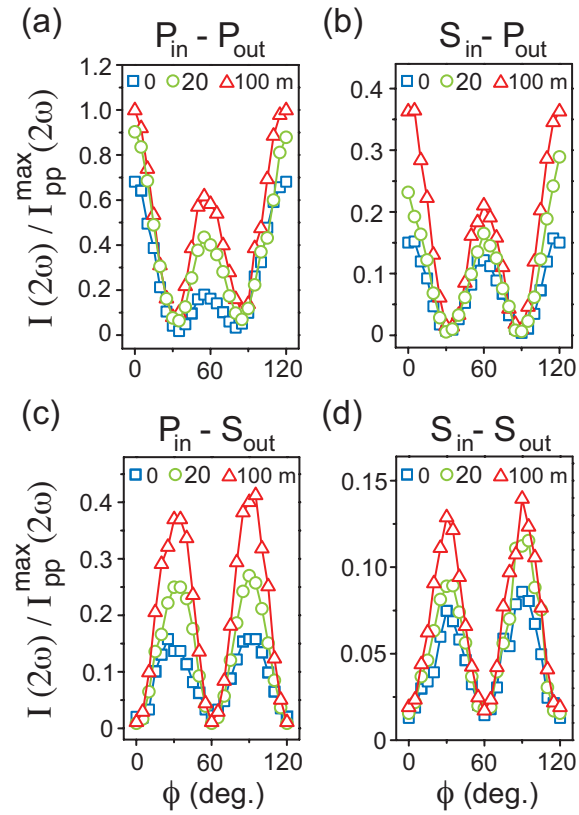


Figure 3.2.5: SHG ϕ dependence at different times after cleavage in air. (a) $P_{in}-P_{out}$, (b) $S_{in}-P_{out}$, (c) $P_{in}-S_{out}$ and (d) $S_{in}-S_{out}$ photon polarization geometries. Figure reprinted from [74].

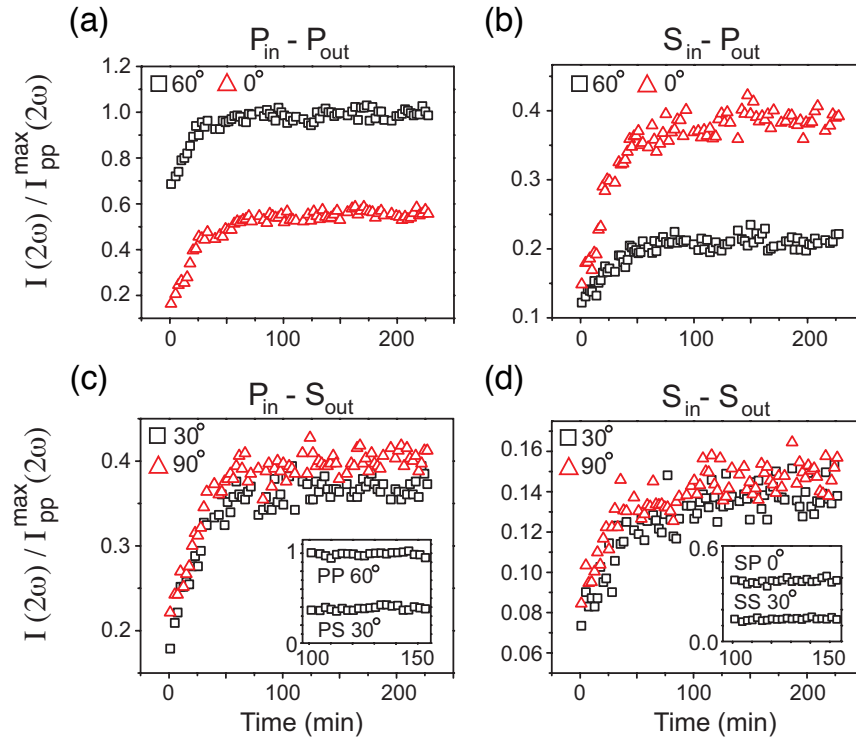


Figure 3.2.6: Time evolution of SHG after cleavage in air. (a) $P_{in}-P_{out}$, (b) $S_{in}-P_{out}$, (c) $P_{in}-S_{out}$ and (d) $S_{in}-S_{out}$ photon polarization geometries. The insets in (c) and (d) show the time evolution of the peak SHG intensities starting at 100 minutes after cleavage in air, prior to which the sample was not exposed to laser light. Figure reprinted from [74].

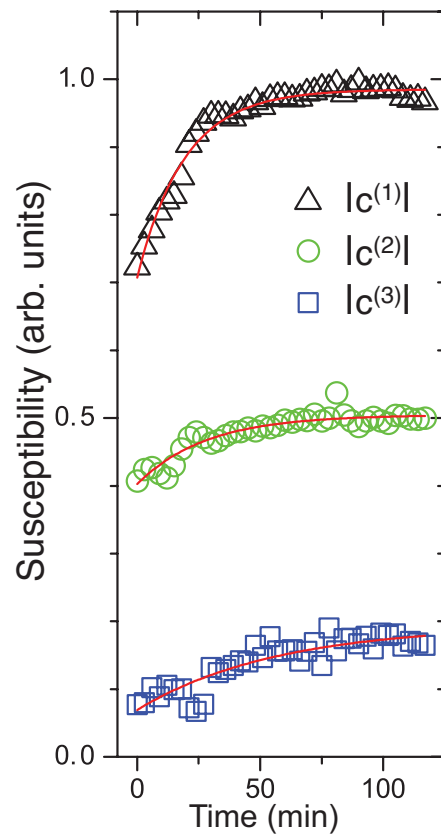


Figure 3.2.7: Time evolution of fit coefficients after cleavage in air. Fit coefficients from fitting (3.6) to the SHG data in Figure 3.2.5 as a function of time after cleavage in air. Because the phase of the complex fit parameters cannot uniquely be determined, it is only informative to show the absolute values. Figure reprinted from [74].

in ultra-high vacuum (UHV) that acts to monotonically increase the electron density at the surface on the hour time scale until a stable accumulation layer is formed [41, 47, 79]. If SHG from Bi_2Se_3 is in fact surface sensitive, such a surface electronic change should be manifested in our measurements. This is because, as shown in section 3.1.1, the band-bending electric field acts to break inversion symmetry over the depth that it penetrates into the bulk [Figure 3.1.2], thereby permitting SHG in the accumulation region with an intensity that is proportional to the field strength. Figure 3.2.5 show a clear increase in $I(2\omega)$ at all φ and in all input-output linear polarization geometries as a function of time after cleavage in air. However, there is no change in the rotational symmetry of the SHG patterns, which rules out any trigonal symmetry breaking atomic reconstruction, as is typical of semiconductors such as $\text{Si}(111)$ in air [89]. Figure 3.2.6 show the complete time dependencies of the SHG peak intensities, which all undergo the same monotonic increase by as much as 400% between $t \approx 1$ and $t = 50$ mins following cleavage, after which they saturate to a value that remains constant out to at least 600 mins. This is a trend highly consistent with the time evolution of the surface Fermi level observed using ARPES [47] and cannot have a bulk origin as no bulk electronic changes were observed with time after cleaving [Figure 3.2.3(b) bottom].

Slow photo-induced changes in SHG intensity are known to occur on semiconductor surfaces such as GaAs [99] and oxidized Si [91, 100] through a two-step charge-excitation charge-trapping processes [91, 99]. To test for such effects, we repeated the measurements after keeping the

sample unexposed to laser light for the first 100 mins after cleavage [Figure 3.2.6 (c)-(d) insets]. The fact that the SHG intensities under these conditions show no time dependence and match the previous saturation intensities shows that the observed time evolution is purely a surface doping effect and not a photo-induced effect.

To understand how the nonlinear susceptibilities evolve with time, we simultaneously fit the SHG data in Figure 3.2.6 at each point in time to (3.6). The time dependence of the fit coefficients is shown in Figure 3.2.7. We find that $|c^{(1)}|$, $|c^{(2)}|$, and $|c^{(3)}|$, which together primarily encode the in-plane electrical response [(3.9) and (3.10)], generally increase as a function of time. This precludes a change in the interatomic-layer distance at the surface after cleaving as the primary source of the increased SHG signal because this would predominantly affect only the out-of-plane susceptibilities. The coefficient $|c^{(4)}|$, which describes the only purely out-of-plane electrical response, on the other hand, generally decreases as a function of time. The dip feature exhibited by $|c^{(2)}|$, $|c^{(3)}|$, and $|c^{(4)}|$ at early times is currently unclear and requires and awaits a detailed microscopic theoretical description of SHG from Bi_2Se_3 . However, we note that this feature is similar to that observed in the raw SHG data for samples cleaved in an O_2 environment as a function of time in Figure 3.2.8(a)-(b).

Because we find that the band-bending in air occurs on the same time scale observed in samples cleaved in UHV, its cause is unlikely related to the direct charging of the surface by absorbed molecules from the en-

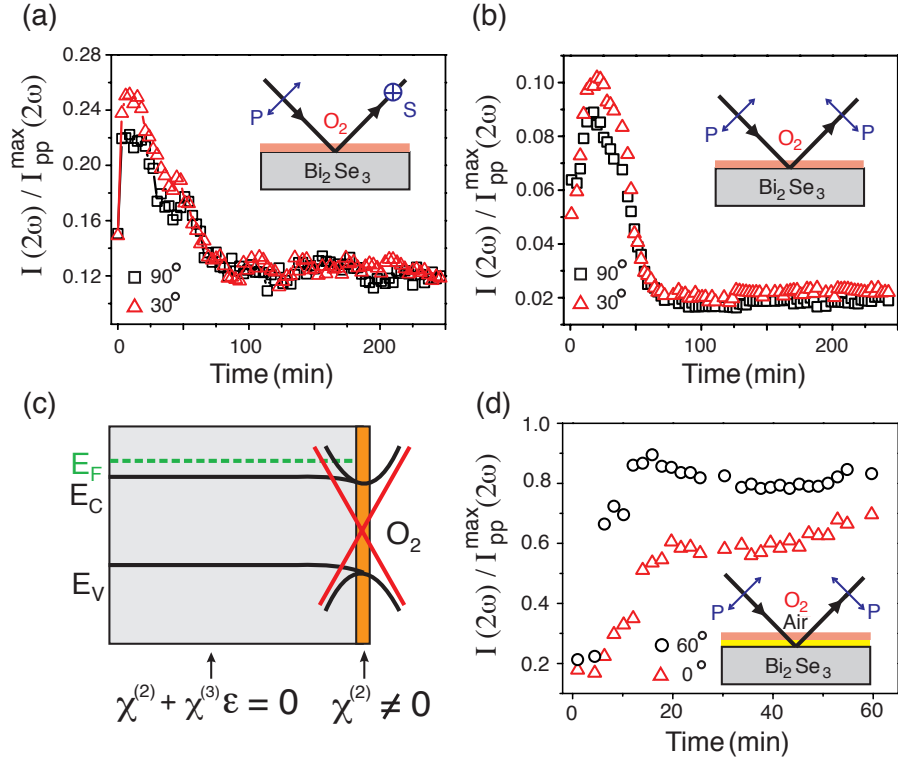


Figure 3.2.8: SHG time-dependence after cleavage in O_2 . (a) Time dependence of the SHG peak intensities measured in the $P_{in}-S_{out}$ polarization geometry after cleaving in O_2 . (b) Time dependence of the SHG minima measured in the $P_{in}-P_{out}$ polarization geometry after cleaving in O_2 . Similar behaviors were also observed in other polarization geometries. (c) Schematic of the energy evolution of the bulk conduction band minimum (E_C) and bulk valence band maximum (E_V) relative to the Fermi level (E_F) as a function of distance to the O_2 covered surface. (d) Time dependence of the SHG peak intensities measured in the $P_{in}-P_{out}$ polarization geometry after cleaving in air then immediately covering the surface with O_2 gas. Figure reprinted from [74].

vironment, for the absorption rates in air and UHV will be different by orders of magnitude. It must therefore be due to an intrinsic material property. Intrinsic band-bending is known to occur through the migration of charged impurities within the crystal—a process that can take place on the hour time scale [101]. If this is the case in our samples, the migrating impurities are most likely negatively charged Se vacancies, which are prolific in Bi_2Se_3 , that may move to the surface to lower the surface energy of the topmost Se layer after cleaving, thereby increasing the surface carrier density.

Although we have shown that the $\chi^{(2)}$ and $\chi^{(3)}\mathcal{E}$ contributions to SHG from $\text{Bi}_2\text{Se}_3(111)$ can be distinguished, isolating the surface electronic response, which is only encoded in $\chi^{(2)}$, will require eliminating the accumulation region SHG. Experiments have shown that O_2 is an effective electron acceptor when deposited on the surface of Bi_2Se_3 [31]. To demonstrate that the accumulation region SHG can be eliminated and to confirm that SHG is sensitive to tuning the surface carrier density, we studied the time evolution of $I(2\omega)$ after cleaving the sample in an O_2 environment. Figure 3.2.8(a)-(b) show that $I(2\omega)$ initially increases to reach approximately 50% of the saturation intensity value in air, then slowly decreases back to its initial value. These results show that electron transfer from the Bi_2Se_3 surface to the absorbed O_2 molecules takes place only after some finite surface charge has developed, and that O_2 can restore the surface back to an un-charged state, where $\vec{\mathcal{E}}=0$, but cannot hole dope beyond this state [Figure 3.2.8(c)]. This further indicates that $\vec{\mathcal{E}}$ arises from the migration of negatively char-

ged Se vacancies to the surface because assuming that charge transfer only takes place when an O_2 molecule is adsorbed at a surface Se vacancy site, no additional hole doping will occur once all vacancies are occupied. Figure 3.2.8(d) shows that this hole doping does not occur when the sample is cleaved in air then immediately exposed to O_2 , which confirms that the charge transfer only occurs by molecules initially absorbed on the surface.

Assuming that the surface doping is negligibly small immediately after cleaving in air ($\vec{\mathcal{E}} \sim 0$), we estimate that the $\chi^{(2)}$ and $\chi^{(3)}\mathcal{E}$ contributions to SHG are roughly equal at long times after cleaving in air. We estimate that the accumulation region penetrates approximately 12 nm into the bulk using the Thomas-Fermi screening length

$$\lambda_{TF} = (3ne^2/2\epsilon_{dc}E_f)^{-1/2}$$

as an approximation [3], where $n = 3.68 \times 10^{17} \text{ cm}^{-3}$ is the bulk carrier density [Figure 3.2.1(b) inset], $\epsilon_{dc} \sim 113\epsilon_0$ is the dc electric permittivity for Bi_2Se_3 [54], and we approximate

$$E_f = \frac{\hbar^2}{2m}(3\pi^2n)^{2/3} = 0.013 \text{ eV}$$

using $m = 0.14m_e$ [54].

3.2.5 CIRCULAR DICHROISM SHG

Having established that a pure surface $\chi^{(2)}$ measurement can be performed on the Bi_2Se_3 materials class that is sensitive to both the surface crystal structure and the surface carrier concentration, we consider how SHG can be used to monitor time-reversal symmetry (TRS) at a topological insulator surface. It has been proposed that new TRS broken phases can be measured through the differential absorption of right- (R) versus left- (L) circularly polarized light [30, 34, 82]. However, it is known that the linear response of Bi_2Se_3 to circularly-polarized light is only sensitive to bulk electrons [83]. In order to understand whether second harmonic versions of such experiments are feasible, it is necessary to measure the intrinsic surface electrical response of Bi_2Se_3 to circular-polarized light.

Second harmonic circular dichroism (CD), which is the difference in SHG yield using incident R - versus L -circularly polarized fundamental light, was measured from Bi_2Se_3 200 minutes after cleavage in air. Figure 3.2.9(a)-(b) show a clear difference between the SHG intensity patterns measured using R - versus L -circularly polarized input for both S - and P -polarized output geometries in the absence of applied currents or magnetic fields, which are well described by (3.7) using the same set of susceptibility values fitted to Figure 3.2.4. By plotting CD as a function of φ [Figure 3.2.9(c)], we find that CD varies sinusoidally, with the S - and P -polarized output components (CD_S and CD_P) out of phase by exactly 180° , as expected from (3.7). Although second harmonic CD

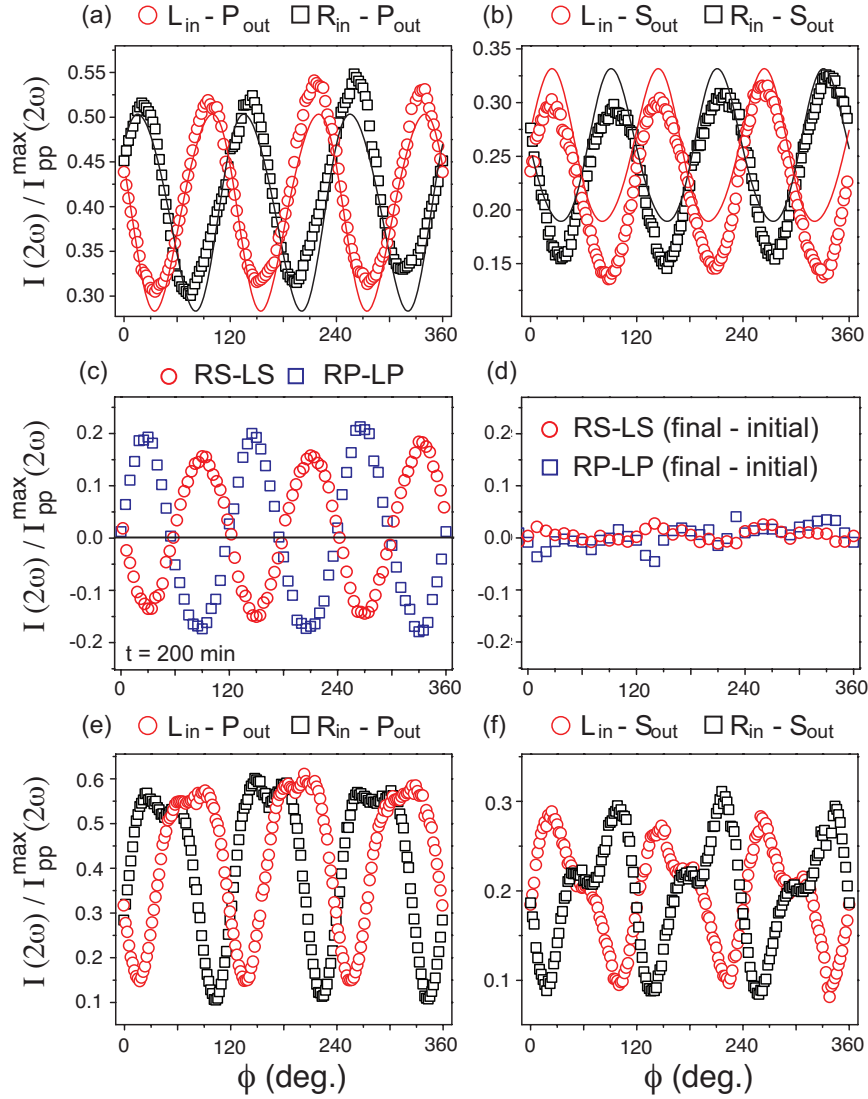


Figure 3.2.9: Circular dichroism SHG from Bi_2Se_3 . Normalized ϕ -dependent SHG intensity patterns measured 200 minutes after cleavage in air under (a) left-circular in $(L_{in}) S_{out}$ and right-circular in $(R_{in}) S_{out}$, and (b) $L_{in} - P_{out}$ and $R_{in} - P_{out}$ photon polarization geometries. Solid lines are theoretical fits to (3.7). (c) Circular dichroism ($I_R - I_L$) corresponding to data in panels (a) and (b). (d) Difference between circular dichroism measured at 200 minutes after cleavage and immediately after cleavage. Normalized SHG intensity patterns in different samples in (e) left-circular in $(L_{in}) S_{out}$ and right-circular in $(R_{in}) S_{out}$, and (f) $L_{in} - P_{out}$ and $R_{in} - P_{out}$ photon polarization geometries. Figure reprinted from [74].

can arise through the interference of higher-order bulk multipole and surface dipole SHG radiation, such effects are known to be suppressed when the photon energy exceeds the bulk band gap and we have shown that the bulk multipole contributions to SHG are negligible. The SHG CD must therefore arise from the surface. Because the surface susceptibility tensor elements are proportional to transition amplitudes between eigenstates $|1\rangle$ and $|2\rangle$ in the band structure, which scale as $1/(\hbar\omega - E_{12} - i\gamma)$ with E_{12} being the energy difference and γ being an absorption factor, a large imaginary part to the surface $\chi^{(2)}$ occurs when $\hbar\omega$ is close to an inter-band transition. Since $\hbar\omega > \Delta$ in our experiment, such resonant excitations can readily occur between the surface and bulk continuum states, leading to pronounced CD.

While CD is generally non-zero, Figure 3.2.9(c) shows that it vanishes when φ is an integer multiple of 60° , angles where the scattering plane coincides with a mirror plane of the (111) surface [Figure 3.1.1]. Such zeroes are protected by mirror symmetry because *R*- and *L*-circularly polarized light transform into one another under mirror reflection about the scattering plane. Because a magnetization can break mirror symmetry, measuring departures from zero in CD along these specific values of φ can be a sensitive probe of TRS breaking on the surface of Bi_2Se_3 . Remarkably, we find that CD at a general φ is insensitive to surface charging, as evidenced by the lack of measurable change as a function of time after cleavage [Figure 3.2.8(d)]. This suggests that sensitive searches for TRS breaking induced CD may be carried out without the need for careful control of surface charging, which is an impor-

tant and robust way of studying the physics of surface doped topological insulators or buried interfaces between topological insulators and ordinary materials [24, 28].

In certain samples, the φ -dependence of $I(2\omega)$ with circularly polarized light exhibited additional features that cannot be accounted for by (3.7) [Figure 3.2.9(e)-(f)]. These appear to be smaller SHG extrema that are shifted from the extrema exhibited in Figure 3.2.9(a)-(b) by 60° . However, the φ -dependence of $I(2\omega)$ in the linear polarization input configurations in the same samples appeared to be unaffected due to the 60° periodicity of the SHG extrema. The origin of these features is currently unclear and require further investigation, but we believe that they may be a result of crystal twinning.

3.3 SUMMARY AND OUTLOOK

We have presented a theoretical and experimental study of second harmonic generation from the topological insulator Bi_2Se_3 . By performing a crystal symmetry analysis we identified the nonlinear electric susceptibility tensor elements that contribute to SHG. The analysis showed that the process is forbidden in the bulk of Bi_2Se_3 owing to the presence of inversion symmetry, but can be generated at the surface where inversion symmetry is necessarily broken. We also found that SHG can be generated near the surface in the accumulation region where the band-

bending electric field breaks inversion symmetry over the depth that it penetrates into the bulk. We incorporated the symmetry analysis results into a phenomenological model and showed that the relative magnitudes of the susceptibility tensor elements can be determined by measuring the SHG intensity and polarization as a function of the in-plane crystal orientation and incident laser polarization.

To test the model, we performed SHG experiments on bulk single crystals of Bi_2Se_3 . We first described the sample growth process and reported the characterization results. We also determined the complex index of refraction in the visible range, which is a necessary input parameter to the theoretical model, by performing spectroscopic ellipsometry measurements. We described the experiment we designed to isolate the SHG signal and characterized the first-order linear optical response. We measured the radiated SHG intensity and polarization as a function of crystal orientation and incident laser polarization, and the results were consistent with our theoretical model. We fit the data and reported the relative contributions to SHG from each of the nonlinear susceptibility elements.

To confirm that the surface and accumulation region were the dominant source of SHG and to quantify their relative contributions, we performed a surface doping dependence study. When the sample was cleaved in air, the SHG intensity in all polarization configurations monotonically increased on the hour time scale before saturating and remaining constant out to at least several hours. We attributed this behavior to the slow formation of the SHG generating accumulation region

that results from the intrinsic band-bending in Bi_2Se_3 after cleaving [41, 47, 79]. We estimated from the results that the surface and accumulation region contributions to SHG were comparable at long times in air. When cleaved in an oxygen environment, the SHG intensity initially increased then slowly decreased back to its initial value. This is consistent with ARPES results showing that depositing oxygen on the surface of Bi_2Se_3 lowers the surface carrier density and hence the magnitude of the band-bending electric field that induces SHG in the accumulation region [31]. These results show that SHG can be used to monitor changes in the surface Fermi level.

We finally investigated the SHG response using circularly polarized light as a function of the in-plane crystal orientation. We found pronounced circular dichroism at all crystal rotation angles except along certain planes of mirror symmetry where the circular dichroism vanished. We proposed that sensitive searches for time-reversal symmetry breaking could be performed by monitoring the SHG circular dichroism along these mirror planes.

The theoretical description and experimental realization of surface second harmonic generation from the Bi_2Se_3 materials class provides a novel contact-free probe of electrical response from a single surface of a topological insulator. The ability to perform such surface sensitive experiments with tuning control of the surface carrier concentration in ambient conditions is promising for future technological applications of topological insulators.

References

- [1] Lev Davidovich Landau, Evgenii Mikhailovich Lifshitz, and Lev Petrovich Pitaevskii. *Statistical physics; 2nd ed.* Course of theoretical physics. Pergamon, Oxford, 1980.
- [2] K Klitzing, G Dorda, and M Pepper. New Method for High-Accuracy Determination of the Fine-Structure Constant Based on Quantized Hall Resistance. *Physical Review Letters*, 45(6):494–497, August 1980.
- [3] Neil W Ashcroft and N David Mermin. *Solid state physics*. Holt, Rinehart and Winston, New York, NY, 1976.
- [4] J E Avron, D Osadchy, and R Seiler. A topological look at the quantum Hall effect. *Physics Today*, (August), August 2003.
- [5] S Chern. On the curvatura integra in a Riemannian manifold. *Annals of Mathematics*, 1945.
- [6] D J Thouless, M Kohmoto, M P Nightingale, and M den Nijs. Quantized Hall Conductance in a Two-Dimensional Periodic Potential. *Physical Review Letters*, 49(6):405–408, 1982.
- [7] M Kohmoto. Topological invariant and the quantization of the Hall conductance. *Annals of Physics*, 1985.
- [8] Michael V Berry. Quantal phase factors accompanying adiabatic changes. *Proc.Roy.Soc.Lond.*, A392(1802):45–57, 1984.

- [9] R B Laughlin. Quantized Hall conductivity in two dimensions. *Physical Review B*, 1981.
- [10] B I Halperin. Quantized Hall conductance, current carrying edge states, and the existence of extended states in a two-dimensional disordered potential. *Phys.Rev.*, B25(4):2185–2190, 1982.
- [11] C Kittel. *Introduction to Solid State Physics*. John Wiley & Sons, Inc, 5th edition edition, 2005.
- [12] Shuichi Murakami, Naoto Nagaosa, and Shou-Cheng Zhang. Spin-Hall Insulator. *Physical Review Letters*, 93(15):156804, October 2004.
- [13] F D M Haldane. Model for a Quantum Hall Effect without Landau Levels: Condensed-Matter Realization of the 'Parity Anomaly'. *Physical Review Letters*, 61(18):2015–2018, 1988.
- [14] B Andrei Bernevig and Shou-Cheng Zhang. Quantum Spin Hall Effect. *Physical Review Letters*, 96(10):106802, March 2006.
- [15] C L Kane and E J Mele. *Z₂ topological order and the quantum spin Hall effect,* *Phys. Rev. Lett*, vol. 95, p. 146802, 2005. B. Bernevig and SC Zhang. Quantum spin Hall effect," *Phys. Rev. Lett*, 2006.
- [16] B A Bernevig and T L Hughes. *Quantum spin Hall effect and topological phase transition in HgTe quantum wells,* *Science*, vol. 314, p. 1757, 2006. M. König, S. Wiedmann, C. Briine, A. Quantum spin Hall insulator state in HgTe quantum ..., 2007.
- [17] Markus König, Steffen Wiedmann, Christoph Brüne, Andreas Roth, Hartmut Buhmann, Laurens W Molenkamp, Xiao-Liang Qi, and Shou-Cheng Zhang. Quantum Spin Hall Insulator State

in HgTe Quantum Wells. *Science*, 318(5851):766–770, November 2007.

- [18] Christoph Brüne, Andreas Roth, Hartmut Buhmann, Ewelina M Hankiewicz, Laurens W Molenkamp, Joseph Maciejko, Xiao-Liang Qi, and Shou-Cheng Zhang. Spin polarization of the quantum spin Hall edge states. *Nature Physics*, 8(6):485–490, May 2012.
- [19] Liang Fu, C Kane, and E Mele. Topological Insulators in Three Dimensions. *Physical Review Letters*, 98(10):106803, March 2007.
- [20] J Moore and L Balents. Topological invariants of time-reversal-invariant band structures. *Physical Review B*, 75(12):121306, March 2007.
- [21] Rahul Roy. Three dimensional topological invariants for time reversal invariant Hamiltonians and the three dimensional quantum spin Hall effect. *arXiv.org*, (19):195322, July 2006.
- [22] Liang Fu and C Kane. Topological insulators with inversion symmetry. *Physical Review B*, 76(4):045302, July 2007.
- [23] D X Qu, Y S Hor, J Xiong, R J Cava, and N P Ong. Quantum Oscillations and Hall Anomaly of Surface States in the Topological Insulator Bi_2Te_3 . *Science*, 329(5993):821–824, August 2010.
- [24] J E Moore. The birth of topological insulators. *Nature*, 464:194–198, 2010.
- [25] A R Mellnik, J S Lee, A Richardella, J L Grab, P J Mintun, M H Fischer, A Vaezi, A Manchon, E A Kim, N Samarth, and D C Ralph. Spin-transfer torque generated by a topological insulator. *Nature*, 511(7510):449–451, April 2015.

- [26] J Wunderlich, B G Park, A C Irvine, and L P Zarbo. Spin Hall effect transistor. *Science*, 330:1801–1804, 2010.
- [27] Oleg V Yazyev, Joel E Moore, and Steven G Louie. Spin Polarization and Transport of Surface States in the Topological Insulators Bi_2Se_3 and Bi_2Te_3 from First Principles. *Physical Review Letters*, 105(26):266806, December 2010.
- [28] M Z Hasan and C L Kane. Colloquium: topological insulators. *Reviews of Modern Physics*, 82(4):3045–3067, 2010.
- [29] X L Qi and S C Zhang. Topological insulators and superconductors. *Reviews of Modern Physics*, 83(4):1057–1110, 2011.
- [30] X L Qi, E Witten, and S C Zhang. Axion topological field theory of topological superconductors. *Physical Review B*, 87(134519), 2013.
- [31] Y L Chen, J H Chu, J G Analytis, Z K Liu, K Igarashi, H H Kuo, X L Qi, S K Mo, R G Moore, D H Lu, M Hashimoto, T Sasagawa, S C Zhang, I R Fisher, Z Hussain, and Z X Shen. Massive Dirac Fermion on the Surface of a Magnetically Doped Topological Insulator. *Science*, 329(5992):659–662, August 2010.
- [32] Y H Wang, H Steinberg, P Jarillo-Herrero, and N Gedik. Observation of Floquet-Bloch States on the Surface of a Topological Insulator. *Science*, 342(6157):453–457, October 2013.
- [33] Xiao-Liang Qi, Rundong Li, Jiadong Zang, and Shou-Cheng Zhang. Inducing a Magnetic Monopole with Topological Surface States. *Science*, 323(5918):1184–1187, 2009.
- [34] Wang-Kong Tse and A H MacDonald. Giant Magneto-Optical Kerr Effect and Universal Faraday Effect in Thin-Film Topological Insulators. *Physical Review Letters*, 105(5):057401, July 2010.

- [35] Liang Fu and C Kane. Superconducting Proximity Effect and Majorana Fermions at the Surface of a Topological Insulator. *Physical Review Letters*, 100(9):096407, March 2008.
- [36] D Hsieh, D Qian, L Wray, Y Xia, Y S Hor, R J Cava, and M Z Hasan. A topological Dirac insulator in a quantum spin Hall phase. *Nature*, 452(7190):970–974, April 2008.
- [37] Y Xia, D Qian, D Hsieh, L Wray, A Pal, H Lin, and A Bansil. Observation of a large-gap topological-insulator class with a single Dirac cone on the surface. *Nature Physics*, 5:398–402, 2009.
- [38] Haijun Zhang, Chao-Xing Liu, Xiao-Liang Qi, Xi Dai, Zhong Fang, and Shou-Cheng Zhang. Topological insulators in Bi. *Nature Physics*, 5(6):438–442, May 2009.
- [39] Yoichi Ando. Topological Insulator Materials. *Journal of the Physical Society of Japan*, 82(10):102001, October 2013.
- [40] M Bianchi, R C Hatch, D Guan, T Planke, J Mi, B B Iversen, and P Hofmann. The electronic structure of clean and adsorbate-covered Bi_2Se_3 : an angle-resolved photoemission study. *Semiconductor Science and Technology*, 27(12):124001, December 2012.
- [41] Marco Bianchi, Dandan Guan, Shining Bao, Jianli Mi, Bo Brummerstedt Iversen, Philip D C King, and Philip Hofmann. Coexistence of the topological state and a two-dimensional electron gas on the surface of Bi_2Se_3 . *Nature Communications*, 1(8):128, November 2010.
- [42] Hadar Steinberg, Dillon R Gardner, Young S Lee, and Pablo Jarillo-Herrero. Surface State Transport and Ambipolar Electric Field Effect in Bi_2Se_3 Nanodevices. *Nano Letters*, 10(12):5032–5036, December 2010.

- [43] D Hsieh, Y Xia, L Wray, D Qian, A Pal, and J H Dil. Observation of unconventional quantum spin textures in topological insulators. *Science*, 323:919–922, 2009.
- [44] Y H Wang, D Hsieh, D Pilon, L Fu, D R Gardner, and Y S Lee. Observation of a warped helical spin texture in Bi_2Se_3 from circular dichroism angle-resolved photoemission spectroscopy. *Physical review ...*, 107(207602), 2011.
- [45] A Sklenár, C Drasar, A Krejcová, and P Lošťák. Optical Properties of Bi_2Se_3 - $x\text{As}_x$ Single Crystals. *Crystal Research and Technology*, 35(9):1069–1076, September 2000.
- [46] J W McIver, D Hsieh, H Steinberg, P Jarillo-Herrero, and N Gedik. Control over topological insulator photocurrents with light polarization. pages 1–5, January 2012.
- [47] D Hsieh, Y Xia, D Qian, L Wray, J H Dil, F Meier, J Osterwalder, L Patthey, J G Checkelsky, N P Ong, A V Fedorov, H Lin, A Bansil, D Grauer, Y S Hor, R J Cava, and M Z Hasan. A tunable topological insulator in the spin helical Dirac transport regime. *Nature*, 460(7259):1101–1105, August 2009.
- [48] S Raghu, S B Chung, X L Qi, and S C Zhang. Collective modes of a helical liquid. *Physical Review Letters*, 104(116401), 2010.
- [49] P Hosur. Circular photogalvanic effect on topological insulator surfaces: Berry-curvature-dependent response. *Physical Review B*, 83(035309), 2011.
- [50] F Meier and B Zakharchenya. *Optical Orientation*. Elsevier, 1984.
- [51] M Fox. *Optical Properties of Solids*. Oxford University Press, New York, 2001.

- [52] S D Ganichev and W Prettl. Spin photocurrents in quantum wells. *Journal of Physics: Condensed Matter*, 15:R935–R983, 2003.
- [53] H Diehl, V A Shalygin, and V V Bel'kov. Spin photocurrents in (110)-grown quantum well structures. *New Journal of ...*, 9:349, 2007.
- [54] James G Analytis, Jiun-Haw Chu, Yulin Chen, Felipe Corredor, Ross D McDonald, Z X Shen, and Ian R Fisher. Bulk Fermi surface coexistence with Dirac surface state in Bi_2Se_3 : A comparison of photoemission and Shubnikov–de Haas measurements. *Physical Review B*, 81(20):205407, May 2010.
- [55] G S Nolas, J Sharp, and H J Goldsmid. *Thermoelectrics: Basic Principles and New Materials Developments*. Springer-Verlag, 2001.
- [56] P Lautenschlager, M Garriga, L Vina, and M Cardona. Temperature dependence of the dielectric function and interband critical points in silicon. *Physical Review B*, 36(9):4821–4830, 1987.
- [57] E Hecht. *Optics*. Addison Wesley, 4th edition edition, 2002.
- [58] E Deyo, L E Golub, E L Ivchenko, and B Spivak. Semiclassical theory of the photogalvanic effect in non-centrosymmetric systems. *arXiv:0904.1917*, April 2009.
- [59] J E Moore and J Orenstein. Confinement-induced Berry phase and helicity-dependent photocurrents. *Physical Review Letters*, 105(026805), 2010.
- [60] A M Danishevskii, A A Kastalskii, and S M Ryvkin. Dragging of free carriers by photons in direct interband transitions in semiconductors. *Sov Phys JETP*, 58:544–550, 1970.

- [61] A F Gibson and A C Walker. Sign reversal of the photon drag effect in p type germanium. *Journal of Physics C: Solid State Physics*, 4:2209–2219, 1971.
- [62] H Hattori, M Umeno, T Jimbo, and O Fujitani. Anisotropic properties of photon drag effect in p-type germanium. *Journal of the Physical ...*, 35:826–831, 1973.
- [63] T Hatano, T Ishihara, S G Tikhodeev, and N A Gippius. Transverse photovoltage induced by circularly polarized light. *Physical Review Letters*, 103(103906), 2009.
- [64] S D Ganichev, P Schneider, V V Bel'kov, and E L Ivchenko. Spin-galvanic effect due to optical spin orientation in n-type GaAs quantum well structures. *Physical Review B*, 68(081302(R)), 2003.
- [65] Jun-ichi Inoue and Akihiro Tanaka. Photoinduced Transition between Conventional and Topological Insulators in Two-Dimensional Electronic Systems. *Physical Review Letters*, 105(1):017401, June 2010.
- [66] Netanel H Lindner, Gil Refael, and Victor Galitski. Floquet topological insulator in semiconductor quantum wells. *Nature Physics*, 7(6):490–495, March 2011.
- [67] Takuya Kitagawa, Takashi Oka, Arne Brataas, Liang Fu, and Eugene Demler. Transport properties of nonequilibrium systems under the application of light: Photoinduced quantum Hall insulators without Landau levels. *Physical Review B*, 84(23):235108, December 2011.
- [68] L Andrew Wray, Su-Yang Xu, Yuqi Xia, David Hsieh, Alexei V Fedorov, Yew San Hor, Robert J Cava, Arun Bansil, Hsin Lin,

and M Zahid Hasan. A topological insulator surface under strong Coulomb, magnetic and disorder perturbations. *Nature Physics*, 7(1):32–37, December 2010.

- [69] Marco Bianchi, Richard C Hatch, Jianli Mi, Bo Brummerstedt Iversen, and Philip Hofmann. Simultaneous Quantization of Bulk Conduction and Valence States through Adsorption of Nonmagnetic Impurities on Bi_2Se_3 . *Physical Review Letters*, 107(8):086802, August 2011.
- [70] L Andrew Wray, Suyang Xu, Madhab Neupane, Yuqi Xia, David Hsieh, Dong Qian, Alexei V Fedorov, Hsin Lin, Susmita Basak, Yew San Hor, Robert J Cava, Arun Bansil, and M Zahid Hasan. Electron dynamics in topological insulator based semiconductor-metal interfaces (topological p-n interface based on Bi_2Se_3 class). May 2011.
- [71] A A Bakun, B P Zakharchenya, and A A Rogachev. Observation of a surface photocurrent caused by optical orientation of electrons in a semiconductor. *JETP Lett*, 1984.
- [72] J Kikkawa and D Awschalom. Resonant Spin Amplification in n-Type GaAs. *Physical Review Letters*, 80(19):4313–4316, May 1998.
- [73] D Hsieh, F Mahmood, J W McIver, D R Gardner, Y S Lee, and N Gedik. Selective Probing of Photoinduced Charge and Spin Dynamics in the Bulk and Surface of a Topological Insulator. *Physical Review Letters*, 107(7):077401, August 2011.
- [74] J W McIver, D Hsieh, S G Drapcho, D H Torchinsky, D R Gardner, Y S Lee, and N Gedik. Theoretical and experimental study of second harmonic generation from the surface of the topological insulator Bi_2Se_3 . *Physical Review B*, 86(3):035327, July 2012.

- [75] J Karch, P Olbrich, M Schmalzbauer, C Brinsteiner, U Wurstbauer, M M Glazov, S A Tarasenko, E L Ivchenko, D Weiss, J Eroms, and S D Ganichev. Photon helicity driven electric currents in graphene. *arXiv:0904.1917*, February 2010.
- [76] R R Birss. *Symmetry and Magnetism*. North-Holland, Amsterdam, 1964.
- [77] G Rosenberg and M Franz. Witten effect in a crystalline topological insulator. *Physical Review B*, 82(3):035105, July 2010.
- [78] Y L Chen, J G Analytis, J H Chu, Z K Liu, S K Mo, X L Qi, H J Zhang, D H Lu, X Dai, Z Fang, S C Zhang, I R Fisher, Z Hussain, and Z X Shen. Experimental Realization of a Three-Dimensional Topological Insulator, Bi_2Te_3 . *Science*, 325(5937):178–181, July 2009.
- [79] D Hsieh, Y Xia, D Qian, L Wray, F Meier, J Dil, J Osterwalder, L Patthey, A Fedorov, H Lin, A Bansil, D Grauer, Y Hor, R Cava, and M Hasan. Observation of Time-Reversal-Protected Single-Dirac-Cone Topological-Insulator States in Bi_2Te_3 and Sb_2Te_3 . *Physical Review Letters*, 103(14):146401, September 2009.
- [80] J G Checkelsky, Y S Hor, R J Cava, and N P Ong. Bulk Band Gap and Surface State Conduction Observed in Voltage-Tuned Crystals of the Topological Insulator Bi_2Se_3 . *Physical Review Letters*, 106(19):196801, May 2011.
- [81] Yong Seung Kim, Matthew Brahlek, Namrata Bansal, Eliav Edrey, Gary A Kapilevich, Keiko Iida, Makoto Tanimura, Yoichi Horibe, Sang-Wook Cheong, and Seongshik Oh. Thickness-dependent bulk properties and weak antilocalization effect in topological insulator Bi_2Se_3 . *Physical Review B*, 84(7):073109, August 2011.

- [82] Joseph Maciejko, Xiao-Liang Qi, H Dennis Drew, and Shou-Cheng Zhang. Topological Quantization in Units of the Fine Structure Constant. *Physical Review Letters*, 105(16):166803, October 2010.
- [83] A B Sushkov, G S Jenkins, D C Schmadel, N P Butch, J Paglione, and H D Drew. Far-infrared cyclotron resonance and Faraday effect in Bi_2Se_3 . *Physical Review B*, 82(12):125110, September 2010.
- [84] A D LaForge, A Frenzel, B C Pursley, Tao Lin, Xinfei Liu, Jing Shi, and D N Basov. Optical characterization of Bi_2Se_3 in a magnetic field: Infrared evidence for magnetoelectric coupling in a topological insulator material. *Physical Review B*, 81(12):125120, March 2010.
- [85] N P Butch, K Kirshenbaum, P Syers, A B Sushkov, G S Jenkins, H D Drew, and J Paglione. Strong surface scattering in ultrahigh-mobility Bi_2Se_3 topological insulator crystals. *Physical Review B*, 81(24):241301, June 2010.
- [86] Jason N Hancock, J L M van Mechelen, Alexey B Kuzmenko, Dirk van der Marel, Christoph Brüne, Elena G Novik, Georgy V Astakhov, Hartmut Buhmann, and Laurens W Molenkamp. Surface State Charge Dynamics of a High-Mobility Three-Dimensional Topological Insulator. *Physical Review Letters*, 107(13):136803, September 2011.
- [87] R Valdés Aguilar, A V Stier, W Liu, L S Bilbro, D K George, N Bansal, L Wu, J Cerne, A G Markelz, S Oh, and N P Armitage. Terahertz Response and Colossal Kerr Rotation from the Surface States of the Topological Insulator Bi_2Se_3 . *Physical Review Letters*, 108(8):087403, February 2012.

- [88] D Hsieh, J W McIver, D H Torchinsky, D R Gardner, Y S Lee, and N Gedik. Nonlinear Optical Probe of Tunable Surface Electrons on a Topological Insulator. *Physical Review Letters*, 106(5):057401, February 2011.
- [89] Y R Shen. The principles of nonlinear optics. *New York*, 1984.
- [90] H L Dai and W Ho. Laser spectroscopy and photochemistry on metal surfaces. *World Scientific*, 1995.
- [91] J Bloch, J Mihaychuk, and H van Driel. Electron Photoinjection from Silicon to Ultrathin SiO₂ Films via Ambient Oxygen. *Physical Review Letters*, 77(5):920–923, July 1996.
- [92] S V Popov, Y P Svirko, and N I Zheludev. *Susceptibility tensors for nonlinear optics*. OP, London, 1995.
- [93] Fu Xiang Wang, Francisco J Rodríguez, Willem M Albers, Risto Ahorinta, J E Sipe, and Martti Kauranen. Surface and bulk contributions to the second-order nonlinear optical response of a gold film. *Physical Review B*, 80(23):233402, December 2009.
- [94] Xiaoqin Li, J Willits, S T Cundiff, I M P Aarts, A A E Stevens, and D S Dessau. Circular dichroism in second harmonic generation from oxidized Si (001). *Applied Physics Letters*, 89(2):022102, 2006.
- [95] Victor Mizrahi J E Sipe. Phenomenological treatment of surface second-harmonic generation. *JOSA B*, 5(3):660–667, March 1988.
- [96] T F Heinz. *Nonlinear optics of surfaces and adsorbates*. PhD thesis, University of California Berkeley.

- [97] N Bloembergen and P Pershan. Light Waves at the Boundary of Nonlinear Media. *Physical review ...*, 128(2):606–622, October 1962.
- [98] H Fujiwara. Spectroscopic ellipsometry: principles and applications, 2007.
- [99] J Qi, M Yeganeh, I Koltover, A Yodh, and W Theis. Depletion-electric-field-induced changes in second-harmonic generation from GaAs. *Physical Review Letters*, 71(4):633–636, July 1993.
- [100] S A Mitchell, T R Ward, D D M Wayner, and G P Lopinski. Charge Trapping at Chemically Modified Si(111) Surfaces Studied by Optical Second Harmonic Generation. *The Journal of Physical Chemistry B*, 106(38):9873–9882, September 2002.
- [101] A Sosin. Point-Defect Migration and Binding in Metals. *Physical review ...*, 122(4):1112–1116, May 1961.